

POLITECNICO DI TORINO

Master's Degree in Biomedical Engineering

Master's Degree Thesis

Wireless power transfer for implantable medical devices



**POLITECNICO
DI TORINO**

Supervisors

Prof. Danilo Demarchi
Ph.D. Paolo Motto Ros
M.Sc. Antonia Silvestri

Candidate

Andrea Bontempi

March 2021

Abstract

For the new generation of Active Implantable Medical Devices (AIMDs), technological advancement in electronic and micro and nanofabrication is going in the direction of reduction of size and power consumption, and improvement of therapeutic efficacy and safety. The power supply of implantable devices is still an open challenge. Most AIMDs are powered by a primary battery that takes up much space, and that has to be replaced when running out. Also, one of the main challenges is to ensure proper and sufficient power delivery to the entire device without overheating it.

We have developed a Wireless Power Transfer (WPT) link using the Near-field Resonant Inductive Coupling (NRIC) to recharge subcutaneously implanted batteries and to power supply AIMDs without a battery. We have evaluated key performance parameters for the WPT system, taking into account size, maximum power dissipation, and thermal performance of the receiver, energy provisioning from the transmitter, and overall efficiency.

First, we have characterized the WPT link by testing the transmission efficiency with respect to both the distance of the coils (up to 20 mm) and their alignment and by varying the load (simulated battery). Tests were carried out with interposed air and then with a conductive environment with high permittivity (animal tissue) to simulate skin behavior. Another essential aspect that has been taken into account is the heating of the device, which must be kept under control to avoid overheating the surrounding tissue. We have then developed a hardware and firmware communication system between the receiver and transmitter to improve the power transfer efficiency (PTE).

Measurements show that the maximum power efficiency achievable goes from 26.7% to 45.4% for 10 mA to 100 mA charging current at a relative distance of coils from 2.8 to 10 mm. The power transmission is not affected by the interposition of animal tissue. We have performed the recharge of three different batteries at 25 mA and 10 mA with a relative coils' distance of 10 mm to validate the system. The temperature increase above room temperature of the Tx coil and the Rx receiver is no more than 5 °C and 2 °C, respectively, during the 10 mA recharge phase.

Contents

List of Tables	III
List of Figures	IV
1 Introduction	1
2 State of the art	3
2.1 Active implantable medical devices	3
2.2 Power supply approaches	4
2.3 Wireless power transfer (WPT)	6
2.3.1 Near-field resonant inductive coupling (NRIC)	7
2.3.2 Near-field Capacitive Coupling (NCC)	10
2.3.3 Ultrasound based wireless systems	11
2.3.4 Solar power harvesting	13
2.3.5 Electromagnetic Mid-Field based systems	14
2.3.6 Electromagnetic Far-Field based systems	15
3 Wireless power transfer for active implantable medical devices	17
3.1 Nanofluidic drug delivery	18
3.2 SenseBack	19
3.3 Wireless power transfer approaches trade-offs	21
3.4 Integrated Circuits ICs	21
3.4.1 Analysis of receiver ICs	22
3.4.2 Analysis of transmitter ICs	24
4 NRIC power receiver	25
4.1 Wireless input power control	27
4.2 Pin-selectable charge current and voltage	27
4.3 NTC input to qualify temperature charging	27
4.4 Li-Ion charger controller and UVCL	28
4.5 PowerPath Controller	30

5	NRIC power transmitter	31
5.1	AutoResonant Switching Frequency Adjusts	31
5.2	Optimum Power Search	31
5.3	Operation	36
5.3.1	Wireless power transfer	37
5.3.2	Input current limit setting and monitoring	38
5.3.3	Frequency threshold	38
5.3.4	Timer capacitors	39
5.3.5	PTH1/2	39
5.3.6	Minimum pulse width	40
5.3.7	NTC input to measure temperature	40
5.3.8	Feedback	41
5.3.9	DTH	42
6	Proof-of-concept open-loop NRIC system evaluation	43
6.1	Test bench	43
6.2	Experimental results	45
6.2.1	Wireless power transfer issues	47
6.3	Battery charging tests	48
7	Closed-Loop NRIC system	51
7.1	Hardware design	52
7.1.1	Optimum Power Search improvements	52
7.1.2	Explicit power control	52
7.2	Embedded control loop implementation	58
7.3	Test bench	61
7.4	Experimental Results	61
7.4.1	Open-loop vs closed-loop NRIC system	61
7.4.2	Tests with interposed tissue	67
7.4.3	Lateral and Angular misalignments	70
7.5	Battery charging tests	73
7.6	Safety and regulations discussion	75
8	Conclusion and future perspectives	79

List of Tables

3.1	Quality comparison of wireless power transfer system.	21
3.2	ICs power dissipation evaluation.	24
3.3	Summury ICs evaluation.	24
4.1	Charge current and voltage programming.	28
5.1	Electrical components of transmitter circuit.	37
6.1	Comparison of primary versus secondary battery characteristics. . .	48
7.1	Summary of recharge performance. Coils distance of 10 mm. . . .	74
7.2	Analysis of heating during 4 recharging modalities tested with coils distance of 10 mm. The highest recorded temperature was reported. The room temperature is shown in figure 7.20 in the first acquisition.	78

List of Figures

2.1	Active implantable medical devices (AIMDs) [3].	4
2.2	CardioMems [1].	4
2.3	a) Electro stimulator miniaturized [4]. b) Battery-powered pacer-maker (Left; Medtronic Adapta), battery-powered swallowable endoscope (Center), Electro stimulator (Right) [4].	5
2.4	Region of EM field propagation [12].	7
2.5	NRIC scheme [2] [13].	8
2.6	Serial and Parallel resonant coupling [2].	9
2.7	NCC scheme [2].	10
2.8	Ultrasound based WPT systems [2].	12
2.9	Representation of acoustic wave propagation.	13
2.10	Solar power harvesting [29].	14
2.11	Mid-field WPT system [4].	14
2.12	Far-field WPT system [2].	15
3.1	Summary of AIMDs power supply.	17
3.2	Nanofluidic implantable platform [37]. a) PEEK body. b) Silicon nanofluidic membrane. c) Pt foil electrodes. d) PEEK lid used to seal the reservoir. e) Battery. f) Printed circuit board. g) Epoxy sealant. h) Silicon drug filling port.	18
3.3	Silicon nanofluidic membrane [37]. a) Schematic of the nanofluidic membrane. b) FIB-SEM image of the nanofluidic membrane. c) Schematic of the deposited electrode.	19
3.4	SenseBack system [38]. 1) Inductive link. 2) Bidirectional neural interface. 3) Microelectrode array.	19
3.5	Thermal image of wireless power receiver (P9027LP-R) [38].	20
3.6	Wireless power receivers size comparison. *ICs without battery management.	23
4.1	LTC4124 electrical schematic, D version [42].	25
4.2	LTC4124 functional block diagram [41].	26
4.3	Quality factor of Rx coil.	27

4.4	LTC4124 wireless power manager. Green signal is the AC voltage at ACIN pin. Red signal is the rectified voltage at pin Vcc.	28
4.5	Example of battery recharge in CC/CV mode [41].	29
5.1	LTC4125 electrical schematic, B version [42].	32
5.2	Voltage and current waveform (red and green) and input voltage control (blue) at frequency of LC tank [43].	33
5.3	Optimum Power Search flow chart [43].	35
5.4	LTC4125 functional block diagram [43].	36
5.5	Quality factor of Tx coil.	37
5.6	Timing diagram during Optimum Power Search [43].	39
5.7	PTHM vs PTH voltage.	41
5.8	Positive search. FB voltage in green, Tx coil voltage in red.	42
6.1	Overall efficiency of NRIC system.	44
6.2	Overall efficiency of NRIC system, charging current 10 mA.	45
6.3	Overall efficiency of NRIC system, charging current 25 mA.	46
6.4	Overall efficiency of NRIC system, charging current 50 mA.	46
6.5	Overall efficiency of NRIC system, charging current 100 mA.	46
6.6	Feedback fault condition. a) FB voltage (red) and Tx coil voltage coil (green). b) PTH voltage (green) and driver signal (red).	47
6.7	Overheating of IC receiver and Tx coil. Charging current of 100 mA and coils distance of 6 mm.	48
6.8	Battery recharging test, coils distance of 5 mm. a) LIR2016 charging current 10 mA. b) LIR2025 charging current 10 mA. c) LIR2032 charging current 25 mA.	50
7.1	Modification of Optimum Power Search. a) PTH voltage before modification. b) PTH voltage after IMON and PTHM modifications.	53
7.2	Evaluation of PTH pull-up resistance.	54
7.3	a) Electrical schematic for studying how the hysteresis of the comparator (LMP7300) affects the Vcc voltage at the receiver. b) Hysteresis at ± 100 mV. c) Hysteresis at ± 50 mV. d) Hysteresis at ± 25 mV. e) Hysteresis at ± 10 mV. f) Hysteresis at ± 5 mV.	55
7.4	a) Electrical schematic of transmitter with power control. b) Comparator output signal (red) and the voltage of PTH (green).	57
7.5	Duty cycle of driver signal at SW pin and power supply compared to PTH voltage.	59
7.6	Flow chart of firmware.	60
7.7	Comparison of overall efficiency, charging current of 10 mA. a) Open-loop NRIC. b) Closed-loop NRIC system.	63
7.8	Comparison of overall efficiency, charging current of 25 mA. a) Open-loop NRIC. b) Closed-loop NRIC system.	64

7.9	Comparison of overall efficiency, charging current of 50 mA. a) Open-loop NRIC. b) Closed-loop NRIC system.	65
7.10	Comparison of overall efficiency, charging current of 100 mA. a) Open-loop NRIC. b) Closed-loop NRIC system.	66
7.11	Comparison of overall efficiency, charging current 10 mA. a) Air interposed. b) Animal tissue interposed.	68
7.12	Comparison of overall efficiency, charging current 25 mA. a) Air interposed. b) Animal tissue interposed.	69
7.13	a) Lateral misalignments configuration. b) Angular misalignments configuration.	70
7.14	Overall efficiency compared to lateral misalignments and battery voltage a) Charging current 10 mA. b) Charging current 25 mA. . .	71
7.15	Overall efficiency with angular misalignments and battery voltage a) Charging current of 10 mA. b) Charging current of 25 mA.	72
7.16	Test bench of recharges.	73
7.17	Battery recharge with closed-loop system. Charging current in blue and battery voltage in red. Coils distance 10 mm. a) LIR2016, charging current of 10 mA. b) LIR2025, charging current of 10 mA. c) LIR2025, charging current of 25 mA. d) LIR2032, charging current of 25 mA.	75
7.18	PTH variation during recharge. The PTH pin voltage (red) and current (blue). a) LIR2016, charging current of 10 mA. b) LIR2025, charging current of 10 mA. c) LIR2025, charging current of 25 mA. d) LIR2032, charging current of 25 mA.	76
7.19	Temperature monitoring during LIR2025 battery recharge at 25 mA. Coils distance of 10 mm. a) Tx coil temperature trend during recharge. b) Rx coil temperature. c) Rx IC temperature.	77
7.20	The temperature trend of Tx coil for 4 recharging modalities tested (air and animal tissue interposed, 10 and 25 mA charging current).	78

Chapter 1

Introduction

Since the first pacemaker had been implanted in 1958 [1], technological development has brought major and significant breakthroughs in the world of implantable devices. Great challenges have been faced while realizing safe implantable devices: the search for biocompatible materials, proper size and durability of batteries, the functionality, and wireless communication. Progress in implantable devices goes hand in hand with the technological development of electronics and microsystems. Over the last 50 years, advances have shown how an implantable device can improve a patient's living conditions. The ever-growing biomedical market also shows how important it is to push forward in this field, implementing new and more efficient solutions. The world of implantable devices moves towards the direction of smaller and less invasive devices, which have low power consumption, and are reliable and safe. There is also a strong focus on e-health: the implanted device must communicate with an external device and be continuously regulated via remote control to improve the device's therapeutic effectiveness.

One of the remaining challenges is the power supply for implantable devices. New implanted devices implement increasingly smaller batteries that need to be recharged periodically. On the other hand, other devices do not implant batteries, but the energy source is transmitted wireless from external sources. Research into new types of power supplies is the basis for the new generation of active medical devices focused on replacing bulky batteries.

This dissertation presents the study of wireless power transfer (WPT) using a near-field resonant inductive coupling (NRIC) system to power a subcutaneous implant device.

Chapter 2 looks at the different power supply types for implantable devices, focusing on the different wireless power transfer methods.

Chapter 3 introduces two new implantable devices (Nanofluidic drug delivery, Senseback), highlighting the main power supply issues and requirements. The NRIC system proved to be the most suitable, and several ICs were examined to choose the most suitable one.

Chapter 4 and 5 describe the chosen receiver and the chosen transmitter respectively, highlighting their main functionalities. Chapter 5 also focuses on the electrical schematic and the Optimum Power Search.

Chapter 6 presents the test results on overall efficiency of NRIC system in the most favorable transmission conditions (perfectly aligned coils). The chapter also highlights transmission problems due to implementation of the transmitter.

Chapter 7 illustrates the implementation of a closed-loop NRIC system to improve power transmission, and avoid transmission problems. The tests performed in the previous chapter are repeated, showing an improvement in overall efficiency. Subsequently, further tests were performed to simulate more realistic conditions of an implant and to define the operability limits of the NRIC system. These additional tests imply the use an animal tissue interposed between the coils to stimulate the skin and the lateral and angular displacement. Finally, three lithium batteries were recharged to validate the system. The temperature of the coils and the receiver IC was monitored during the recharging phase.

Chapter 8 presents conclusions and future perspectives.

Chapter 2

State of the art

2.1 Active implantable medical devices

Active implantable medical devices (AIMDs) are used to study, treat or monitor dysfunctional organs, and it is possible to implant them in different areas of the body [2]. Nowadays, there are different types of AIMDs available on the market (fig. 2.1) and many others under study. Examples of commercially AIMDs are cardiac pacemakers, implantable cardioverter-defibrillators (ICDs), implantable cardiac monitors (ICMs), cochlear implants, retinal implants, phrenic nerve stimulation (PNS), deep brain stimulation (DBS), gastric stimulators, and implantable infusion pumps. In some of these devices, most of the space is occupied by batteries. These devices are too large to be directly implanted in the specific organ: they are, indeed, implanted under the skin and stimulate the affected organ through the use of catheters. For the new generation of AIMDs, technological advancement in electronic and micro and nanofabrication is going in the direction of reduction of size and power consumption and improvement of therapeutic efficacy and safety. Those devices are becoming more compact and no longer require the use of catheters but can be directly implanted on the affected organ. The new AIMDs can incorporate microfabricated components or can be completely microfabricated. The wireless pressure measurement system from CardioMEMS, Inc (fig 2.2) is the first microelectronic mechanical system (MEMS) that has received Food and Drug Administration (FDA)-approval [1]. Ho et al. [4] investigated the use of an electro stimulator implanted directly in the heart. The device shown in figure 2.3a is 2 mm in diameter, weighs 2 mg, capable of generating $2.4 \mu\text{J}$. As shown in figure 2.3b, the size of the devices is progressively decreasing.

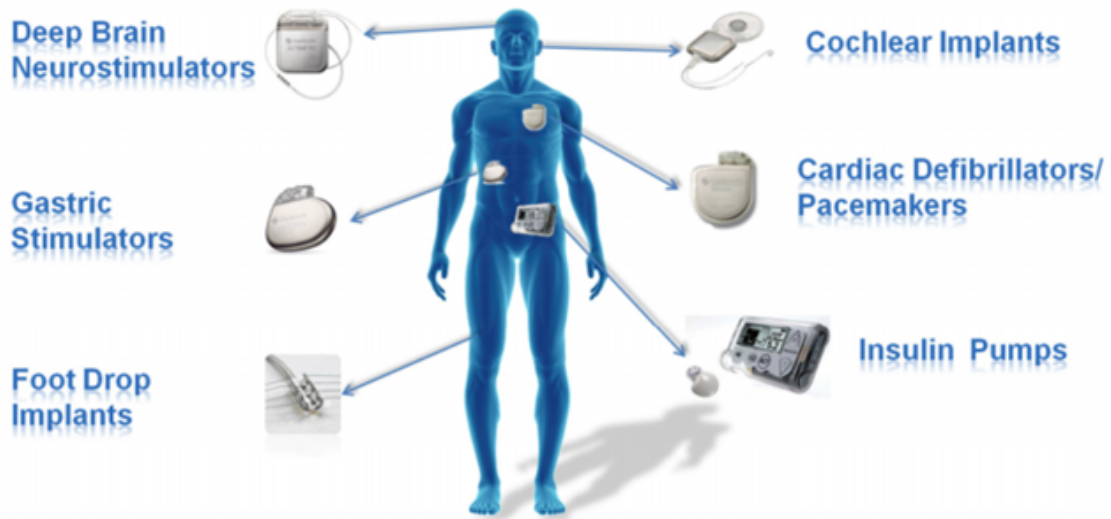


Figure 2.1: Active implantable medical devices (AIMDs) [3].



Figure 2.2: CardioMems [1].

2.2 Power supply approaches

To ensure proper operation, AIMDs needs a permanent and sufficient power supply. The energy source is divided into three categories:

- Primary batteries: the first energy source used to power AIMDs and the most widely used. Lithium-based batteries are the most commonly used with AIMDs thanks to their high volumetric density capacity and considerably durable longevity of 5 to 10 years [5]. According to the requirements of AIMD, there are different types of battery:
 - Lithium-iodine (Li-I₂) batteries, which are employed in pacemakers;
 - Lithium-thionyl-chloride (Li/SOCl₂) batteries, which are employed in neurostimulator and drug pumps;



Figure 2.3: a) Electro stimulator miniaturized [4]. b) Battery-powered pacemaker (Left; Medtronic Adapta), battery-powered swallowable endoscope (Center), Electro stimulator (Right) [4].

- Lithium-silver vanadium oxide (Li-SVO) batteries, which are employed in ICDs;
- Lithium-carbon monofluoride (Li-Cfx) batteries;
- Lithium-manganese oxide (Li-MnO₂) batteries;

It is not possible to produce micro batteries with high capacity. In addition to this, the battery life is limited, and once exhausted, the device must be explanted. New solutions have been investigated to cope with these problems.

- Energy-harvesting: the idea is to collect the energy by exploiting the human body's movements or chemistry. In this way, AIMDs can be battery free or even have a secondary battery implanted that can be recharged. Canan Dagdevirena et al. [6], have shown how it is possible to convert motions of heart, lung, and diaphragm into electrical energy by exploiting the properties of piezoelectric materials. Benjamin I. Rapoport et al. have developed an implantable fuel cell that generates power through glucose oxidation [7]. Other possibilities include the extraction of thermoelectric [8] and biopotential energy [9]. However, these solutions allow producing relatively low power densities below $0.1 \frac{\mu\text{W}}{\text{m}^2}$ [4].
- Wireless power transfer (WPT): the idea is to transfer energy from the outside of the body to the inside without wires. AIMDs come equipped with a receiver, and the power is transferred through the use of an external transmitter. This way, AIMDs can be implanted without the battery, and the power supply is given by an external source or with rechargeable batteries that are recharged periodically, always using the external source. This topic will be further developed in the next section.

2.3 Wireless power transfer (WPT)

Wireless power transfer (WPT) systems were made possible by Michael Faraday's discovery of electromagnetic induction in 1831 and further developed thanks to the pioneering work of Heinrich Hertz and Nikola Tesla. Tesla made a significant contribution to the efficiency of the WPT by working with resonant coupling. In the last few decades, thanks to the technological advancement in electronics and micro and nanofabrication, WPT systems have been very successful in different applications, particularly in that of AIMDs. WPT systems allow the transfer of power to implantable devices using an external transmitter and an implantable receiver. This way, no transdermal wire is used, thus avoiding biocompatibility problems. Another advantage of WPT systems is the possibility of implanting devices without a battery or with a rechargeable battery, thus avoiding replacing the implant in case of battery power depletion. In the literature [2]-[10] there are different types of technologies used to implement WPT systems:

- Near-field resonant inductive coupling (NRIC);
- Near-field Capacitive Coupling (NCC);
- Ultrasound based wireless systems;
- Solar power harvesting;
- Electromagnetic Mid-Field based systems;
- Electromagnetic Far-Field based systems.

A wireless power transfer system can be defined as any system capable of transferring electrical power without using a solid connection [11]. The principle of transmitting power by EM field is the most popular, but in the last decades, new principles have been adopted, such as acoustic links and solar energy harvesting. For systems that exploit the propagation of EM waves, it is possible to divide three propagation regions: near, mid, and far-field [12] (fig. 2.4).

- The near field is also called the reactive near-field region and is defined as *“that portion of the near-field region immediately surrounding the antenna wherein the reactive field predominates”* [12]. The border of this region is defined as $R < 0.62\sqrt{\frac{D^3}{\lambda}}$. D is the largest dimension of an antenna, and λ is the wavelength at the operating frequency. In the free space, the electric and magnetic near field can be calculated independently.
- The mid-field is also called Radiating near-field (Fresnel) region and is defined as *“that region of the field of an antenna between the reactive near-field region and the far-field region wherein radiation fields predominate and wherein the*

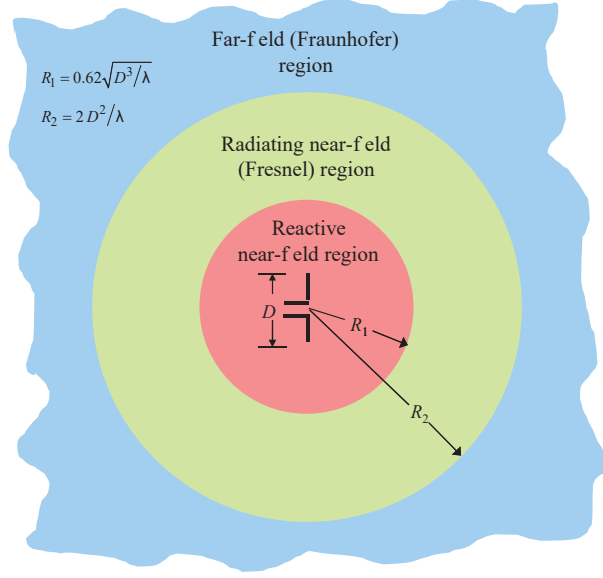


Figure 2.4: Region of EM field propagation [12].

angular field distribution is dependent upon the distance from the antenna” [12]. The inner boundary is defined as $0.62\sqrt{\frac{D^3}{\lambda}} < R < \frac{2D^2}{\lambda}$.

- The far-field is also called Fraunhofer region and is defined as “*that region of the field of an antenna where the angular field distribution is essentially independent of the distance from the antenna*” [12]. The far-field region exists at distances greater than $R > \frac{2D^2}{\lambda}$. In this region exist an interaction between the electric and the magnetic field.

2.3.1 Near-field resonant inductive coupling (NRIC)

The NRIC (fig. 2.5) is the most common and most studied wireless power transfer system. It is based on the use of a primary coil transmitter (Tx) that generates a variable magnetic field over time by inducing an electromagnetic force (ε) in the secondary coil receiver (Rx). The electromagnetic force is given by equation 2.1:

$$\varepsilon = -\frac{d}{dt} \int_{\Sigma} \vec{B} d\vec{A} \quad (2.1)$$

Where Σ is the surface of the receiver, B is the magnetic flux density, and A is the area vector [11],[14]. The NRIC system allows transmitting power in a range from a few mm up to about a few tens of mm, using a range of operating frequencies from few hundreds of kHz to few tens of MHz. The magnetic field intensity decreases as the distance between the two coils increases. Besides, for frequencies above 100 kHz, the magnetic field is attenuated by the tissues [15]. For these reasons, the NRIC

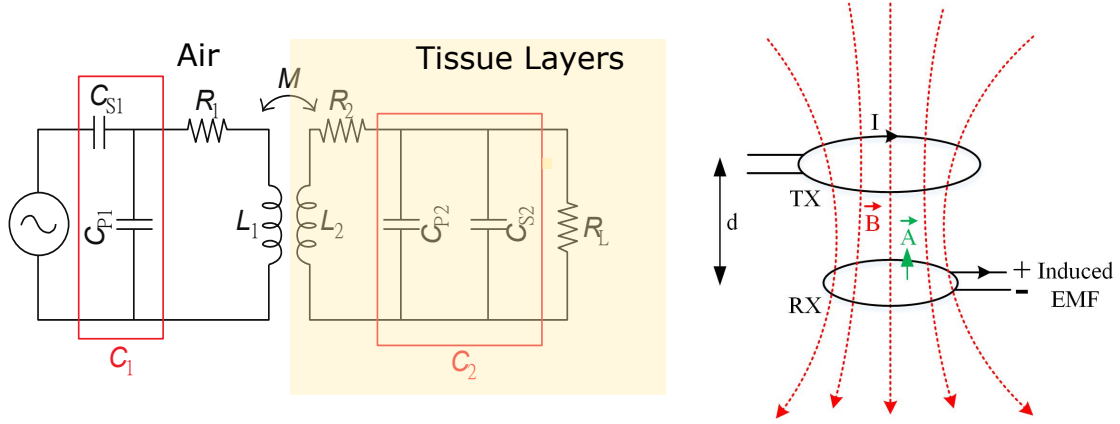


Figure 2.5: NRIC scheme [2] [13].

system's use is limited for WPT systems that require a maximum sweep of a few tens of mm. The power transfer efficiency (PTE) is used to evaluate the wireless power transfer link [13]. The power transfer efficiency of the NRIC system is given by 2.2:

$$PTE = \frac{k^2 Q_1 Q_2}{1 + k^2 Q_1 Q_2 + \frac{Q_2}{Q_L}} \times \frac{1}{1 + \frac{Q_2}{Q_L}} \quad (2.2)$$

where the quality factor of the transmitter (Q_1), receiver (Q_2), and load (Q_L) are given by 2.3:

$$\begin{aligned} Q_1 &= \frac{\omega_0 L_1}{R_1} \\ Q_2 &= \frac{\omega_0 L_2}{R_2} \\ Q_L &= \frac{R_L}{\omega_0 L_2} \end{aligned} \quad (2.3)$$

The resonant coupling provides better efficiency than the classic inductive coupling. It is achieved when the transmitter and receiver are tuned to the same frequency according to the equation 2.4:

$$f = \frac{1}{2\pi\sqrt{L_1 C_1}} = \frac{1}{2\pi\sqrt{L_2 C_2}} \quad (2.4)$$

The resonant coupling cancels out the contribution of the inductive part in the Rx circuit [11]. There are four typologies of resonant coupling: SS/SP/PS/PP, where the first letter indicates the type of compensation in the transmitter (series/parallel) and the second letter indicates the type of resonant in the receiver (series/parallel) [16]. SS and SP (fig. 2.6) deliver the same power, but SS works using a large current and low voltage, while SP works using a low current and large voltage [14].

The rectifier used to convert alternative current (AC) to direct current (DC) has a better efficiency when working with large voltage. For this reason, the SP resonant coupling is widely used in biomedical applications [16].

PTE is the most important parameter to take into account when using a WPT

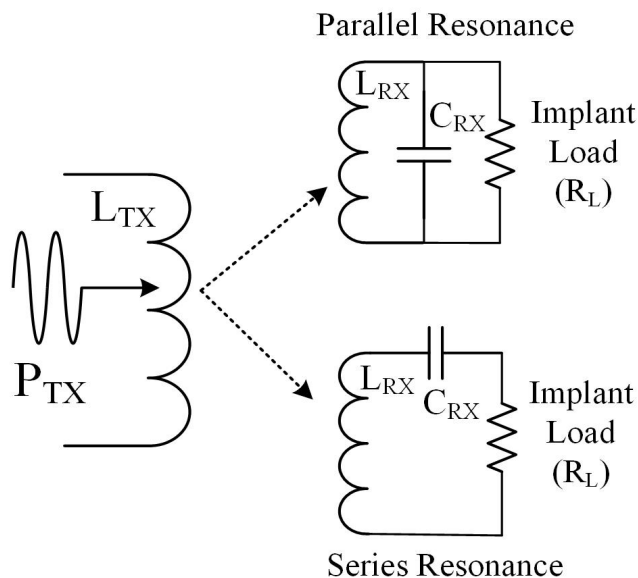


Figure 2.6: Serial and Parallel resonant coupling [2].

system: an optimal efficiency allows to dissipate less power and avoid overheating problems. When using NRIC systems, different problems arise: misalignments between the transmitter and receiver can cause the decrease of PTE; and load variation and detuning due to modification of the geometry of flexible coils can cause a swing of PTE. In the literature, there are several solutions to the problems reported above:

- In [17], they design, compare and optimize a 2-, 3-, and 4-coil inductive link to achieve high PTE values at a larger separation of coils. The results show that using 3-coil results in a power transfer efficiency of 37% compared to 15% and 35% with 2- and 4-coil. While in terms of power delivered to the load, the 3-coil inductive link is 59 and 1.5 times higher than 4-coil and 2-coil inductive link, respectively;
- In [18] and [19], magnets were used to improve the coupling between the coils and to limit the problems caused by the misalignment of the coils. Suspended magnets are used because they are compatible with magnetic resonant imaging (MRI) up to 3 T;
- A closed-loop system for power transfer management is presented in [20]. The back telemetry is used as a feedback system to control and adapt the power

transmission to different transmission conditions. The results show that the power on the load was maintained at 11.2 mW changing the coils' distance from 0.5 to 2 cm;

- In [21] the development of miniaturized flexible coils is presented. Miniature coils with less inductance per area minimize the reduction in PTE due to flexing and stretching. The coil is developed on polyethylene terephthalate, with thin gold traces;
- In [22], the study carried out on the optimization of printed spiral coils (PSCs) for devices with extreme size constraints is presented. The coils were optimized, taking into account the contribution of the interposed tissue (air, saline, and muscle tissue). They achieve transmission efficiencies of 72.2% 51.8% and 30.8% with a relative spacing of 10 mm for air, saline, and muscle tissue, respectively;
- A system for transferring power to multiple millimeter-sized wireless implants was presented in [23]. They proposed 1- and 2-tier resonator coupled inductive links to distribute the transmitted power uniformly. They propose also two new strategies: scalable resonator array and self-regulated power management circuit. They achieve a PTE of 11.9%, whilst reducing the power distribution deviation to 1.77%.

2.3.2 Near-field Capacitive Coupling (NCC)

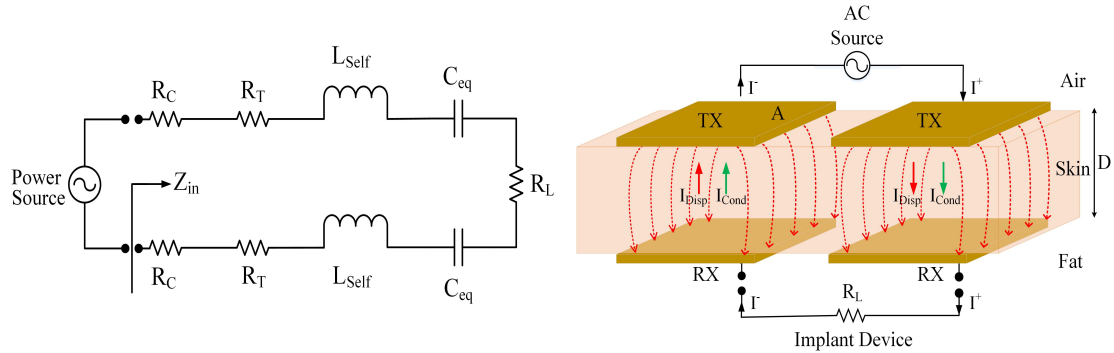


Figure 2.7: NCC scheme [2].

The NCC system [24] (fig. 2.7) works on the principle of electric field coupling between two pair of conductors, for forward and reverse currents. The electric field between the two conductors generates two types of currents: one of displacement (eq. 2.5) and one of conduction (eq. 2.6).

$$I_{disp} = \epsilon_0 \epsilon_r(\omega) A \frac{\partial \vec{E}}{\partial t} \quad (2.5)$$

$$I_{cond} = \frac{V(t)\sigma(\omega)A}{D} \quad (2.6)$$

Where ϵ_0 is vacuum permittivity, $\epsilon_r(\omega)$ and $\sigma(\omega)$ are frequency-dependent permittivity and conductivity of the skin; A is the area of the patches and D is the distance between the patches, V(t) is the sinusoidal voltage and \vec{E} is the electric field between the patches. The transmission system has good performance if the displacement current is high and the conduction current is low, as this last one causes tissue losses and overheating. The NCC system allows transmitting power in a range of a few mm, using an operating frequency range that goes from few tens of MHz to sub-GHz. The NCC system, like the NRIC, can transfer the power of the order of hundreds of mW. However, if compared to the NRIC system, NCC has some advantages: it is a low-cost technology, it is less affected by lateral and angular misalignment, it reduces electromagnetic interference because the two patches well delimit the electric field, and it has greater flexibility [25],[26]. On the other hand, PTE is defined by equation 2.7:

$$PTE = \frac{R_L}{R_L + R_T}(1 - |\Gamma|^2) \quad (2.7)$$

where R_L is the load resistor, Γ is the reflection coefficient, and R_T is the tissue loss given by equation 2.8:

$$R_T = Real\left(\frac{-jD}{\omega\epsilon_0\epsilon_r(\omega)A}\right) \quad (2.8)$$

High frequencies must be used to achieve good PTE and decrease the impedance of the tissue. But the rectification at high frequencies (over 30 Mhz) is less efficient compared to low frequency [2]. According to equation 2.7, the PTE is also affected by the small variation of the patches distance and area. Moreover, the NCC is in the preliminary state of study, and there are no long-term safety studies, yet [2].

2.3.3 Ultrasound based wireless systems

This system uses ultrasonic waves to transfer power through the tissue. The ultrasonic waves are mechanical waves that need a physical medium to be transmitted and that are generated by exploiting the properties of piezoelectric materials, which transform electrical energy into mechanical energy and vice versa. Therefore, the transmitter and the receiver are made both of piezoelectric crystals. The transmitter is electrically excited to generate the ultrasound, and the implanted receiver converts the ultrasound into electrical energy. The ultrasound system (fig. 2.8) allows transmitting power in a range from a few mm up to about 100 mm, using an operating frequency range which goes from few hundreds of kHz to a few MHz [2],[5].

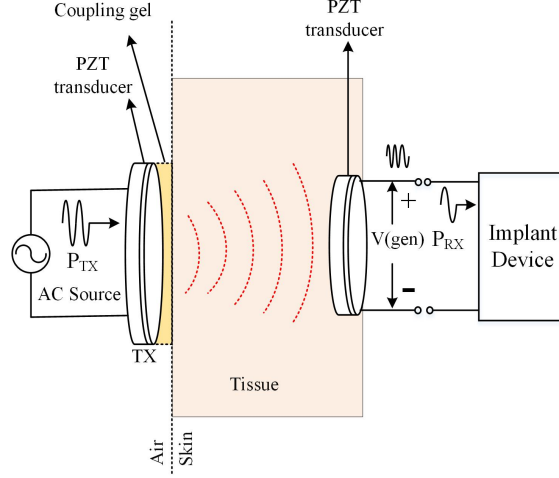


Figure 2.8: Ultrasound based WPT systems [2].

This new system has been successful in power transmission. Indeed, in [27] a PTE of 82% is reported, which guarantees powers of the order of hundreds of μW even in deeply implanted devices ($> 20 \text{ mm}$). Furthermore, it can be implemented in miniaturized implantable devices (6.5 mm^3), thanks to the piezoelectric receiver's small size. On the other hand, the PTE is only good if certain specifications are met. Indeed many factors influence the efficiency of the ultrasound system [2], [26]:

- Part of the transmitted wave is absorbed by the tissue according to Lambert-Beer's law (eq. 2.9):

$$I_d = I_0 e^{-2\alpha d} \quad (2.9)$$

Where I_0 and I_d is the intensity of the wave before and after, d is the thickness of the tissue and α is the absorption coefficient;

- The acoustic impedance mismatch is related to different characteristics and properties of tissues and occurs at each interface, but it is dominated at the PZT-tissue boundary. The reflection coefficient is given by equation 2.10:

$$\Gamma = \left| \frac{Z_{tissue} - Z_{pzt}}{Z_{tissue} + Z_{pzt}} \right| \quad (2.10)$$

The intensity of the transmitted wave is proportional to $(1 - \Gamma^2)$, therefore drastically drops for an unmatched transducer;

- The PZT manufacturing process is essential for mechanical and electrical power conversion efficiency (PCE). In particular, piezoelectric micromachined ultrasonic transducers (PMUTs) have better PCE compared to commercial off-the-shelf PZT;

- The propagation of acoustic waves can be divided into three zones (fig. 2.9): The near field, the far-field, and the focus zone between the near and far field [2]. The focus zone is the preferred location to implant the receiver and to maximize the PTE, and it is given by the Rayleigh distance (L) mathematically expressed in equation 2.11:

$$L = \frac{D^2 - \lambda^2}{4\lambda} \quad (2.11)$$

where D is the diameter of Tx PZT and λ is the sound propagation in the medium. The near field region is characterized by a variable acoustic wave that causes an oscillation of PTE. The PTE is sensitive to small variations in the distance between the receiver and the transmitter; this does not make the ultrasound system suitable for subcutaneous implants.

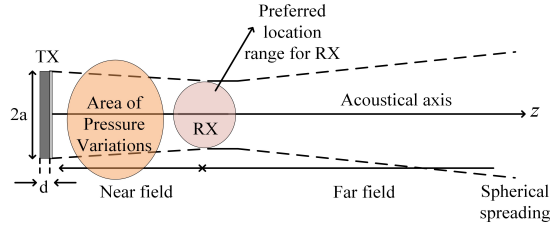


Figure 2.9: Representation of acoustic wave propagation.

Therefore, ultrasonic power transfer performs well in terms of efficiency but is only suitable for use in the presence of homogeneous tissues. The ultrasound system is still being tested and lacks long-term side-effects studies [28]. However, it is well known that the main side effect of ultrasonic wave is the cavitation phenomenon, which can cause cell membrane rupture.

2.3.4 Solar power harvesting

Thanks to the use of miniaturized photovoltaic cells, the solar power harvesting (fig. 2.10) can be used in active implantable medical devices like a WPT system. This new WPT system would theoretically allow to have battery-less devices with unlimited life. The photovoltaic cell is able to power the AIMD by converting an external light source in electric current [30]. When using this system in a subcutaneous implant, the main problems concern dark conditions, which would not allow the device to be powered, and power losses due to the tissue. Indeed, the tissue absorbs most of the energy in the visible range, while it is more transparent in the infrared range [29],[31]. The tissue interposed between the photovoltaic cell and the light source causes a drastic reduction of PTE and energy instability, guaranteeing a power supply for the ultra-low power devices only.

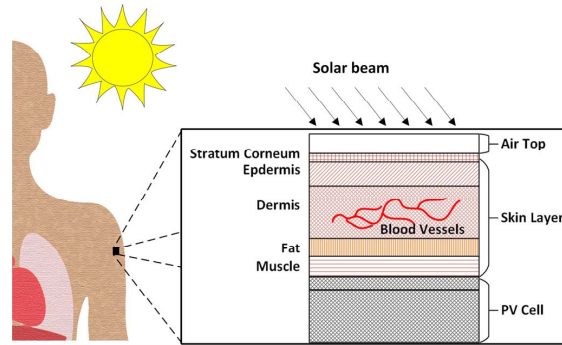


Figure 2.10: Solar power harvesting [29].

2.3.5 Electromagnetic Mid-Field based systems

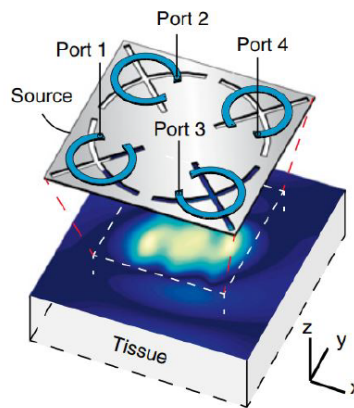


Figure 2.11: Mid-field WPT system [4].

The Mid-field WPT system (fig. 2.11) is an optimal solution to transmit power to all those implantable devices that have the following characteristics:

- The size of Rx coil is much less of wavelength at mid-field frequency range, typical in micro-implants;
- The Tx and Rx coils are separated by order of one wavelength at mid-field range. (*"Few centimetres when the operating range lies at low-GHz range"* [2]);
- Low power (μW).

According to Jhon et al. [32], the midfield frequency for miniaturized weakly coupled coil implants allows for better efficiency than the classic NRIC system. Higher

frequency is used typically at the low-GHz range to obtain better efficiency. At high frequencies, the dielectric relaxation loss of the tissue is the dominant loss mechanism [33]. The impact of this increased tissue loss on the human body needs to be analyzed carefully yet [34]. In addition to this, the mid-field system allows transferring the power of the order of μW , therefore, only for ultra-low power devices.

2.3.6 Electromagnetic Far-Field based systems

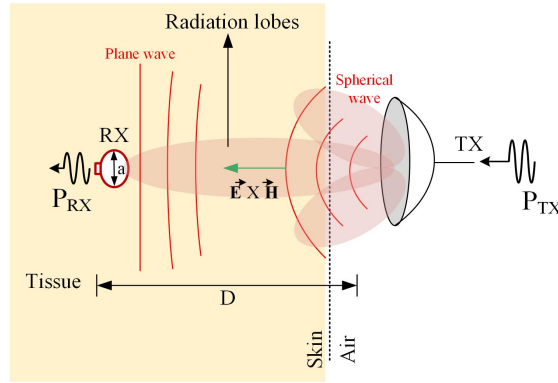


Figure 2.12: Far-field WPT system [2].

The Far-field WPT system (fig. 2.12) works on the principle of the electromagnetic field. It is considered Far-field when the distance R between the receiver and transmitter is major of $\frac{2D^2}{\lambda}$. Where D is the diameter of the receiver, and λ is the wavelength of the electromagnetic field. In the Far-field region, the electromagnetic field is approximated by the planar wave. The radiated wave generates the alternating current in the receiver. After the rectification, the current is used by implant devices. The frequency used lies in the GHz range, and the link allows transfer power over a few tens of mm. To quantify the overall power receive P_R , the Friis' law 2.12 is used [35]:

$$P_R = |S_{12}|^2 \times P_T \quad (2.12)$$

where $|S_{12}|$ is the transmission coefficient and P_T is the power of the transmitter. As we can see, the PTE depends on the transmission coefficient that is influenced by different parameters such as:

- Directionality;
- Tx and Rx antennas efficiency;
- Impedance mismatching;

- RF to DC converter.

It is very difficult to miniaturize antennas and maintain high efficiency. With the size decrease of antennas, the bandwidth reduces, and the radiative resistance becomes lower than loss resistance, thus reducing the efficiency. The immersion lens are used to focalize the Tx beam to the receiver and improve the efficiency. However, it is still an open challenge to use this system to power an implanted device. Now it is only possible to power devices that require ultra-low power [2],[36].

Chapter 3

Wireless power transfer for active implantable medical devices

There are different systems to power supply an active implantable medical device, which have previously been discussed and summarised in figure 3.1. This section presents two new AIMDs and discusses which wireless power transfer is the best to use.

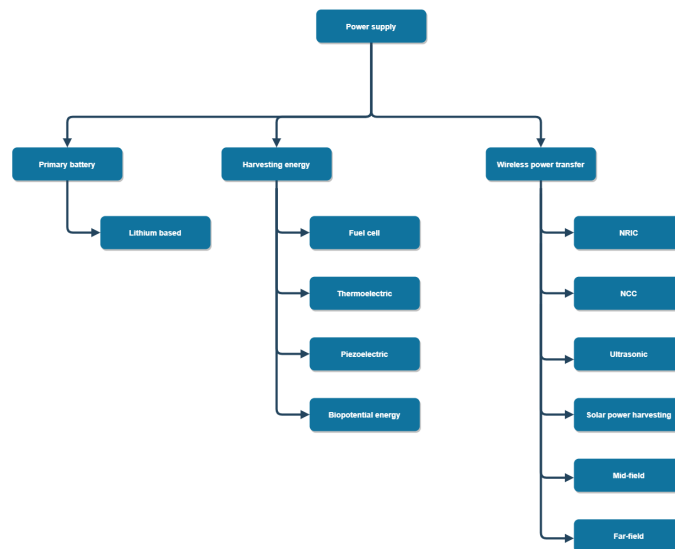


Figure 3.1: Summary of AIMDs power supply.

3.1 Nanofluidic drug delivery

The AIMD treated is a remotely controlled nanofluidic implantable platform for tunable drug delivery developed from Dr. Alessandro Grattoni's laboratory [37]. The device shown in figure 3.2 is entirely implantable subcutaneously. It allows the management of the release of drugs in a controlled way by adjusting the dosage and timing and avoiding abrupt changes in the dosage, which can compromise the therapy. Chronic diseases require personalized lifelong drug administration, and it is essential to manage the release in the best possible way. An optimal drug release schedule allows maximizing the efficiency of therapy, improving patients' quality of life, and reducing the side effects due to drugs.

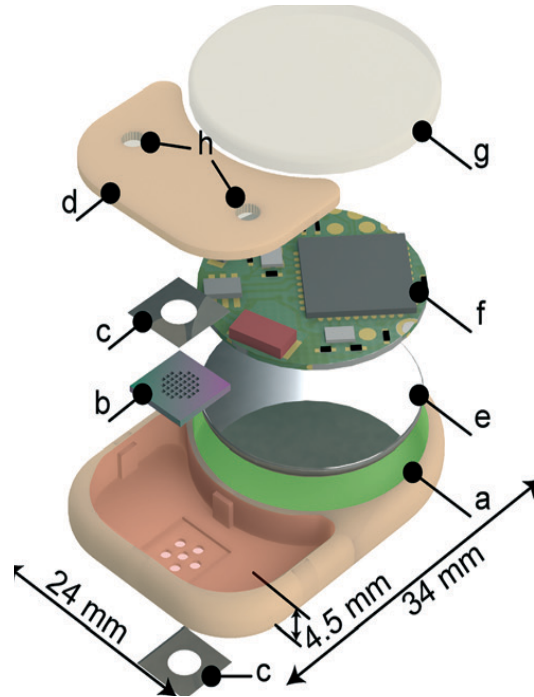


Figure 3.2: Nanofluidic implantable platform [37]. a) PEEK body. b) Silicon nanofluidic membrane. c) Pt foil electrodes. d) PEEK lid used to seal the reservoir. e) Battery. f) Printed circuit board. g) Epoxy sealant. h) Silicon drug filling port.

The nanofluidic silicon membrane is used to modulate the drug release rate, which is closed between two platinum electrodes (fig. 3.3). With the application of a small E-field across the membrane via Pt electrodes, ionic species are forced to redistribute or are electrophoretically driven across the nanochannel. If the E-field is not applied, drug release is due to the concentration gradient between the reservoirs and the subcutaneous space. Finally, low energy Bluetooth communication is employed to remote control the drug release and dosing for each patient.

The power consumption is of the order of a few hundred μW , except during the

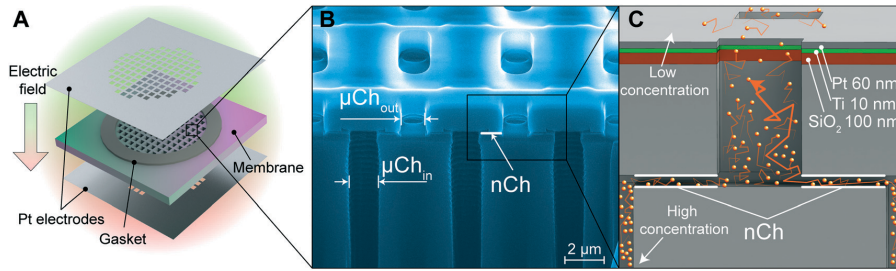


Figure 3.3: Silicon nanofluidic membrane [37]. a) Schematic of the nanofluidic membrane. b) FIB-SEM image of the nanofluidic membrane. c) Schematic of the deposited electrode.

connection between the implant and server, where the power consumption is of the order of a few mW. A primary battery, CR2016 (VARTA), which has a capacity of 90 mAh (270 mWh), is employed to supply the system. The lifespan of the battery is estimated at almost 20 days in the high power consumption scenario.

It is possible to replace the primary battery with a secondary one and recharge it with a wireless system to solve this problem.

3.2 SenseBack

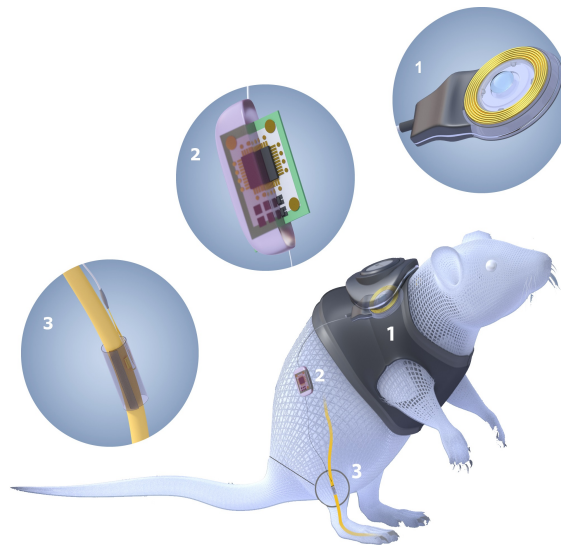


Figure 3.4: SenseBack system [38]. 1) Inductive link. 2) Bidirectional neural interface. 3) Microelectrode array.

Prosthetic arms are controlled by activating specific muscles in the stump to which the prosthesis is attached. Despite this, the amputee has no sensation of

the prosthetic limb, making its use more complex and less natural. The Senseback project [38], developed by the Imperial College, aims to provide artificial sensory feedback to prosthetic limb users. Their work focuses on proprioceptive and tactile feedback to develop technologies that will enable the next generation of assistive devices to provide truly natural control through enhanced sensory feedback. The system (fig. 3.4) has three main components:

1. Inductive link for power and data transfer;
2. Implanted Bidirectional neural interface;
3. Flexible, biocompatible penetrating microelectrode array, implanted on a peripheral nerve.

The bidirectional neural interface ASIC is the heart of the implant [39]. The ASIC has 32 channels and can perform high-voltage neural stimulation or acquiring neural or electromyographic signals. ASIC aims to stimulate with artificial signals that mimic those of the hand or arm of the amputee's nervous system. The implanted device consumes 113 mW while recording and wirelessly streaming data from 16 channels. The power transfer system has been implemented using resonant coupling (NRIC), the P9235A-R integrated circuit for the transmitter and the P9027LP-R integrated circuit for the receiver. The analysis reported in [38] shows that the power transfer efficiency is around 20% with a significant portion of energy dissipated as heat. Figure 3.5 shows the thermal image of the wireless power receiver, highlighting the unacceptable levels of heating.

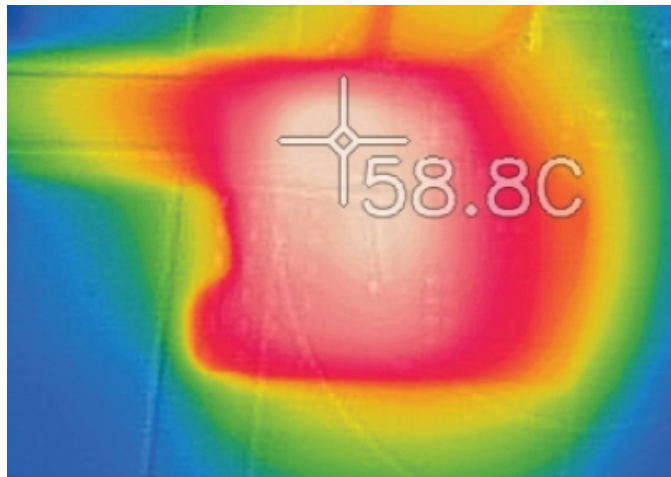


Figure 3.5: Thermal image of wireless power receiver (P9027LP-R) [38].

3.3 Wireless power transfer approaches trade-offs

Seven parameters have been considered to understand which is the best wireless power transfer system for the two AIMDs:

- The transmitted power must be greater than tens of mW;
- The PTE value must be as high as possible to have less dissipation, avoiding overheating;
- Flexibility, to allow better implantation of the coil;
- EMI immunity to prevent wireless charging from disturbing the device during operation;
- The size of the RX coil must be as small as possible to be least invasive;
- The better system for a subcutaneous implant;
- If the safety analysis of wireless power systems has been conducted.

The analysis summarized in table 3.1 shows that the most suitable system to use is near-field resonance inductive coupling (NRIC). The NRIC system is the most compatible with the devices under study. It allows to transmit power greater than hundreds of mW, and it is suitable for subcutaneous implants as the operating range is of the order of the thickness of the skin. The size of coils is suitable for integration into devices under study. Finally, the NRIC system has already been used in other implants, such as the cochlear one, and several safety studies have already been conducted.

WPT	Output power >mW	High PTE	Flexible	Immunity EMI	Rx size <2cm	Subcutaneous implant	Safety analysis
NRIC	✓	-	✓	-	✓	✓	✓
NCC	✓	-	✓	✓	-	✓	-
Ultrasonic	-	✓	-	✓	✓	-	-
Solar	-	-	-	✓	✓	✓	-
Mid-field	-	-	✓	-	✓	-	-
Far-field	-	-	✓	-	✓	-	-

Table 3.1: Quality comparison of wireless power transfer system.

3.4 Integrated Circuits ICs

The NRIC link is achieved by using a transmitter capable of generating a variable magnetic field to transmit power and a receiver capable of using this power to recharge the implanted battery or to supply the implanted device. Two ICs were selected: one for the transmitter and one for the receiver. The most problematic

among the two integrated circuits is the receiver since its purpose is to be implanted. For this reason, we have defined the following constraints for the receiver, which help in determining the best integrated circuit to use:

- Small size;
- Single IC with:
 - rectifier;
 - voltage regulator;
 - programmable linear battery charger;
- Low power dissipation.

The size of the IC and external components should be taken into account because a small overall size allows for less invasive implantable devices. In terms of space-saving, it would also be better to use a single IC with the features listed above instead of using one IC to handle the power and another to handle the recharging. A further characteristic to consider is the power dissipation of the integrated circuit. The dissipated power is linked to the rise in temperature of the device, which must be kept under control to avoid overheating of tissues surrounding the implanted device. The European Standard EN45502-1 limits the surface temperature of an implanted device to 2 °C above the body temperature of 37 °C [40].

3.4.1 Analysis of receiver ICs

We have compared six distinct receiver ICs that were considered compatible with the NRIC system. The ICs investigated are:

- XCM414 (Torex);
- BQ51003 (Texas instruments);
- TS51224 (Semtech);
- TS51223 (Semtech);
- LTC4124 (Analog Devices);
- LTC4126 (Analog Devices);
- P9027LP-R (Renesas).

ICs size

Figure 3.6 shows the size comparison of the ICs. Two axes were used, one to represent the total size of the receiver and one to indicate the number of passive external components to be added to the IC. The total size was calculated by considering the size of the integrated circuit, the passive components (excluding the coil), and considering the space between the components. The analysis shows that the IC with the smallest size and the least number of components is the LTC4124. It should also be noted that only the LTC4124, LTC4126, and TS51224 ICs include battery management, whereas the other ICs require a further IC to manage battery charging.

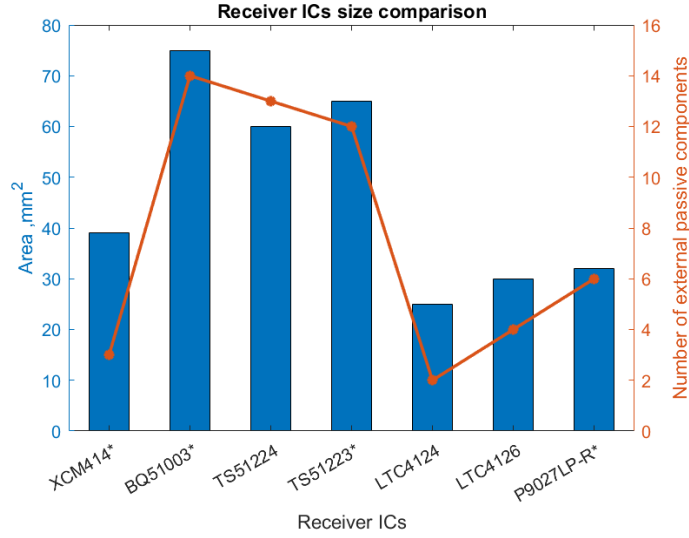


Figure 3.6: Wireless power receivers size comparison. *ICs without battery management.

Power dissipation

To evaluate the maximum power dissipation of ICs, we consider the junction to ambient thermal resistance $R_{\Theta JA}$, which is a measure of the thermal performance of an IC package. $R_{\Theta JA}$ intends to give a metric by which the relative thermal performance of a package can be compared. The temperature of the junction of the IC is related to the power dissipation (Pd) by the equation 3.1:

$$T_J = T_A + (R_{\Theta JA} \cdot Pd) \quad (3.1)$$

Knowing the maximum temperature difference that the implanted IC must have, it is possible to obtain the maximum dissipate power from the integrated circuit.

With the same dissipated power, the integrated with lower $R_{\Theta JA}$ will have a lower overheating. Table 3.2 shows the values of $R_{\Theta JA}$ for the ICs under study, with the relative power consumed considering a maximum temperature rise of 2 °C.

ICs	XCM414	BQ51003	TS51224	TS51223	LTC4124	LTC4126	P9027LP-R
$R_{\Theta JA}$ (°C/W)	71.43	58.9	N/A	N/A	92	92	72
Pd (mW)	28	34	N/A	N/A	22	22	28

Table 3.2: ICs power dissipation evaluation.

The receiver IC comparison

The main features considered for choosing the best IC are summarized in Table 3.3. The most compliant ICs are LTC4124 and LTC4126. LTC4124, compared to LTC4126, provides different charging modes with different charge current and charge voltage. Therefore, the LTC4124 IC was chosen for the receiver part of the NRIC system.

Receiver ICs	XCM414	BQ51003	TS51224	TS51223	LTC4124	LTC4126	P9027LP-R
Small Area <40 mm ²	√	-	-	-	√	√	√
$R_{\Theta JA}$	-	√	-	-	-	-	-
Single IC	-	-	√	-	√	√	-

Table 3.3: Summary ICs evaluation.

3.4.2 Analysis of transmitter ICs

The transmitter must be compatible with the selected receiver and must transmit power at a distance of at least 10 mm with interposed air. Analog Devices recommends using two integrated circuits, either LTC4125 or LTC6990, compatible with LTC4124.

The LTC6990 is a precision silicon oscillator with a programmable frequency range of 488 Hz to 2 MHz. It implements a DC/AC converter by using its oscillator to drive the NMOS switch connected to the LC tank.

While LTC4125 is a high-performance monolithic full bridge resonant driver capable of delivering 5 W of power, LTC4125 automatically adjusts its driving frequency matching the LC resonant frequency. Moreover, LTC4125 also includes an optimum power search to deliver the correct power to the receiver.

The LTC4125 is the best performing and most compatible with the requirements. The DC2770A-B evaluation kit was used to test the NRIC system’s operation with the two chosen ICs. In the next section, the functions of the chosen ICs will be analyzed, starting with the receiver.

Chapter 4

NRIC power receiver

The LTC4124 [41] is a high-performance wireless Li-Ion charger with a minimum number of required passive components and low battery disconnect. Figure 4.1 shows the electrical schematic of the receiver.

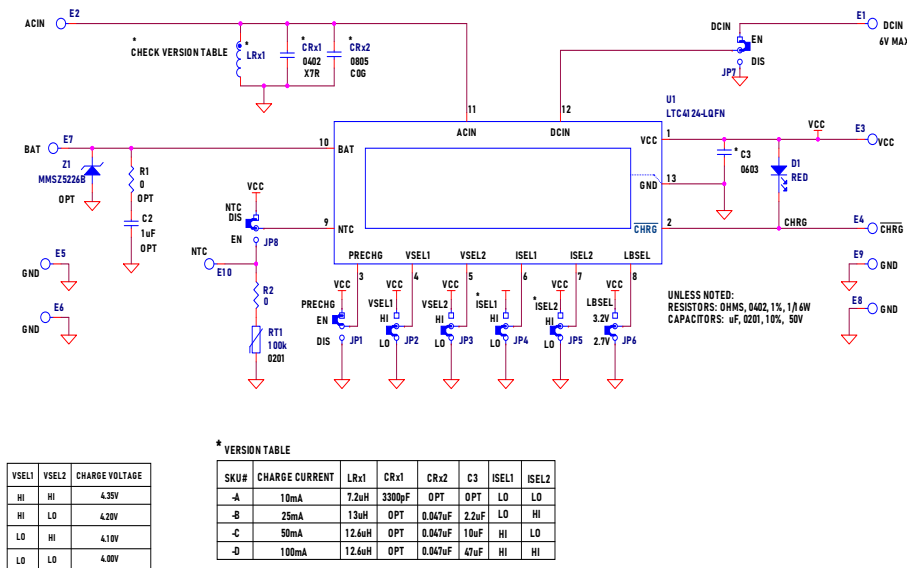


Figure 4.1: LTC4124 electrical schematic, D version [42].

The main features of the receiver are listed below:

- Wireless Input Power Control and Rectification;
- Pin-Selectable charge current and voltage;
- NTC input to qualify temperature charging;
- Li-Ion Charger Controller .

- PowerPath Controller

The functional block diagram 4.2 reports a simplification of how LTC4124 works and it describes the main functions and interrelationships of the IC.

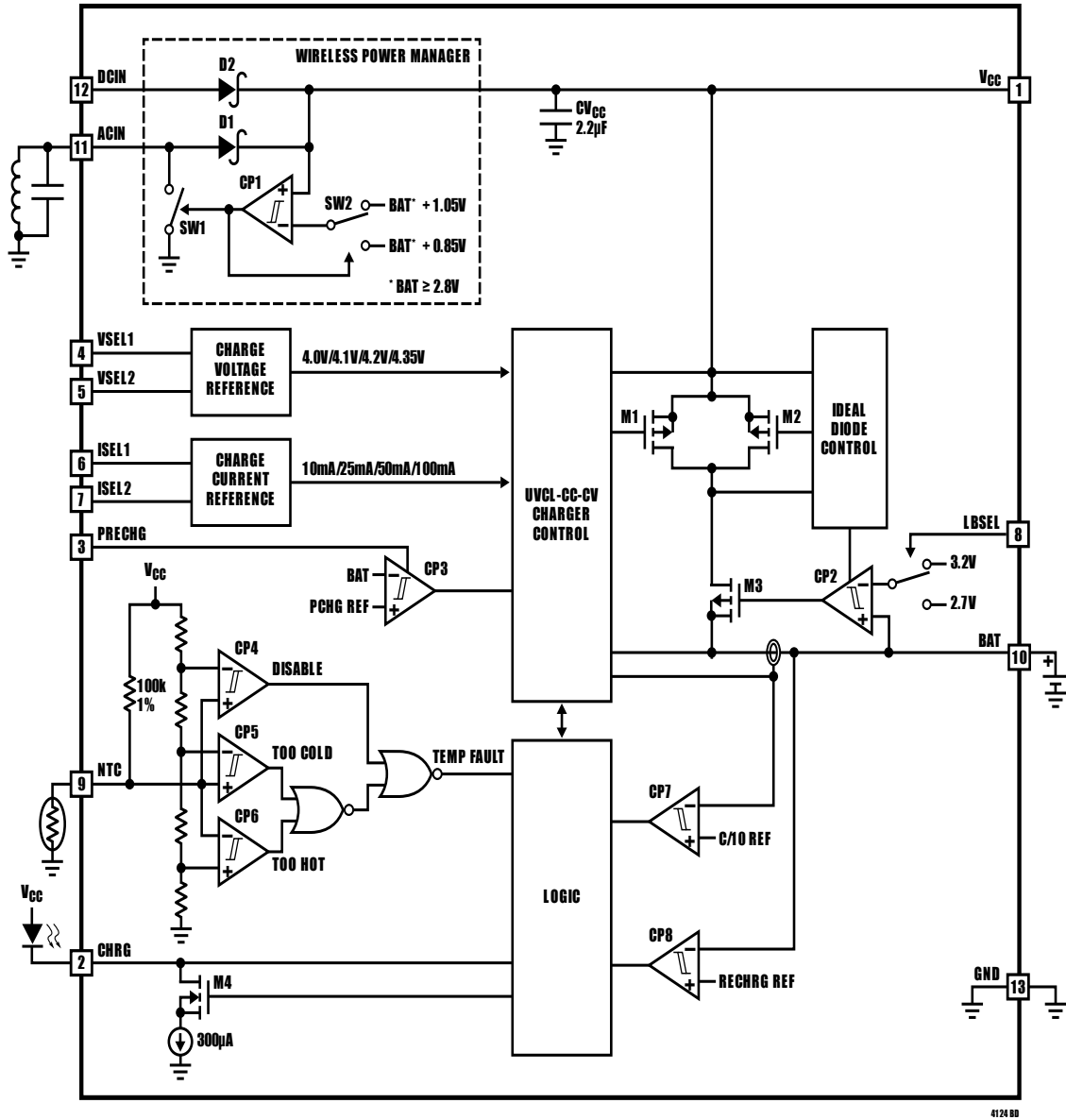


Figure 4.2: LTC4124 functional block diagram [41].

4.1 Wireless input power control

The system involves the use of a complete power receiver system composed of a coil and a capacitor in parallel. The coil (WURTH ELEKTRONIK, 760308101220) has an inductance of $12.6 \mu\text{H}$, a diameter of 17 mm, and a thickness of 0.8 mm. A capacitor of $0.047 \mu\text{F}$ was used to achieve a resonant frequency of the LC tank of 200 kHz. At this frequency, the quality factor of the coil is 25, as shown in figure 4.3. The quality factor is a fundamental parameter as it is the ratio between the energy stored in the oscillating resonator and the energy dissipated per cycle by damping processes.

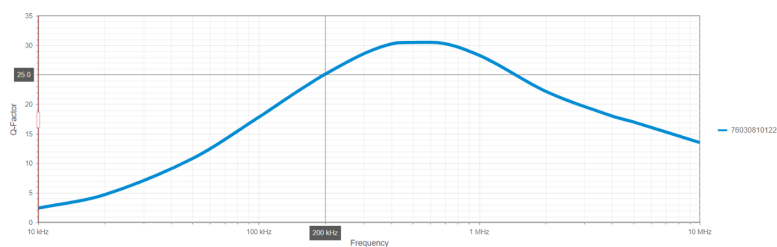


Figure 4.3: Quality factor of Rx coil.

The diode D1 rectifies the AC voltage at the ACIN pin. LTC4124 is capable of shunting excess received power to maintain the Vcc voltage in the desired range. Indeed, the functional block diagram 4.2 shows a comparator (CP1) connected at a switch used to control the input power. As shown in figure 4.4, the switch is closed when the voltage is higher than the battery voltage + 1.05 V and is open when the voltage is lower than the battery voltage + 0.85 V.

4.2 Pin-selectable charge current and voltage

It is only necessary to tie the pin ISEL 1/2 and VSEL 1/2 to Vcc or the ground in order to select the appropriate current and voltage to recharge a battery. As shown in table 4.1, you can select 4 charge currents and voltages for a total of 16 combinations.

4.3 NTC input to qualify temperature charging

The NTC pin is used to qualify the temperature of the IC during the recharge. LTC4124 manages temperature control by implementing the rising threshold (cold threshold) and the falling threshold (hot threshold). The cold threshold of CP5 is set at 75% of the Vcc voltage, while the hot threshold of CP6 is set at 35% of the Vcc voltage. If the NTC pin's voltage is outside this range, the recharge pauses, and

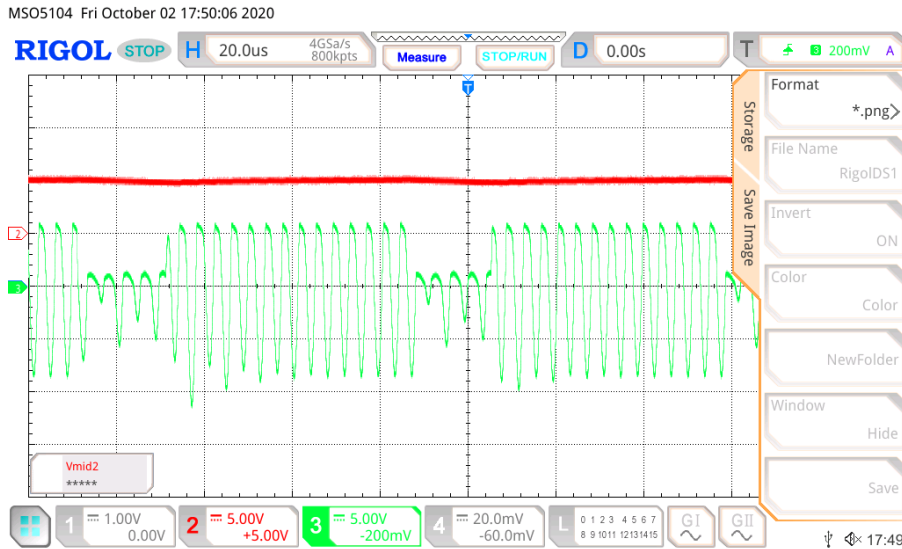


Figure 4.4: LTC4124 wireless power manager. Green signal is the AC voltage at ACIN pin. Red signal is the rectified voltage at pin Vcc.

VSEL1	VSEL2	Charge Voltage, V
HI	HI	4.35
HI	LO	4.20
LO	HI	4.10
LO	LO	4
ISEL1	ISEL2	Charge current, mA
HI	HI	100
HI	LO	50
LO	HI	25
LO	LO	10

Table 4.1: Charge current and voltage programming.

the current drops to zero. As shown in the electrical schematic 4.1, the thermistor employed is NTC432452, with a resistance of 10 k Ω at room temperature.

4.4 Li-Ion charger controller and UVCL

LTC4124 includes a constant current and constant voltage CC/CV linear battery charger with a safety timer termination, bad battery detection, and under-voltage current limiting (UVCL). The LTC4124 manages battery charging in constant current and constant voltage mode, which is typical charging for lithium batteries. As

shown in the figure, the voltage increases linearly in the CC mode, while the current is kept constant. When the voltage exceeds the recharge threshold (V_{BAT_RECHG}), typically 97.6% of the programmed charge voltage, the recharging enters the CV mode. Through CV mode, the voltage is kept constant, and the current gradually decreases. Also, the LTC4124 activates a timer to switch off charging after 3 hours. LTC4124 also allows to activate or deactivate the pre-charge mode (trickle charge). This mode is used at the start of recharging for the batteries that have been deeply discharged. Activating pre-charge mode delivers 10% of the programmed current until the battery voltage exceeds the threshold set at 68% of the programmed charge voltage (V_{BAT_TRKL}). If the battery has not exceeded the V_{BAT_TRKL} threshold after 40 minutes of charging, the CHRG pin indicates that the battery is faulty by blinking fast (6 Hz).

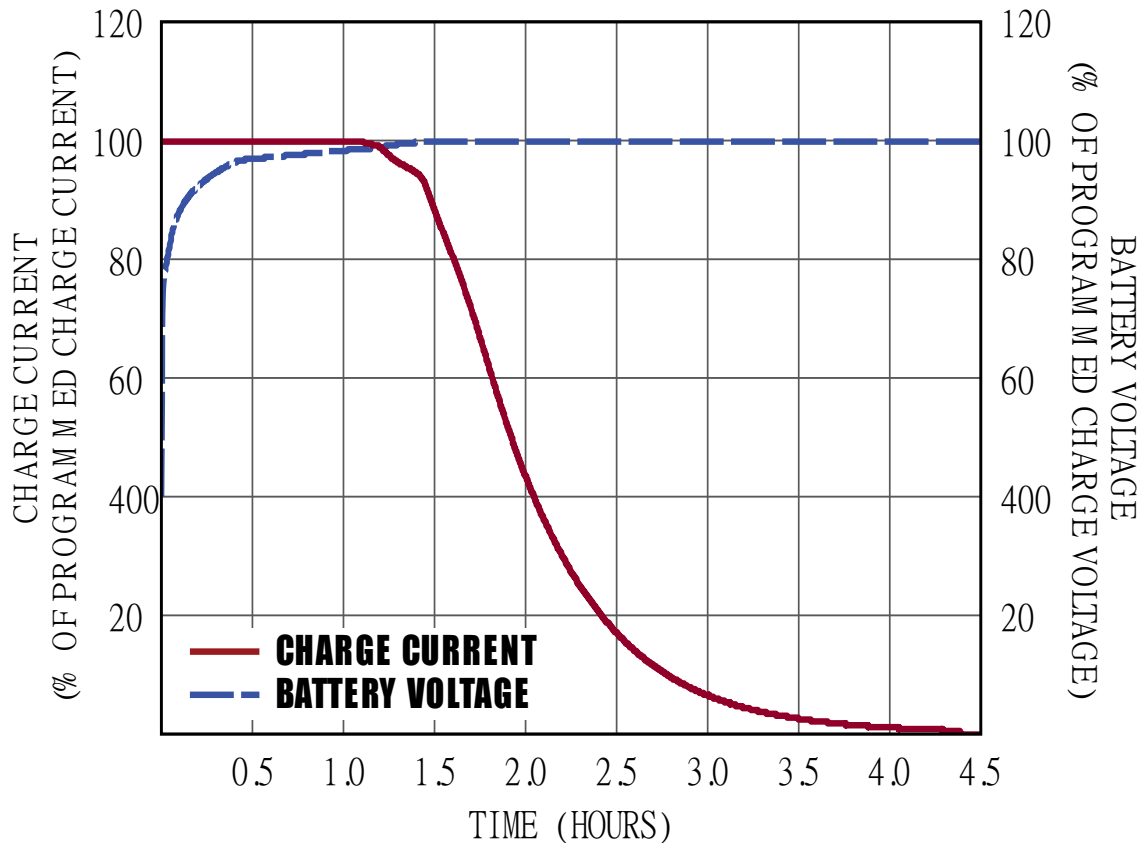


Figure 4.5: Example of battery recharge in CC/CV mode [41].

The LTC4124 implements under voltage current limiting (UVCL), which decreases the current delivered to the battery if the voltage on the V_{cc} pin is less than 3.4 V. This feature is particularly useful when the available power is limited. Without UVCL, the current would immediately drop to zero, allowing V_{cc} to exceed the

lower limit of functionality. This oscillatory behavior would result in intermittent charging. UVCL prevents this oscillatory behavior by adjusting the current depending on the related availability of power.

4.5 PowerPath Controller

The Ideal Diode Control block drive the gate of M2 to achieve a low voltage drop (50mV) from the BAT pin to the VCC pin. Current flows from the BAT pin to support the VCC pin voltage to be as close to that of the BAT pin as possible.

Chapter 5

NRIC power transmitter

The LTC4125 [43] is a complete AutoResonant wireless power transmitter, able to drive the series-resonant tank composed of transmit coil (L_{TX}) and the transmit capacitor (C_{TX}). LTC4125 has the advantage of being easily programmed by changing passive external components. Figure 5.1 shows the electrical schematic used for the transmitter.

The LTC4125 has two main features:

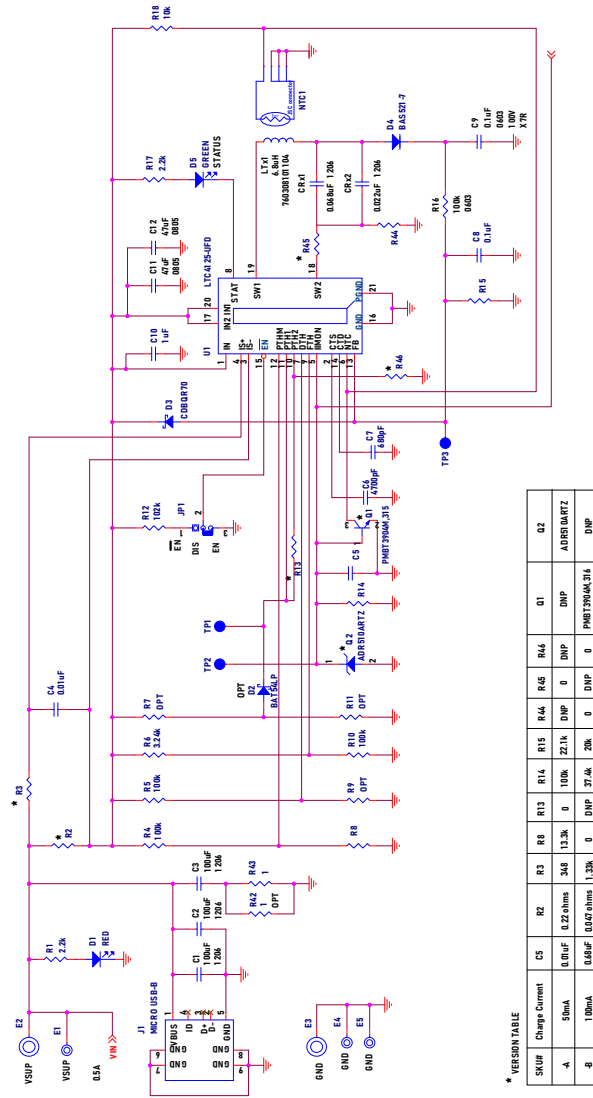
- AutoResonant Switching Frequency Adjusts;
- Optimum Power Search.

5.1 AutoResonant Switching Frequency Adjusts

LTC4125 employs a properly auto resonant technology. At the start-up, the IC drives the LC tank with a 50% duty cycle square wave at 2.5 kHz. LTC125 detects the flowing current in the LC tank and adjusts the frequency of the drive voltage accordingly. As shown in figure 5.2, the IC ensures that the voltage at each SW pin is always in phase with the current into the pin. With this technology, the LTC4125 continuously adjusts the driving frequency of the full-bridge switches to match the LC resonance frequency.

5.2 Optimum Power Search

In the wireless power system, the transmitter coil generates a magnetic field that must be sufficiently intense to transfer the power to the receiver. The efficiency of the power transmission changes according to the distance between the coil and the load variation. The LTC4125 enforces an Optimum Power Search algorithm that adjusts the strength of the magnetic field according to the condition of the



* VERSION TABLE

SKU#	Change	Current	C5	R2	R3	RE	R13	R14	R15	R44	R4d	Q1	Q2
A		50mA	0.01uF	0.22ohms	348	13.3k	0	100k	22.1k	DNP	0	DNP	ADR10ARTZ
B		100mA	0.01uF	10.0ohms	13.3k	0	DNP	27.0k	20k	0	DNP	0	PH1290M4L315
													DNP

Figure 5.1: LTC4125 electrical schematic, B version [42].

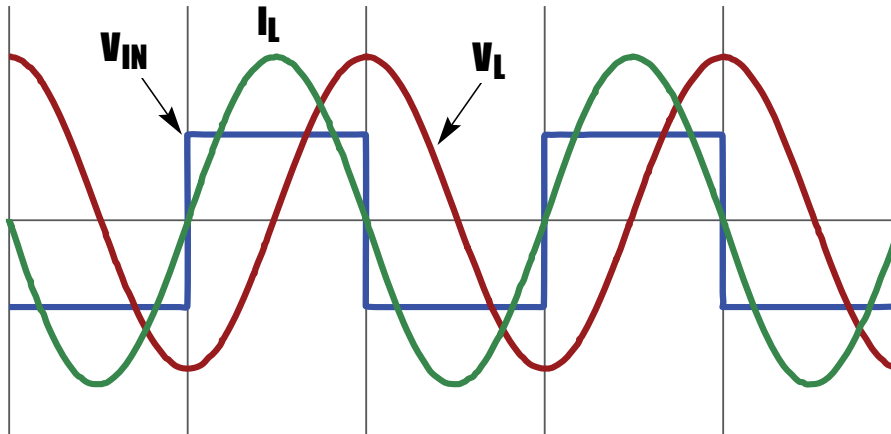


Figure 5.2: Voltage and current waveform (red and green) and input voltage control (blue) at frequency of LC tank [43].

transmission. The algorithm adjusts the pulse width of the full-bridge driver. The tank current and the tank voltage are proportional to the pulse width, therefore, to increase or decrease the magnetic field strength, it is sufficient to increase or decrease the pulse width.

Periodically, the optimum power search is effectuated and it is divided into three phases. The timing of each stage is programmable by changing capacitors connected at pin CTS and CTD.

- In the first phase (T1), the value of power transmission is retained at a constant starting value;
- In the second phase (T2), the optimum power search applies a stepwise linear ramp of transmit power to search the receiver. There are two possibilities: a positive or a negative search. When the positive search is met, phase T2 is stopped and the next phase starts. In the second phase, the receiver is identified by an increment in the power transmission amplitude, which means that the power required to meet the requirements of receiver load has been reached or exceeded. In the negative search, the stepwise linear ramp of transmitting continues until the upper limit is reached and afterward, the transmitted power drops to zero, and the next phase starts;
- In the third phase (T3), the power transmitted is held constant if the positive search is found.

The Optimum Power Search controls if any fault condition occurs. In case of a fault condition, the power transmission drops to zero until the next power search. The LTC4125 implements six fault conditions listed below:

- Foreign object, detected by frequency threshold programmed by the FTH pin;

- Coil temperature, detected via the NTC pin;
- Excessive tank voltage, detected by feedback (FB) pin;
- End of search ramp, when the pulse width reaches 50% of duty cycle;
- Input current limit, detected by IMON pin;
- Internal (die) over temperature.

To find a valid receiver, the LTC4125 implements two types of exit conditions during phase T2: primary and secondary. Primary exit conditions are not programmable, while secondary ones are programmable via hardware. There are two programmable secondary exit conditions:

- Input current threshold;
- Differential tank voltage threshold (DTH).

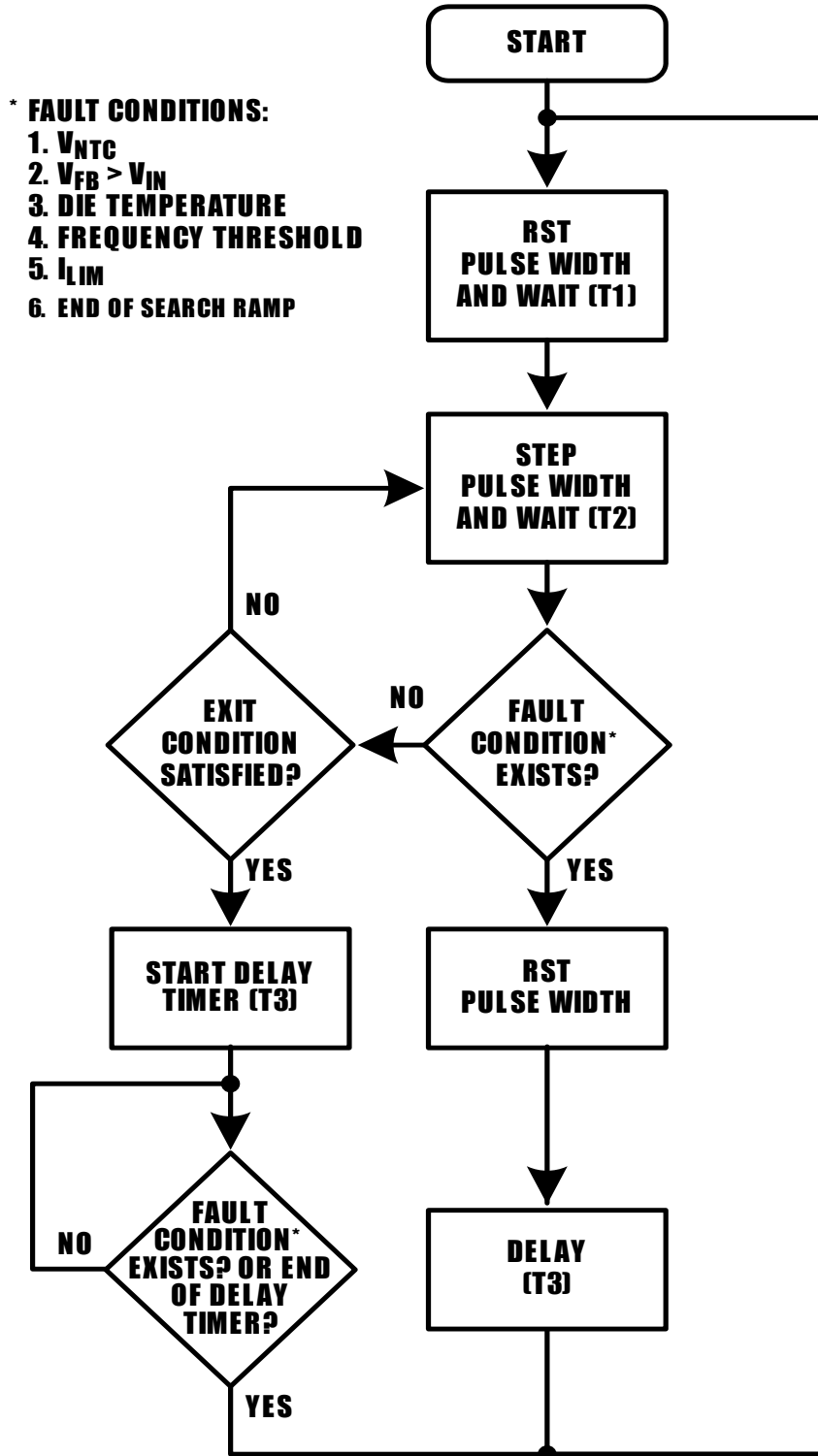


Figure 5.3: Optimum Power Search flow chart [43].

5.3 Operation

This section describes at how external passive components contribute to the operation of the transmission system and the programming of the Optimum Power Search. The block function diagram (fig. 5.4) shows a simplification of how the LTC4125 works. The external components shown in the block diagram are linked to the electrical schematic (fig. 5.1) via the summary table 5.1.

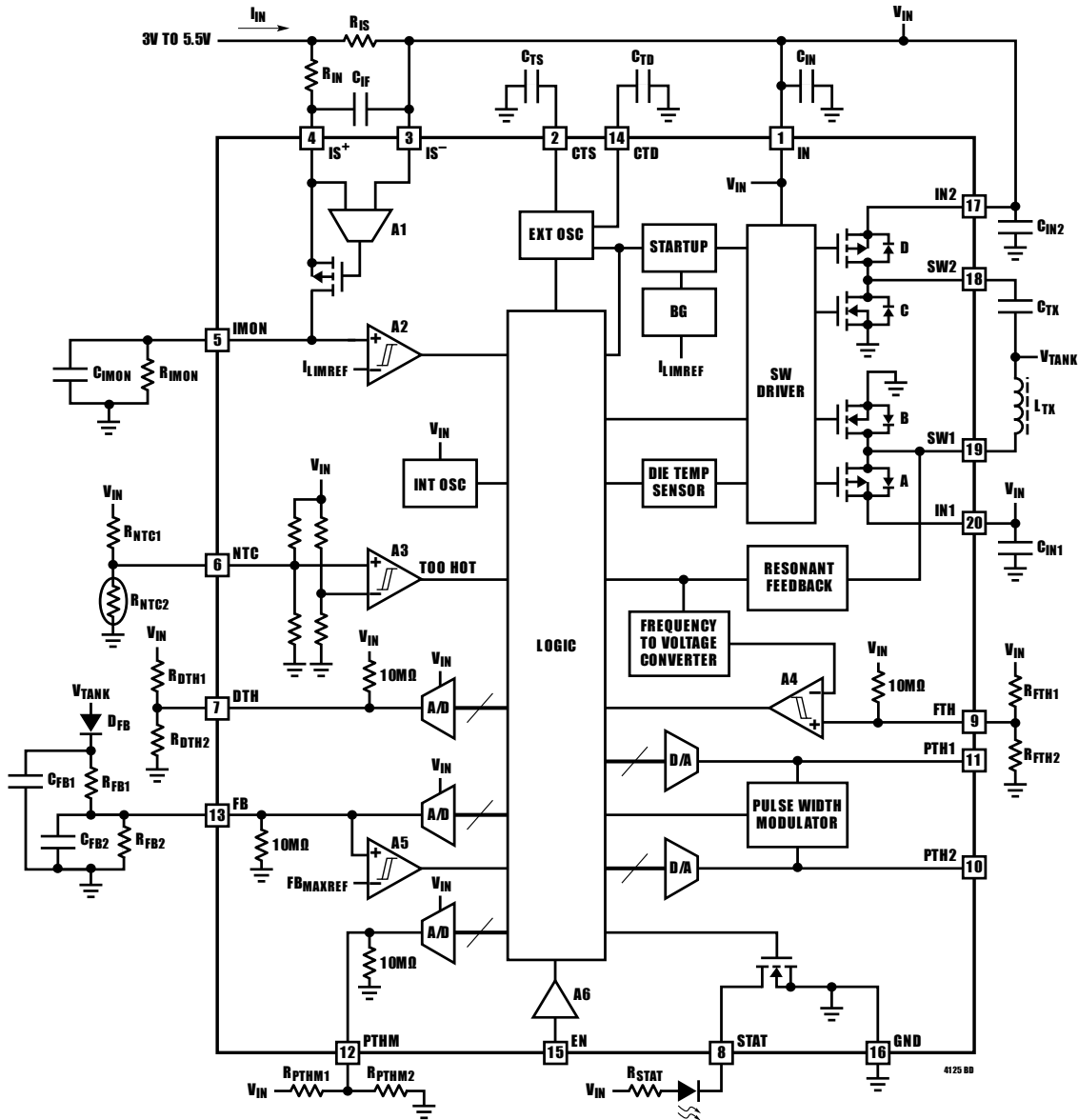


Figure 5.4: LTC4125 functional block diagram [43].

	Name	Notation	Value
Feedback	R_{FB1}	R16	100 k Ω
	R_{FB2}	R15	20 k Ω
Input current	R_{IN}	R3	1.33 k Ω
	R_{IMON}	R14	37.4 k Ω
	R_{IS}	R2	47 m Ω
Frequency threshold	R_{FTH1}	R6	3.24 k Ω
	R_{FTH1}	R10	100 k Ω
Timer capacitors	CTD	C7	0.68 nF
	CTS	C6	4.7 nF
Minimum Pulse Width	R_{PTHM1}	R4	100 k Ω
	R_{PTHM2}	R8	0 Ω
Delta threshold	R_{DTH1}	R5	100 k Ω
	R_{DTH2}	R9	Opt.
Temperature	R_{NTC}	-	10 k Ω
	R18	R18	10 k Ω
Transmitter resonant	L_{TX}	-	6.8 μ H
	C_{TX1}	-	68 nF
	C_{TX2}	-	22 nF

Table 5.1: Electrical components of transmitter circuit.

5.3.1 Wireless power transfer

LTC4125 manages the power transfer by using the half-bridge driver to modify the duty cycle of driver signal. In the electrical schematic (fig. 5.1) only SW1 is used to drive the LC tank. Therefore, better resolution of magnetic field intensity can be achieved during phase T2 but with lower maximum power transmission. This half-bridge driver drives the AC voltage and current to the same frequency as the LC tank. The LC tank consists of the coil and two parallel capacitors placed in series with the coil. The coil used is 760308101104 (Würth Electronic) and has an inductance of 6.8 μ H, a resistance of 125 m Ω , and a diameter of 20.8 mm. Two capacities in parallel (C_{Tx1} and C_{Tx2}) are used to obtain the same resonant frequency of the receiver (200 kHz). At this frequency, the quality factor of the Tx coil is 60.9, as shown in figure 5.5.

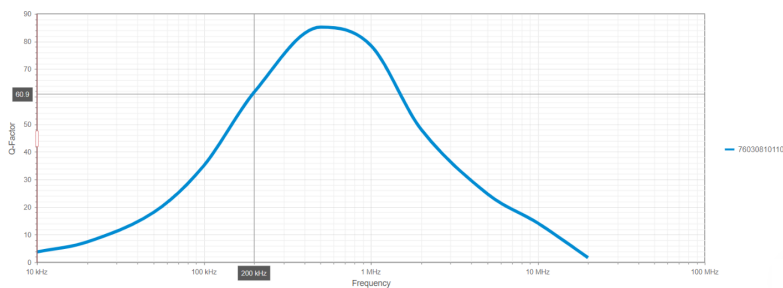


Figure 5.5: Quality factor of Tx coil.

5.3.2 Input current limit setting and monitoring

The LTC4125 monitors the current using three pins: IS-, IS+ and, IMON. The functional block diagram (fig. 5.4) shows the architecture employed by the IC. The sense resistance (R_{IS}) is used to monitor the input current. The voltage at the IMON pin varies with the current as follows:

$$V_{IMON} = \frac{R_{IMON} \cdot R_{IS} \cdot I_{RIS}}{R_{IN}} \quad (5.1)$$

The LTC4125 implements two input current parameters: input current threshold (I_{TH}) and input current limit (I_{LIM}). I_{TH} is one of two secondary conditions and when the current exceeds the threshold during the Optimum Power Search, the search is stopped and the power is held constant. I_{TH} is set according to the equation 5.2:

$$I_{TH} = \frac{R_{IN} \cdot V_{ITH}}{R_{IMON} \cdot R_{IS}} \quad (5.2)$$

where V_{ITH} is equal to 0.8 V. It is possible to simulate this secondary exit condition forcing the voltage over the threshold limit at the IMON pin.

I_{LIM} is the maximum current that can flow in the circuit. When the current exceeds the limit, power transmission is stopped immediately. The input limit is set according to the equation 5.3:

$$I_{LIM} = \frac{R_{IN} \cdot V_{LIM}}{R_{IMON} \cdot R_{IS}} \quad (5.3)$$

where V_{LIM} is equal to 1.25 V.

5.3.3 Frequency threshold

The frequency threshold pin is used to protect the LTC4125 against the foreign object. The LTC4125 employs an integrated frequency-to-voltage converter connected to the comparator A4 (fig. 5.4) to control the transmission frequency. The frequency to voltage converter is discretized to 7 bits with an input range between 0 and 320 kHz. Thus the accuracy of the frequency threshold input is limited to ± 2.5 kHz. The comparator compares the output of the frequency-to-voltage converter with the threshold programmed by the voltage divider between Vin and ground at the FTH pin. The following equation (5.4) determines the threshold value (F_{LIM}):

$$F_{LIM} = \frac{R_{FTH2}}{R_{FTH2} + R_{FTH1}} \cdot 320kHz \quad (5.4)$$

When a conductive object is interposed between the two coils, the apparent inductance decreases, and the resonant frequency increases. When the frequency exceeds the imposed limit, the LTC4125 detects a fault condition and reduces the transmitted power to zero until the next power search.

5.3.4 Timer capacitors

The capacitors connected to the CTS and CTD pins determine the period of a search cycle (fig. 5.6). The capacitor CTS determines the period T1 and T2 according to the equations 5.5 - 5.6:

$$T1 = \frac{256 \cdot C_{TS} \cdot 1.2V}{10\mu A} = 144ms \quad (5.5)$$

$$T2 = \frac{T1}{8} = 18ms \quad (5.6)$$

The capacitor CTD determines the period T3 according to the equation 5.7:

$$T3 = \frac{65 \cdot 10^3 \cdot C_{TD} \cdot 1.2V}{10\mu A} \cong 5s \quad (5.7)$$

where $10 \mu A$ is the typical pull-up current of pin CTS and pull-down current of pin CTD. The CTD pin must be short to the ground to disable Optimum Power Search. In this way, the LTC4125 will make a single cycle at power-up and then keep the power at the value found.

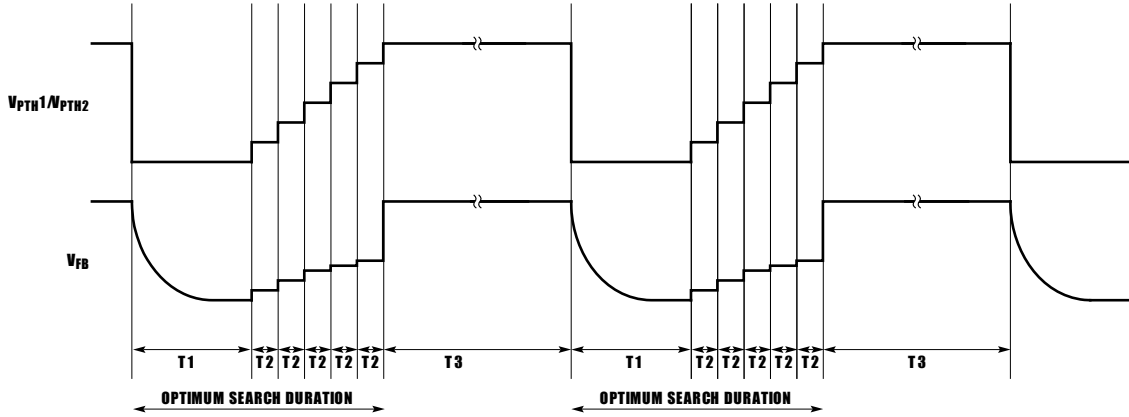


Figure 5.6: Timing diagram during Optimum Power Search [43].

5.3.5 PTH1/2

The pulse width regulates the amount of transmitted power, therefore, it is essential to have feedback about the pulse width size. The voltage on the pin PTH1 and PTH2 is proportional to the size of pulse width according to the equation 5.8:

$$PW_{SW_x} = \left(\frac{0.24}{fn} \cdot V_{PTH_x} \right) + 150ns \quad (5.8)$$

where f_n is the resonant frequency of the LC tank. During the Optimum Power Search, in phase T2, the pulse width increases as well as the voltage on the pin PTHx. In the electrical schematic (fig. 5.1) it is used only half of the full-bridge, so only PTH1 is available to monitor the power transmission.

5.3.6 Minimum pulse width

The initial power transmission in the phase T1 is defined by the voltage at the PTHM pin. The PTHM pin uses a voltage divider between the V_{IN} and ground and an integrated analog to digital converter to set the minimum pulse width according to the equation 5.9:

$$MINPW = \left(\frac{0.576}{f_n} \cdot \frac{R_{PTHM2}}{R_{PTHM2} + R_{PTHM1}} \right) + 150ns \quad (5.9)$$

In the electrical schematic (fig. 5.1) the PTHM is short to ground, in this way the pulse width is set at the minimum value of 150 ns.

The voltage on the PTHM pin is related to the voltage on the PTH pin by the equation 5.10:

$$V_{PTH} = \frac{V_{PTHM} \cdot 0.576}{V_{IN} \cdot 0.24} \quad (5.10)$$

The functionality of the PTHM pin was studied by changing the voltage on its pin and monitoring the voltage on the PTH pin with bench multimeter (Agilent 34411A). The test was carried out by varying the voltage on the PTHM pin by 50 mV from 0 V to 2 V. The result in figure 5.7 shows that the resolution of the integrated analog-digital converter in the PTHM pin is 5 bits.

5.3.7 NTC input to measure temperature

The Optimum Power Search monitors the temperature using NTC thermistor (MURATA, FTN55XH103FD4B). The NTC has a resistance of 10 k Ω at room temperature (25 °C) and a B factor equal to 3350 K . The NTC is located under the transmitted coil because it is the point that suffers the most heating. The coil is not a perfect inductor but has a parasitic resistance, which causes power dissipation thus resulting in the coil heating up. The NTC hot threshold (V_{NTCH}) is set to 35% of V_{in} , which is equal to 1.75 V. When the voltage on the NTC falls below 35% of the supply voltage, the fault condition is activated. Considering the resistance value of the thermistor at room temperature and the resistor R18, the fault temperature (T) can be determined using the following equations 5.11:

$$T = \frac{B}{\ln\left(\frac{R_{NTC}(T)}{R_{18}}\right) + \frac{B}{T_0}} \cong 42^\circ C \quad (5.11)$$

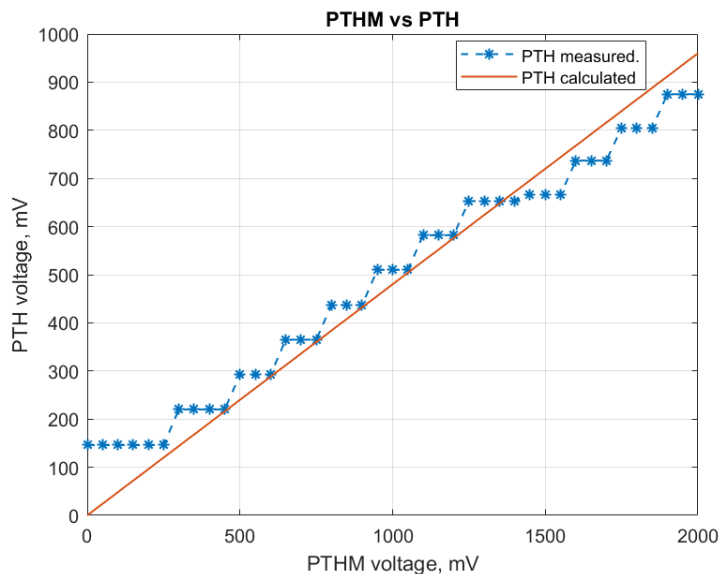


Figure 5.7: PTHM vs PTH voltage.

where T_0 is room temperature in kelvin (298 K). For safety reasons, the coil temperature cannot exceed 42 °C. If the temperature exceeds the limit, power transmission is interrupted until the coil temperature drops to a reasonable value.

5.3.8 Feedback

The Optimum Power Search monitors the LC tank voltage through the FB pin to ensure that the voltage does not exceed the limit. Also, the primary exit condition of Optimum Power Search uses the FB pin to determine if a receiver is found or not in phase T2 (fig. 5.8).

A half-wave rectifier, consisting of a diode and capacitors, is employed to detect the peak of LC tank voltage. The voltage at pin FB is given by a voltage divider. The ratio of the resistor divider is chosen according to the maximum voltage to be applied to the coil. It is possible to determine the maximum voltage on the coil through the following equation 5.12:

$$V_{TANK-MAX} < \left(\frac{R_{FB1}}{R_{FB2}} + 1 \right) \cdot V_{IN} + V_D \quad (5.12)$$

where V_D is the voltage drop of the rectification diode. If the voltage on the coil exceeds this limit $V_{TANK-MAX}$, the LTC4125 triggers a fault condition and stops delivering power until the next search.

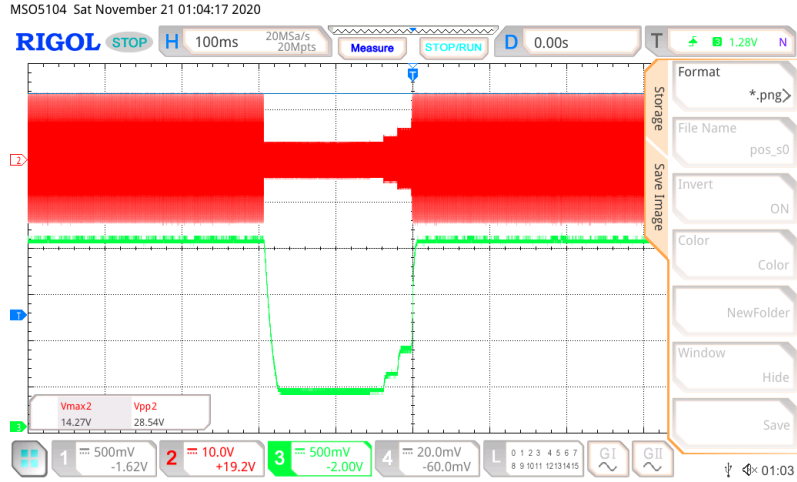


Figure 5.8: Positive search. FB voltage in green, Tx coil voltage in red.

5.3.9 DTH

The DTH pin can be used to activate one of the secondary exit conditions in the Optimum Power Search. During the sweep, if the feedback voltage (V_{FB}) is larger than V_{DTH} , the exit condition is satisfied, the sweep is stopped and the optimum power transfer is met. In a typical sweep, multiple primary exit conditions implemented by the LTC4125 detect the optimum power transfer. However, the DTH pin is useful when the receiver circuit has the lowest output power at the highest target separation (lowest coupling).

The DTH pin is programmed to set a threshold on the voltage step of the feedback signal. The optimum power is found when $\Delta V_{FB} > \Delta V_{DTH}$. The DTH pin is programmed with a resistor divider between V_{IN} and GND as follows (eq. 5.13):

$$V_{DTH} = \frac{R_{DTH2}}{R_{DTH1} + R_{DTH2}} V_{IN} \quad (5.13)$$

As shown in the electrical schematic (fig. 5.1), DTH is connected to V_{IN} to deactivate its function.

Chapter 6

Proof-of-concept open-loop NRIC system evaluation

The evaluation kit (DC2770AB) was used to test the NRIC link, and it consists of the transmitter and receiver previously described. The overall system design of the NRIC link is schematized in figure 6.1. The term “loop” refers to a real control loop that directly and actively involves the transmitter and receiver. The transmitter has its own control system but does not directly involve the receiver, thus the term “open-loop”.

Three main components define the overall efficiency of the system:

- The transmitter’s efficiency (η_T) to convert a DC voltage into an AC voltage to generate a strong magnetic field;
- The power transfer efficiency link (η_{PTE}), which depends on the quality factor and coupling coefficient of coils and the resonant frequency;
- The receiver’s efficiency (η_R) to rectify and regulate the AC voltage into a DC voltage to power supply an implanted device and recharge an implanted battery.

The product of these three efficiencies gives the overall efficiency (η_{TOT}), and it is the most relevant parameter to consider. A high-efficiency NRIC system results in less intense magnetic fields, less overheating, and less power dissipation. Therefore, it is essential to test the overall efficiency of the NRIC system.

6.1 Test bench

A test bench was set up to test the overall efficiency of the NRIC link when charging a battery. A battery emulator was used to simulate the behavior of batteries.

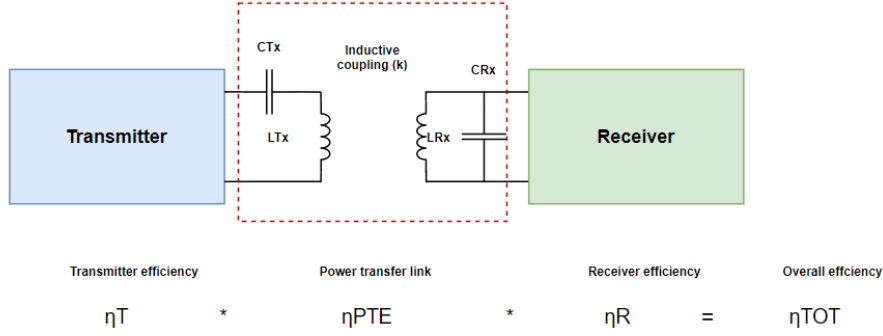


Figure 6.1: Overall efficiency of NRIC system.

As indicated in the datasheet, a $20\ \Omega$ resistor was connected between the receiver pins BAT and GND. The DC power supply (RIGOL DP832) was connected to the resistor in parallel to simulate the battery voltage.

The overall efficiency of the NRIC link was measured as the ratio between transmitter input power and receiver output power. In this way, all three efficiencies are taken into account. The PTE parameter limits the overall efficiency. Indeed, the power transfer between two coils is particularly affected by the coupling coefficient k , which has values less than 0.5 when air or skin is interposed between them. The value of the coupling coefficient is given by the following equation (6.1):

$$k = \frac{M}{\sqrt{L1 \cdot L2}} \quad (6.1)$$

M is the mutual inductance between coils, while $L1$ and $L2$ are the Tx and Rx coil's inductances. The mutual inductance of the coil depends on its geometry disposition, and its value decreases with the increase of the coil distance and with lateral and angular misalignments. Furthermore, PTE is optimized for one specific load; however, implantable medical devices are subject to load variation.

Taking into consideration all these aspects, tests were carried out to quantify the overall efficiency of the NRIC system and were initially performed as follow:

- Perfect alignment between coils with interposed air;
- Distance between coils from 3 mm to 20 mm;
- Load:
 - Simulated battery charging voltage from 2.8 V to 4.1 V;
 - Charging current of 10, 25, 50 and 100 mA.

6.2 Experimental results

The overall efficiency of the NRIC system for four different charging currents is shown in four figures 6.2, 6.3, 6.4 and 6.5. Each figure shows the related efficiency with the variation of the coil's distance and simulated battery voltage. As it can be seen from the figures and was presumed from the theory, the efficiency tends to decrease as the distance between the coils increases because the magnetic field strength and the coupling coefficient between the coils decrease. On the other hand, the overall efficiency increases as the current supplied by the receiver (load) increase. Indeed, for 10 mA charging (fig. 6.2) the maximum efficiency is 20.7%, for 25 mA charging (fig. 6.3) it is 30.5%, for 50 mA charging (fig. 6.4) it is 35.1% and for 100 mA charging (fig. 6.5) it is 40%. The power transfer of the NRIC system is more efficient for 100 mA charging current but only for distances less than 5 mm. It can be seen that the power transfer drops to zero very quickly for 50 and 100 mA charging currents. The NRIC system is unsuitable for transferring large powers (>0.2 W) at distances greater than a few mm. For 10 and 25 mA charging currents, the transfer is less efficient, but it also suitable for distances greater than a few mm.

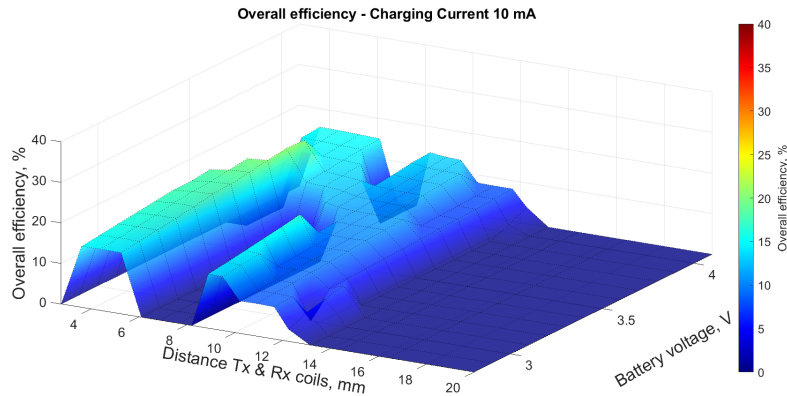


Figure 6.2: Overall efficiency of NRIC system, charging current 10 mA.

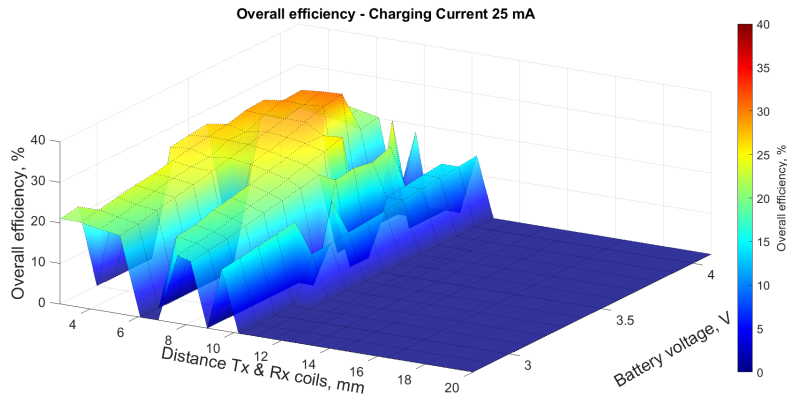


Figure 6.3: Overall efficiency of NRIC system, charging current 25 mA.

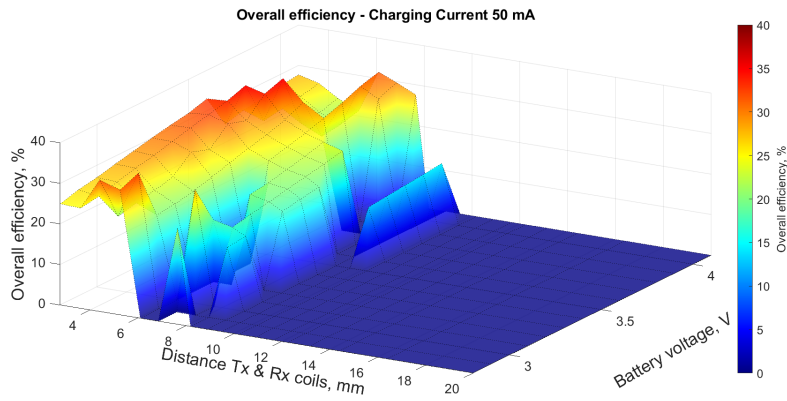


Figure 6.4: Overall efficiency of NRIC system, charging current 50 mA.

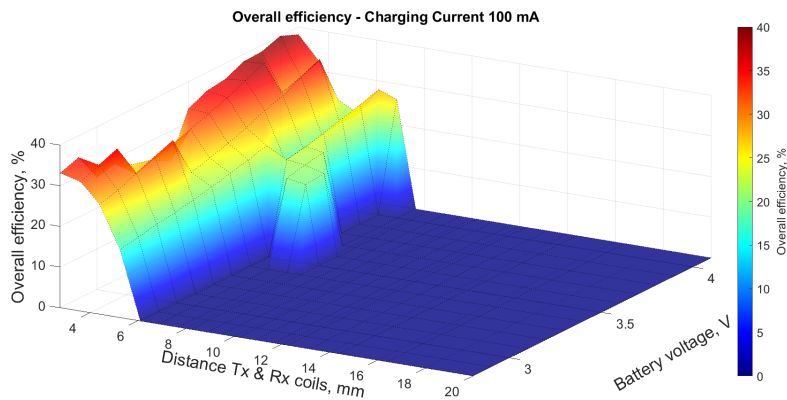


Figure 6.5: Overall efficiency of NRIC system, charging current 100 mA.

6.2.1 Wireless power transfer issues

The overall efficiency drops to zero when the transmitter stops supplying power. As already stated, there are six fault conditions causing power transmission to stop. The analysis showed that two different fault conditions are activated:

- FB threshold over 5 V;
- NTC Threshold.

The first fault condition arises in phase T2 of Optimum Power Search. When the transmitter is not able to find a receiver, the power transmission drops to zero. Figure 6.6a shows the voltage on the FB pin (green) and the voltage of the coil TX (red). Both voltages increase gradually, but the small voltage increase of the FB signal between two steps is not sufficient to recognize the presence of the receiver. Therefore, the power transmission drops to zero. As shown in figure 6.6b, the PTH voltage (green) drops to zero when the FB condition occurs, and the duty cycle of the driver signal (red) decreases along with PTH voltage.

The second fault condition, instead, concerns the temperature of the transmit-

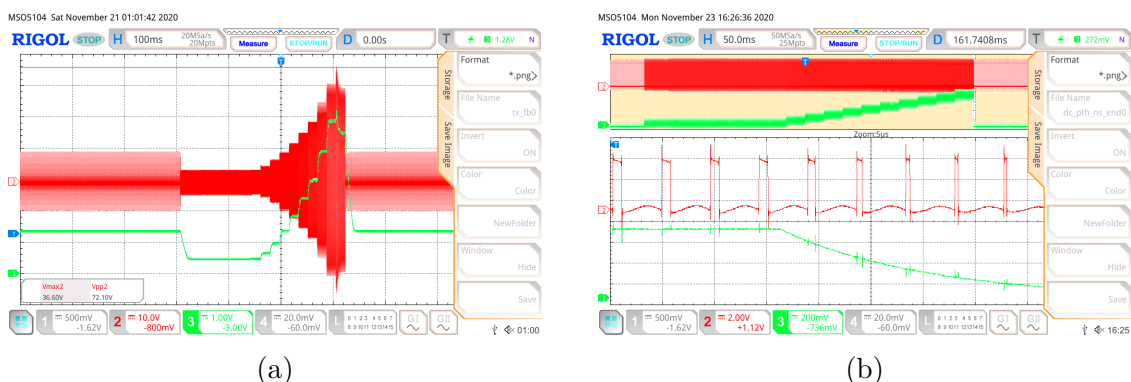


Figure 6.6: Feedback fault condition. a) FB voltage (red) and Tx coil voltage coil (green). b) PTH voltage (green) and driver signal (red).

ter coil. The transmitter must generate a high-intensity magnetic field when the receiver is programmed to deliver 50 mA and 100 mA. Therefore, the transmitter requires a high current that causes overheating of the coil. In this case, the Optimum Power Search finds the receiver, but the optimum power found causes an unacceptable overheating. The Tx coil and IC receiver temperature were monitored with a thermal imaging camera (fluke Ti10). The temperature of the Tx coil exceeds the threshold imposed of 42 °C when the distance of the coil is greater than 6 mm. Figure 6.7 shows that the temperature of the IC receiver, when programmed to deliver 100 mA, reaches at 40 °C, which is unacceptable for implanted devices.

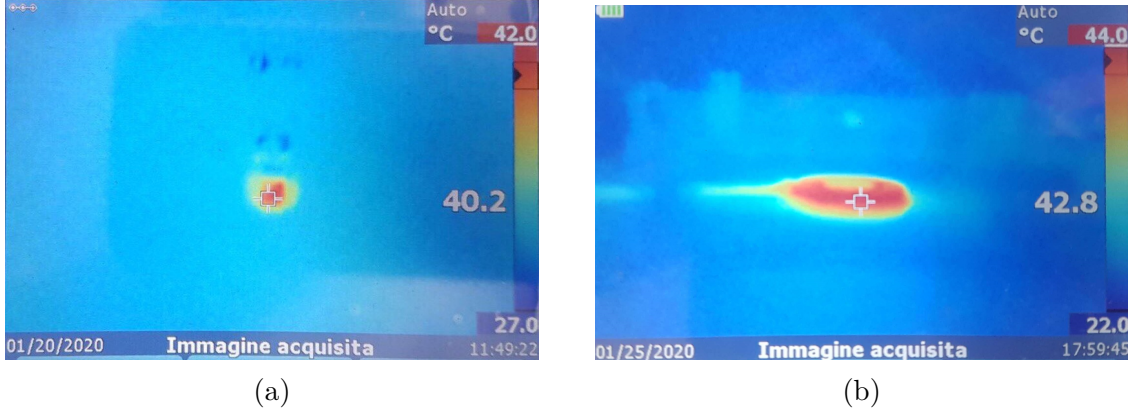


Figure 6.7: Overheating of IC receiver and Tx coil. Charging current of 100 mA and coils distance of 6 mm.

6.3 Battery charging tests

From the analysis carried out concerning the overall efficiency, 10 and 25 mA charging currents are the most promising and the most suitable ones. The choice of batteries to be tested was based on the characteristics of the battery already used for the nanofluidic implantable platform. The primary battery (CR2016, VARTA) has a capacity of 90 mAh, a diameter of 20 mm, a height of 1.6 mm, and a nominal voltage of 3 V. Therefore, the following three parameters were considered:

- Battery size;
- Capacity;
- Charge voltage and current.

The characteristics of the selected batteries (LIR2016/2025/2032) are shown in the table 6.1.

Batteries	Diameter, mm	High, mm	Nominal voltage, V	Capacity, mAh	Maximum charging current, mA
CR2016	20	1.6	3	90	-
LIR2016	20	1.6	3.7	16	16
LIR2025	20	2.5	3.7	25	25
LIR2032	20	3.2	3.7	40	40

Table 6.1: Comparison of primary versus secondary battery characteristics.

The primary battery can power the nanofluidic drug delivery system for about 20 days at maximum consumption conditions. The secondary batteries chosen have a lower capacity and allow the system to be powered for less time. The discharge time for the LIR2016/25/32 batteries would be 3, 5, and 8 days respectively. The

main advantage of the secondary batteries is that they can be recharged. According to the datasheet, the batteries can be recharged 500 times if they are recharged with the nominal current. By implementing these batteries, the device would operate for more than 4, 6, and 10 years respectively.

The recharging test was carried out to check whether any fault conditions occurred during the recharging process that could compromise correct recharging. According to the overall efficiency tests, the best distance to use between the coils is 5 mm for charging currents of 10 mA and 25 mA. Figure 6.8 shows the battery recharges. The current was acquired with the bench multimeter (Agilent, 34411A) and the voltage with the Atmega328p microcontroller (Microchip). For the LIR2016 and LIR2025 batteries, the 10 mA recharge current was used (fig. 6.8a and 6.8b), while for the LIR2032 battery, the 25 mA recharge current was used (fig. 6.8c). In all recharges, fault conditions were highlighted. Fault conditions are caused by a failure to search the receiver. Therefore, the voltage at pin FB increases until it exceeds the set threshold. The charging current drops to zero during a fault condition because the power transmission is interrupted.

This analysis has shown that the system used in this way is inefficient for recharging batteries. The system does not guarantee continuous power transmission. Also, only a coil spacing of 5 mm could be tested, larger distances do not allow any charging.

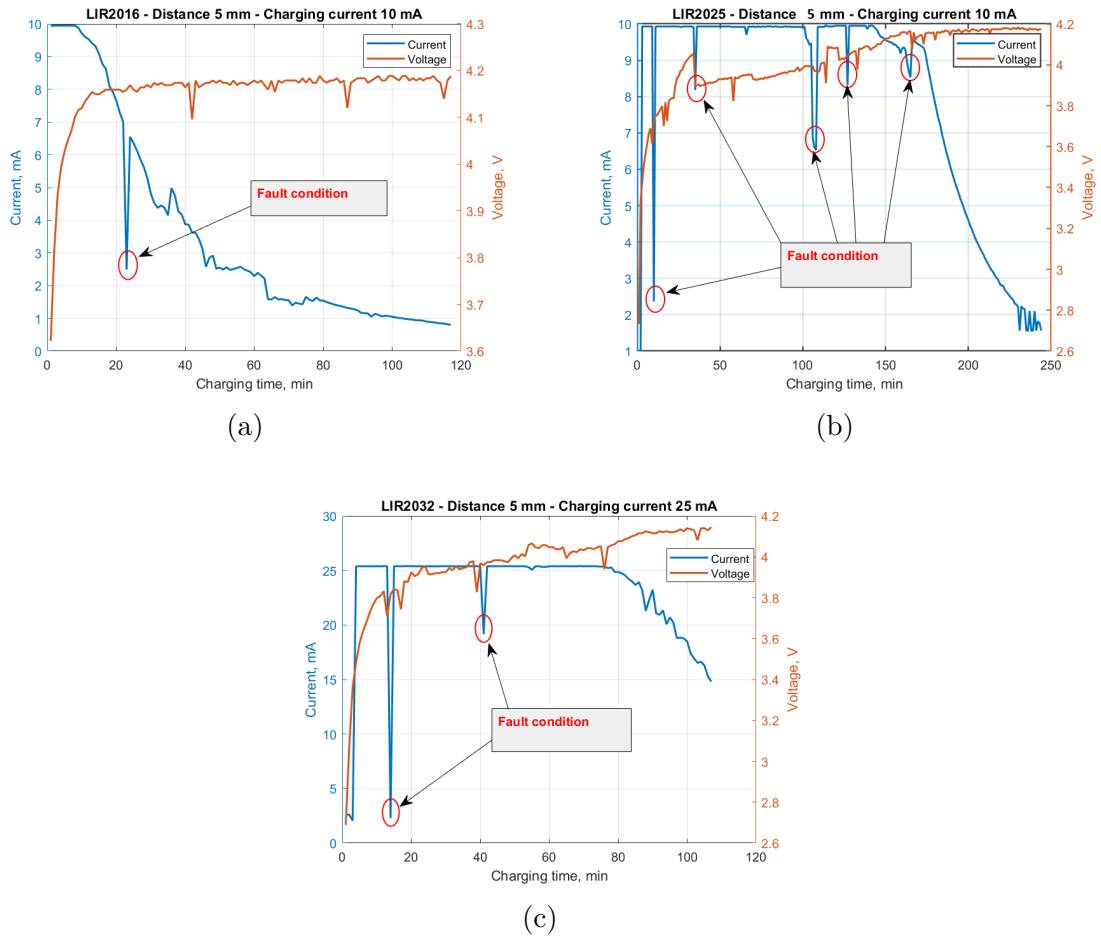


Figure 6.8: Battery recharging test, coils distance of 5 mm. a) LIR2016 charging current 10 mA. b) LIR2025 charging current 10 mA. c) LIR2032 charging current 25 mA.

Chapter 7

Closed-Loop NRIC system

The problems of the NRIC link are related to the transmitter. Indeed the power drops to zero when the receiver is not found. The main problem is the accuracy of the primary exit condition of the transmitter. Indeed, the Optimum Power Search is not able to find a receiver due to a small voltage increase of FB signal during phase T2.

There are two possible ways to solve this problem:

- DTH secondary exit condition;
- Closed-loop system.

Using the DTH pin is possible to set a secondary exit condition. A threshold is set on the step size of the voltage on the FB pin. This solution can be used when the NRIC link is at the lowest coupling condition; however, it is not the best solution. If the condition of transmission changes, a fixed threshold could result in insufficient transmission power. Especially for an implantable system, it is necessary to have a system that can adapt to different configurations.

The closed-loop system would allow power transmission to be managed according to the receiver's requirements without the problems due to the step size of the FB pin. The use of the FB pin allowed a feedback between the receiver and the transmitter. However, it was deficient when transmission conditions varied. Using a closed-loop system that bypasses the FB pin would improve the communication efficiency between the receiver and transmitter. This solution is the most suitable as it involves changing the voltage on the PTH pin to modify the transmitted power according to the receiver's requirements. A hardware and firmware communication system was added to the NRIC link to do that.

7.1 Hardware design

The transmission problem is identified in phase T2 of Optimum Power Search, where the primary exit conditions cannot identify the receiver. The electrical schematic of the transmitter was changed to modify the Optimum Power Search, and we developed a feedback system to control the power transmission was developed.

7.1.1 Optimum Power Search improvements

It is sufficient to modify the external components of the transmitter circuit to change the Optimum Power Search. The transmitter has been modified in two parts:

- Modification at IMON pin;
- Modification at PTHM pin.

The electrical schematic at the IMON pin has been modified to activate the secondary exit condition during the phase T2. Adding a voltage divider composed by $R14 = 100\text{ k}\Omega$ and $R15 = 75\text{ k}\Omega$ (fig. 7.4a) between the V_{IN} and ground ensures the voltage at the IMON pin to be 1 V . In this way, when the transmitter reaches phase T2, the search step is stopped immediately. Transistor Q1 is removed to avoid that NTC voltage drops to zero when the 1 Volt is applied.

The resistor divider on the PTHM pin was modified to change the initial value on the PTH pin in phase T1. Therefore, the initial value of the PTH pin is not set to the minimum but is equal to the value set by the voltage divider, according to the equation 5.10. The voltage divider at the PTHM pin comprises $R4 = 100\text{ k}\Omega$ and $R8 = 20\text{ k}\Omega$ to have a voltage of 800 mV . Therefore the voltage on the PTH pin is equal to 360 mV in phase T1. The modification of the Optimum Power Search is shown in figure 7.1. Figure 7.1a shows a positive power search before the modification, while Figure 7.1b shows the positive search after modification, where the phase T2 is not present. After phase T1, the PTH pin shows only one step of 75 mV before starting phase T3.

7.1.2 Explicit power control

The PTH pin is useful to monitor the duty cycle on the SW pin and can be driven as an input to set the duty cycle [44]. An external pull-down resistor in series with a MOSFET can discharge a capacitor connected to the PTH pin. In this way, it is possible to control the voltage on the PTH pin and the power transmission simply by opening and closing the MOSFET with a control signal.

It was necessary to evaluate the internal pull-up resistance, to select the pull-down resistor and capacitor values. The value of pull-up resistance was obtained by

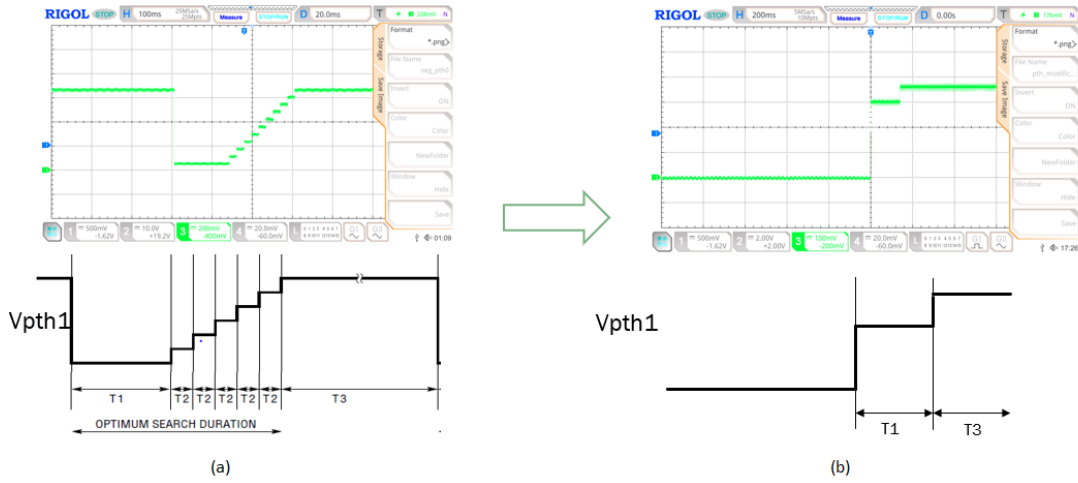


Figure 7.1: Modification of Optimum Power Search. a) PTH voltage before modification. b) PTH voltage after IMON and PTHM modifications.

measuring the time constant of the voltage across the capacitor connected to the PTH pin. Those measures were performed with the oscilloscope (RIGOL MS05104). The test was conducted following this procedure:

- Capacitance values: $1 \mu\text{F}$, $0.47 \mu\text{F}$, $0.22 \mu\text{F}$ and 68 nF ;
- The voltage at the PTH pin from 100 mV to 700 mV .

The result in figure 7.2 shows that the value of the pull-up resistance of the PTH pin is about equal to $180 \text{ k}\Omega$. A capacitor of $1 \mu\text{F}$ was chosen to have a charge time constant of approximately 200 ms . The value of the pull-down resistor was chosen to be $10 \text{ k}\Omega$. Therefore, the time constant during discharge is faster than during charging. The discharge time constant is 10 ms , guaranteeing a ratio between the charge and discharge time constant of 20. The N-MOSFET (TN0702) in series with the resistor is used to discharge the capacitor and control power transmission.

The feedback circuit consisting of a comparator (TLV7011) and a DAC (dac7563) was used to control the opening and closing of the MOSFET. The comparator compares the voltage of the capacitor with the threshold imposed by the DAC. When the voltage of the capacitor exceeds the high threshold, the output of the comparator is put high. This signal drives the gate of the MOSFET into saturation, thus allowing the capacitor to be discharged. When the voltage of the capacitor is below the low threshold, the output of comparators drops to zero. In this way, the MOSFET goes into interdiction, thus allowing the capacitor to be charged. Therefore, the PTH voltage fluctuates around the threshold set by the DAC.

The fluctuation of PTH voltage must be kept under control to have a correct transmission of power. A different comparator (Imp7300) was initially used to

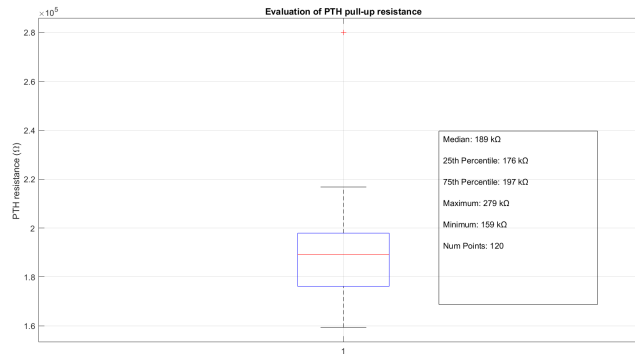


Figure 7.2: Evaluation of PTH pull-up resistance.

figure out the best hysteresis value to employ. Figure 7.3a reports the electrical circuit to test the best hysteresis value. The comparator lmp7300 is characterized by adjustable positive and negative hysteresis. The value of the hysteresis depends on the voltage on the resistance R4 and the positive and negative hysteresis is set to be the same. Thanks to the DAC, it is possible to variate the value of hysteresis. The test was performed for five different hystereses: ± 100 mV, ± 50 mV, ± 25 mV, ± 10 mV and ± 5 mV:

- Figure 7.3b reports the test with hysteresis of 100 mV. The red signal is the Vcc voltage of the receiver. The test shows that with a hysteresis of 100 mV at the PTH pin, the voltage on the receiver (Vcc) is unstable with a peak-to-peak voltage (V_{pp}) greater than 1 V.
- Figure 7.3c reports the test with hysteresis of 50 mV. The red signal is the Vcc voltage of the receiver. The test shows that with a hysteresis of 50 mV at the PTH pin, the voltage on the receiver (Vcc) is unstable with a peak-to-peak voltage (V_{pp}) greater than 1 V.
- Figure 7.3d reports the test with hysteresis of 25 mV. The red signal is the Vcc voltage of the receiver. The test shows that with a hysteresis of 25 mV at the PTH pin, the voltage on the receiver (Vcc) is unstable with a peak-to-peak voltage (V_{pp}) greater than 900 mV.
- Figure 7.3e reports the test with hysteresis of 10 mV. The red signal is the Vcc voltage of the receiver. The test shows that with a hysteresis of 10 mV at the PTH pin, the voltage on the receiver (Vcc) is quite stable with a peak-to-peak voltage (V_{pp}) greater than 400 mV.
- Figure 7.3f reports the test with hysteresis of 5 mV. The red signal is the Vcc voltage of the receiver. The test shows that with a hysteresis of 5 mV at

the PTH pin, the voltage on the receiver (V_{cc}) is stable with a peak-to-peak voltage (V_{pp}) greater than 170 mV.

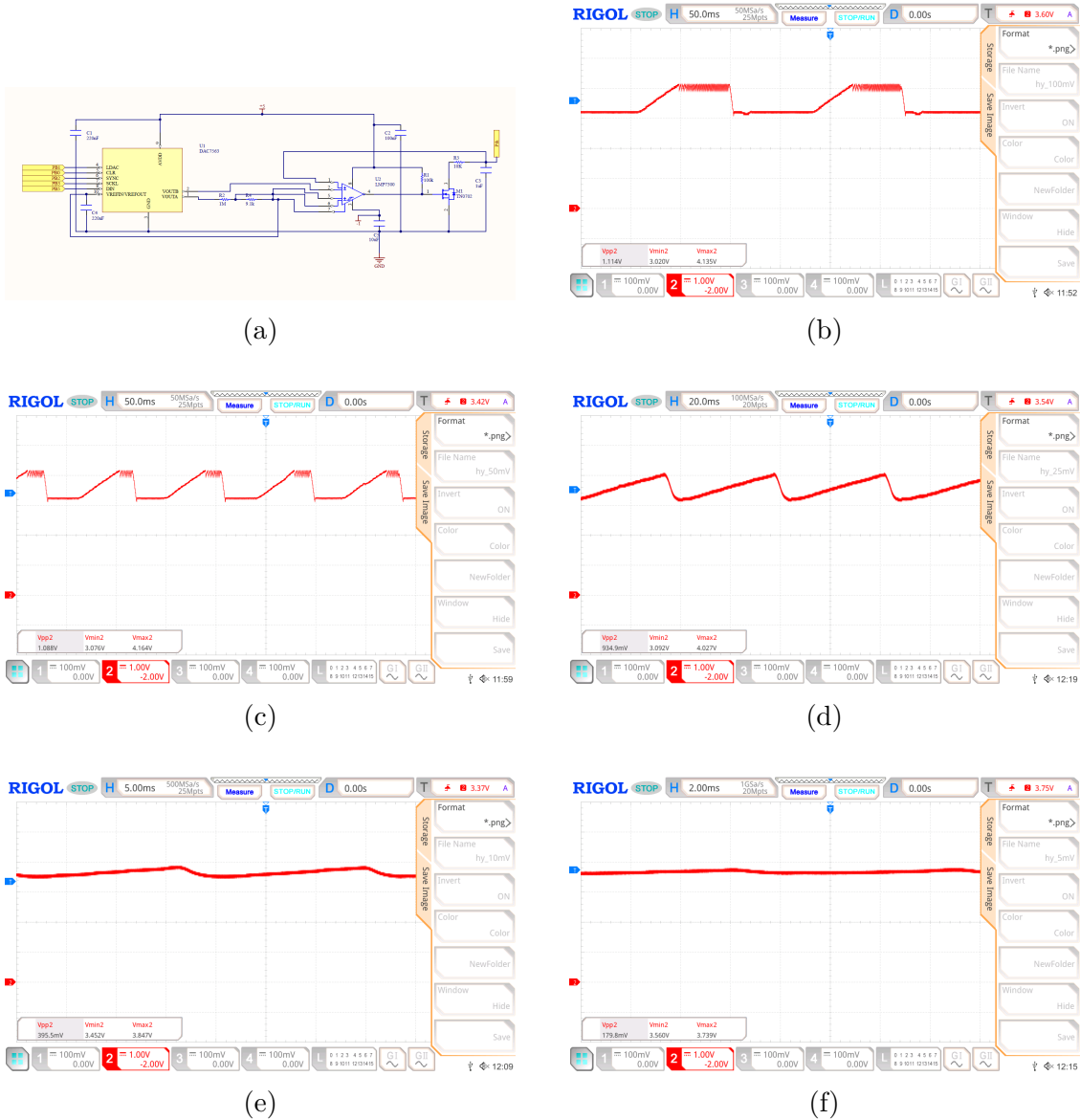


Figure 7.3: a) Electrical schematic for studying how the hysteresis of the comparator (LMP7300) affects the V_{cc} voltage at the receiver. b) Hysteresis at ± 100 mV. c) Hysteresis at ± 50 mV. d) Hysteresis at ± 25 mV. e) Hysteresis at ± 10 mV. f) Hysteresis at ± 5 mV.

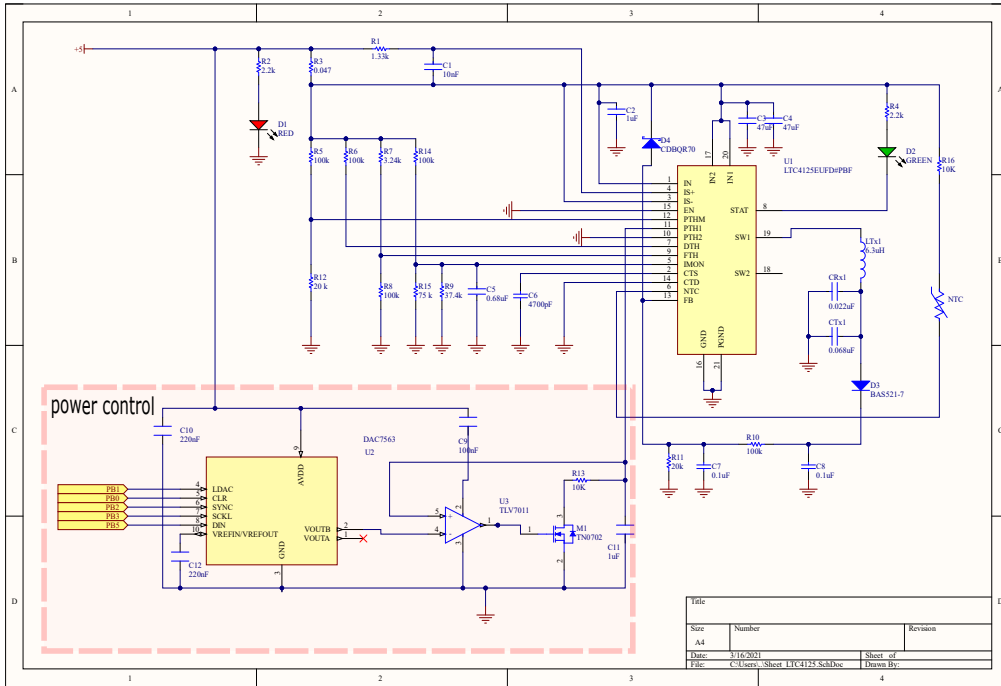
Hysteresis ± 5 mV is the most suitable to allow constant power transmission. The comparator (lmp7300) used for the hysteresis test is not suitable for the final implementation. Indeed the IN + and IN - have a common-mode voltage range

from 1 V above the negative rail to the positive rail, while the PTH pin voltage is in the range of 0 to 1 V. Therefore, a dual power supply (fig. 7.3a) was used from -1 V to 5 V.

The latest version of the transmitter's electrical schematic is shown in figure 7.4a where the comparator lmp7300 has been replaced by the comparator TLV7011. The comparator used (TLV7011) is characterized by the rail-to-rail common-mode input voltage and internal hysteresis of ± 4 mV. The operation of the implemented power control system is shown in figure 7.4b where the capacitor voltage (PTH signal) is shown in green and comparator output is shown in red. When the voltage on the capacitor exceeds the high threshold, the capacitor is discharged until the voltage value exceeds the low threshold. The threshold set by the DAC defines the voltage value of the capacitor. With the power control system, it is possible to manage the power transmission by simply varying the threshold value, thus changing the voltage on the capacitor (PTH signal) and consequently the power transmitted.

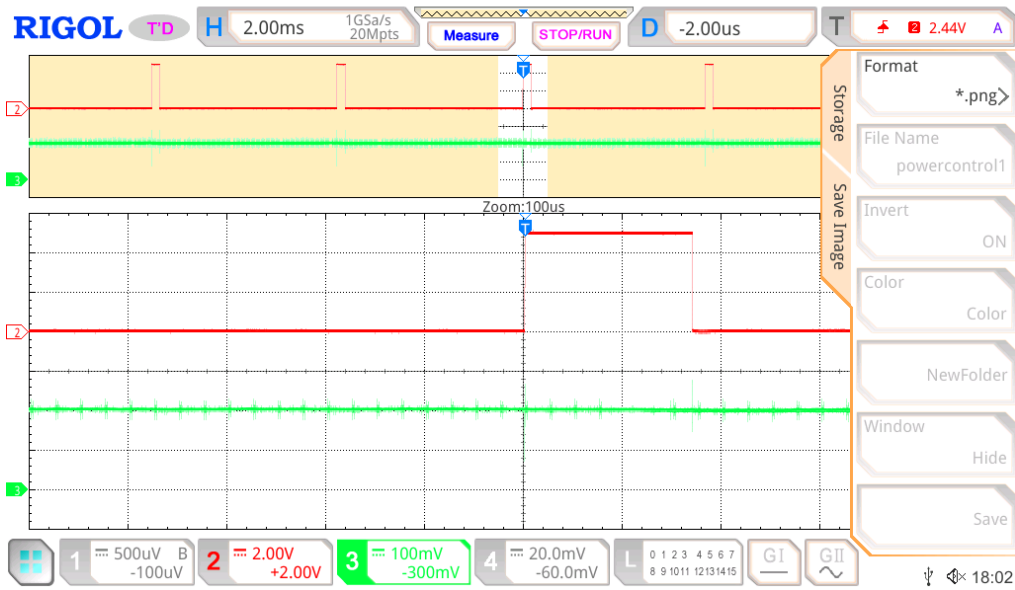
Aspects relating to the DAC and its programming are covered in the firmware section.

Closed-Loop NRIC system



(a)

MSO5104 Thu February 11 18:02:48 2021



(b)

Figure 7.4: a) Electrical schematic of transmitter with power control. b) Comparator output signal (red) and the voltage of PTH (green).

7.2 Embedded control loop implementation

The microcontroller Atmega328p was used to develop the closed-loop system. The microcontroller has two main tasks: checking the power at the receiver and controlling the DAC output. Figure 7.6 reports the firmware flow chart to control the power transmission.

For the receiver part, the microcontroller monitors the V_{cc} voltage and the battery voltage every four seconds. The V_{cc} voltage must exceed the threshold of 3.6 V and must be higher than the battery voltage to have proper power transmission. The first check is on the V_{cc} voltage: if the voltage does not exceed the threshold set at 3.6 V, the power is increased. The second check starts on the voltage difference between V_{cc} and the battery voltage only if the first condition is verified. It has been set that the voltage on the V_{cc} pin lies in a range between 300 mV and 700 mV above the battery voltage. The lower threshold has been selected to guarantee the correct operation of the receiver and to provide a stable charging current. The upper threshold was selected for two reasons:

- The internal switch of receiver power control is never activated, avoiding power dissipation. Indeed, the V_{cc} voltage never exceeds the internal threshold of $1.2 V + V_{bat}$;
- If the transmitted power is too high, the feedback system adjusts the power transmission. This function is particularly useful during the last charging phase when less current is required, and therefore less power must be transmitted.

With these controls, it is possible to manage power transmission as efficiently as possible, avoiding overheating due to excessive magnetic fields intensity.

The microcontroller uses the serial peripheral interface (SPI) to program the DAC. The DAC is characterized by 12-bit digital-to-analog converters and has been programmed to have the following characteristics:

- Internal reference of 2.5 V;
- Output gain: 2;
- Resolution of 1.22 mV.

The DAC output sets the threshold of the comparator and therefore the voltage value of the PTH pin. The threshold step of 2.5 mV is used to change the PTH voltage. Figure 7.5 shows the study of how the variation of the PTH voltage affects the duty cycle of the driver signal at the SW1 pin (blue) and the power required from the transmitter (red). The test was carried out by changing the PTH voltage with the chosen step of 2.5 mV from 180 mV to 260 mV. The duty cycle was studied using

the RIGOL MSO5104 oscilloscope by taking 100 measurements for each acquisition. In the open-loop system discussed in chapter 6, the variation of PTH was 75 mV. Whereas with the closed-loop system the variation of PTH has been set to 2.5 mV and the results show that with this variation it is possible to vary the duty cycle of the driver signal more finely and to better manage the power required by the transmitter during transmission. Therefore, these changes allow better efficiency of the transmitted power.

The microcontroller is also used to store the main data. Every second, the battery voltage and charging current are acquired and saved. While the threshold is saved every time it changes, the Tx coil temperature is acquired every 30 minutes.

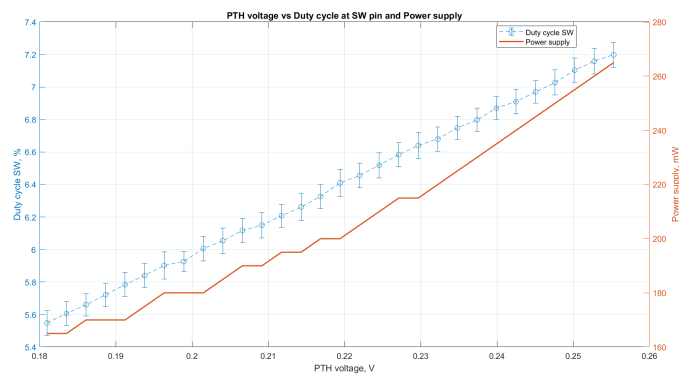


Figure 7.5: Duty cycle of driver signal at SW pin and power supply compared to PTH voltage.

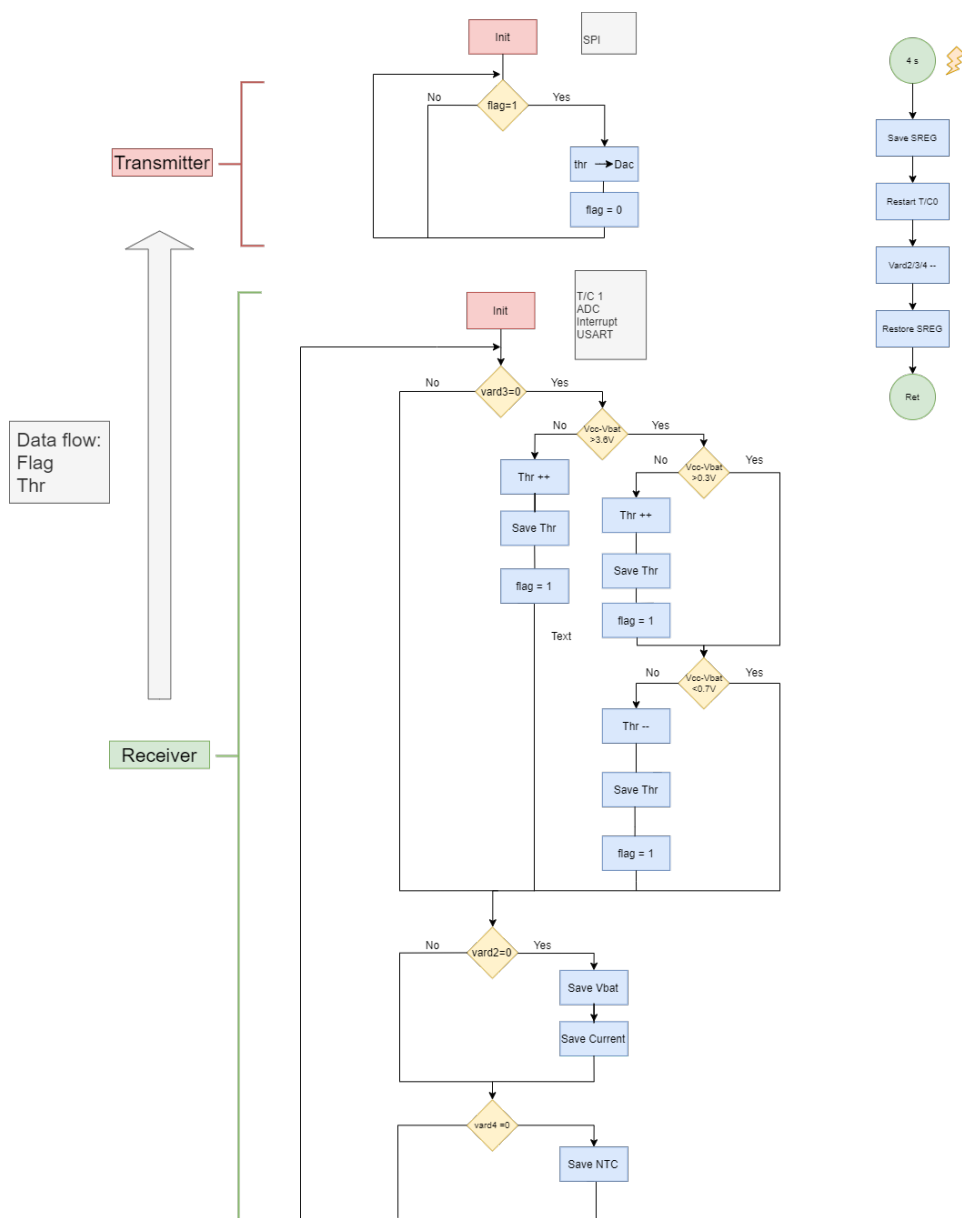


Figure 7.6: Flow chart of firmware.

7.3 Test bench

The same test bench described in chapter six was used to test the overall efficiency of the system. The test was carried out to compare the open-loop and closed-loop NRIC system.

Additional tests were performed to study the behavior of the NRIC system under similar conditions to a subcutaneous implant. Indeed, the subcutaneous implants add complexity to the overall system. The interposed skin causes a displacement between the coils which can compromise the overall efficiency of the system. Furthermore, at transmission frequencies above 100 kHz, the skin influences power transmission due to the power absorption and parasitic capacity.

Therefore, the following tests were also carried out:

- Overall efficiency with animal tissue interposed:
 - Charging current 10 - 25 mA;
- Lateral Misalignments:
 - Interposed air;
 - 0 - 8 mm;
 - Charging current 10 - 25 mA;
- Angular Misalignment:
 - Interposed air;
 - 0 - 12°;
 - Charging current 10 - 25 mA.

For these additional tests, the same battery emulator previously described was used.

7.4 Experimental Results

7.4.1 Open-loop vs closed-loop NRIC system

The closed-loop NRIC system was compared to the open-loop NRIC system to understand if it has improvements in overall efficiency.

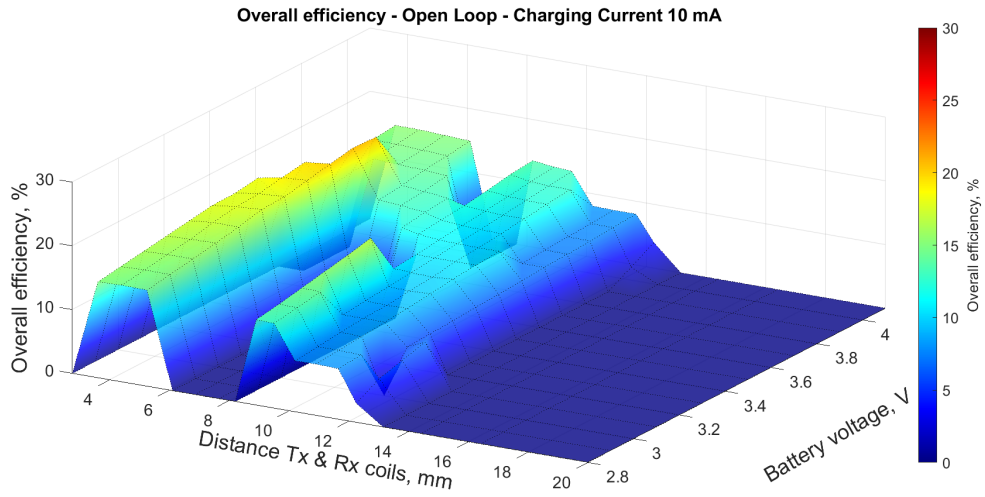
The test was conducted in the best condition for power transmission with coils' perfect alignment. The coils were moved progressively apart by approximately one millimetre in the range of 3 mm to 20 mm, and four different charging currents (10 - 25 - 50 - 100 mA) were used to test the overall efficiency.

Figures 7.7, 7.8, 7.9 and 7.10 show a comparison of the overall efficiency between the open-loop system and the closed-loop system.

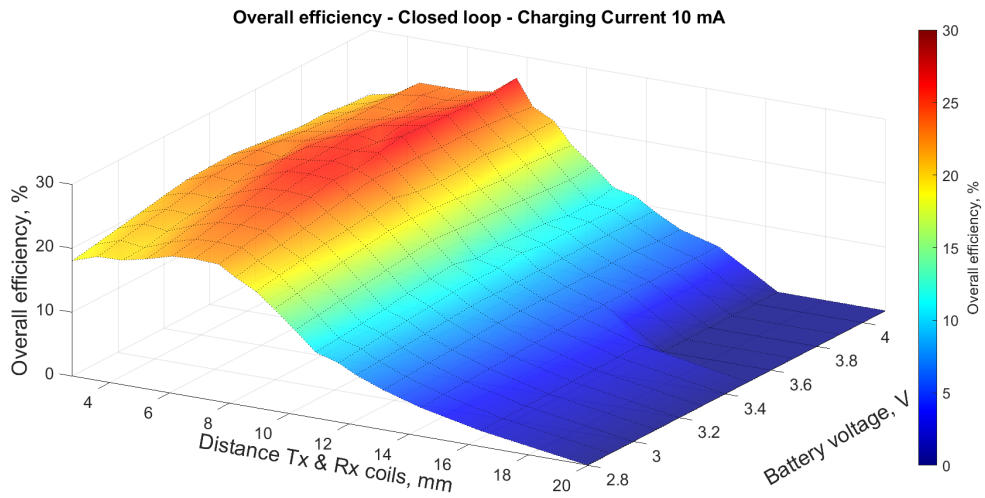
- Figures 7.7a and 7.7b show a comparison of the overall efficiency between the open-loop system and the closed-loop system respectively, with a 10 mA charging current. The maximum overall efficiency is 26.7% compared to 20.7% for the open-loop version. Power transfer up to 18 mm without overheating problems.
- Figures 7.8a and 7.8b show a comparison of overall efficiency between the open-loop system and the closed-loop system respectively, with a 25 mA of charging current. The maximum overall efficiency is 38.2% compared to 30.5% for the open-loop version. Power transfer up to 14 mm without overheating problems.
- Figures 7.9a and 7.9b show a comparison of overall efficiency between the open-loop system and the closed-loop system respectively, with a 50 mA of charging current. The maximum overall efficiency is 43.6% compared to 35.1% for the open-loop version. Power transfer up to 12 mm without overheating problems.
- Figures 7.10a and 7.10b show a comparison of overall efficiency between the open-loop system and the closed-loop system respectively, with a 100 mA of charging current. The maximum overall efficiency is 45.4% compared to 40% for the open-loop version. Power transfer up to 8 mm without overheating problems.

The closed-loop system improved performance in all the cases tested. The transmitter no longer has the fault conditions that did not allow power to be transmitted. With the closed-loop system, the transmitter always delivers the best power for the receiver. Thanks to improved PTH voltage control, it is possible to fine-tune the magnetic field strength and improve heating performance.

Despite the link's best performance at 50 and 100 mA charging currents, the transmitter coil overheats to more than 42 °C at distances over 12 mm and 8 mm respectively. Charging at 10 mA and 25 mA, on the other hand, allows greater distances to be covered without overheating the system. Therefore, 10 mA and 25 mA recharges are the most promising to use, avoiding overheating and a high-intensity magnetic field. For these reasons, subsequent tests are limited to the study of 10 and 25 mA currents.

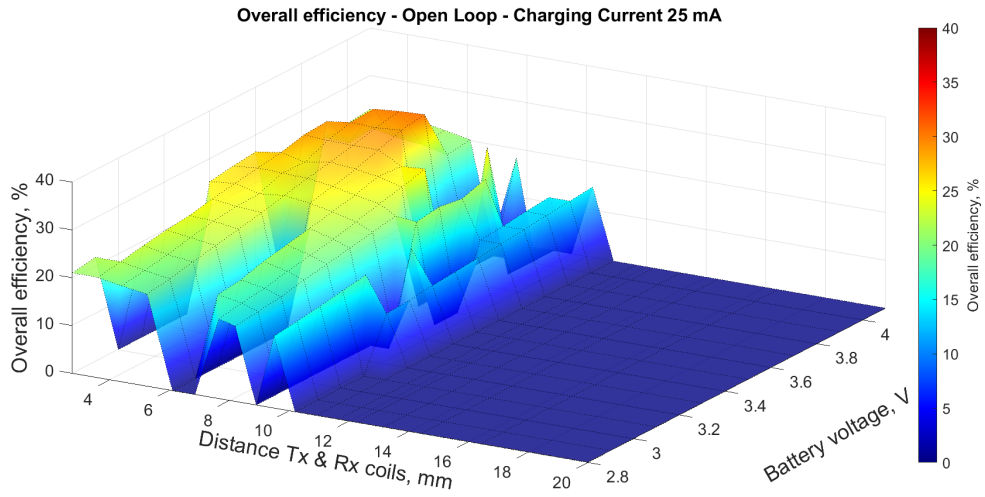


(a)

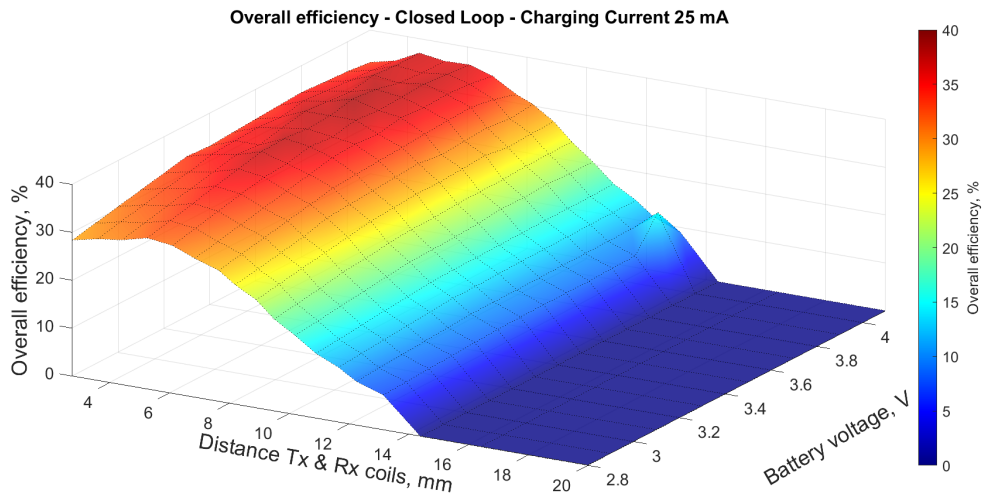


(b)

Figure 7.7: Comparison of overall efficiency, charging current of 10 mA. a) Open-loop NRIC. b) Closed-loop NRIC system.

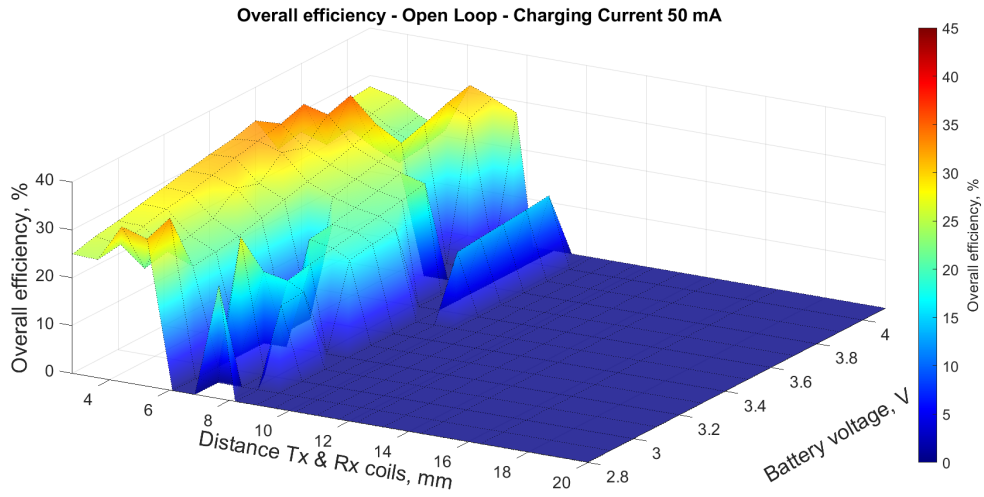


(a)

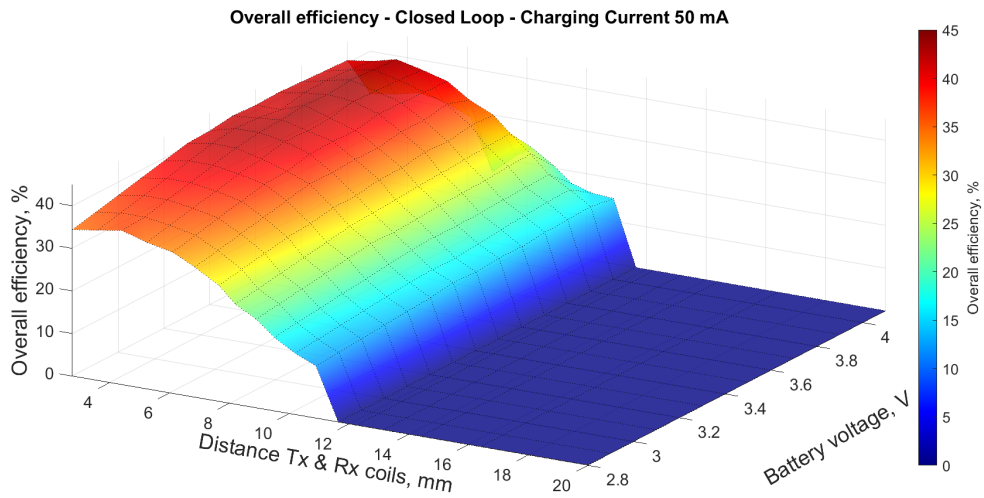


(b)

Figure 7.8: Comparison of overall efficiency, charging current of 25 mA. a) Open-loop NRIC. b) Closed-loop NRIC system.

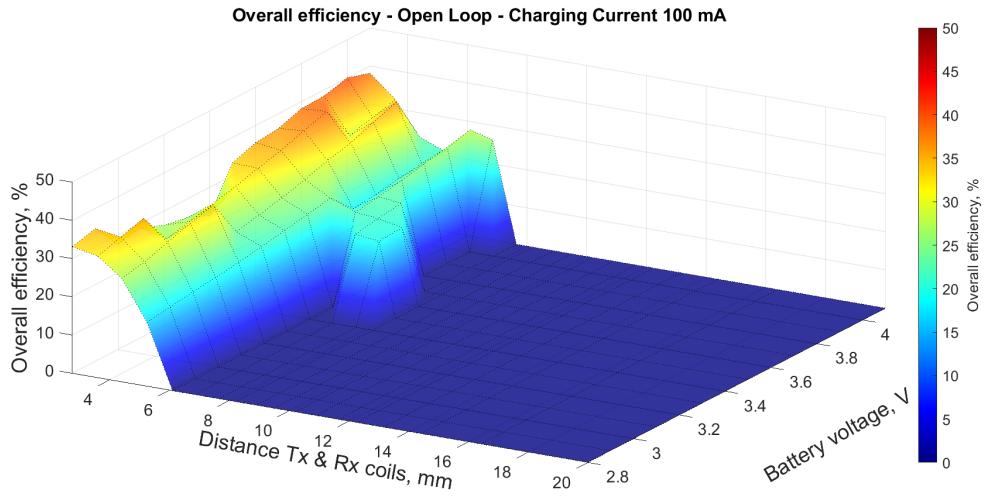


(a)

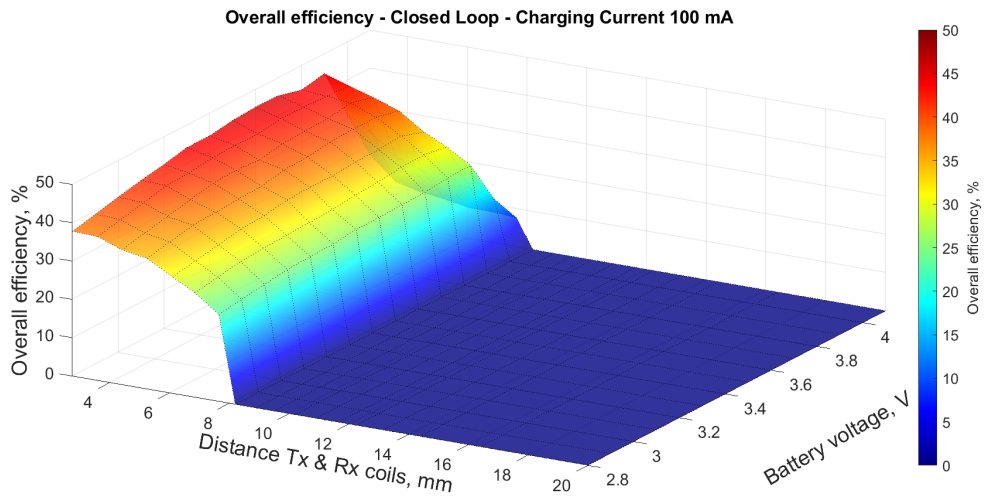


(b)

Figure 7.9: Comparison of overall efficiency, charging current of 50 mA. a) Open-loop NRIC. b) Closed-loop NRIC system.



(a)



(b)

Figure 7.10: Comparison of overall efficiency, charging current of 100 mA. a) Open-loop NRIC. b) Closed-loop NRIC system.

7.4.2 Tests with interposed tissue

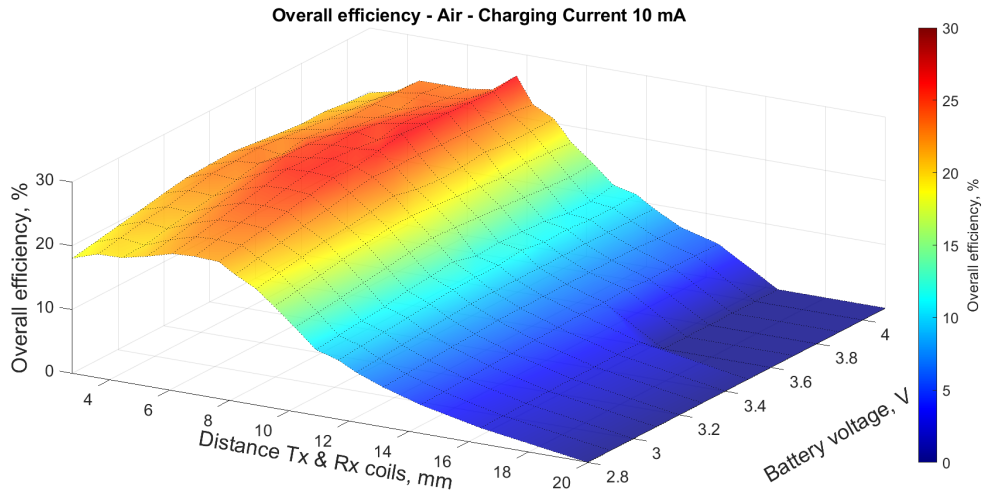
The NRIC system's operation was conducted and tested with an animal tissue interposed between coils to simulate the skin behavior. The skin has dielectric properties (permeability, permittivity, and conductivity) that affect power transmission.

The permeability of the human tissues is equal to the permeability of free space, therefore it does not influence the magnetic field. While the permittivity and conductivity, values depend on the type of tissue and wave frequency. Transfer efficiency is limited due to reflected power and tissue losses at increasingly higher magnetic field frequencies. With a low frequency < 100 kHz, the body appears transparent to the magnetic field, while with a high frequency, the magnetic field is attenuated. Indeed, the human tissues are conductive, so the inner magnetic field induces eddy currents in the tissue. The inducted currents increase with frequency as well as the opposing magnetic field. Therefore, the magnetic field is distorted by the tissue, and above 100 kHz it is attenuated inside the tissue.

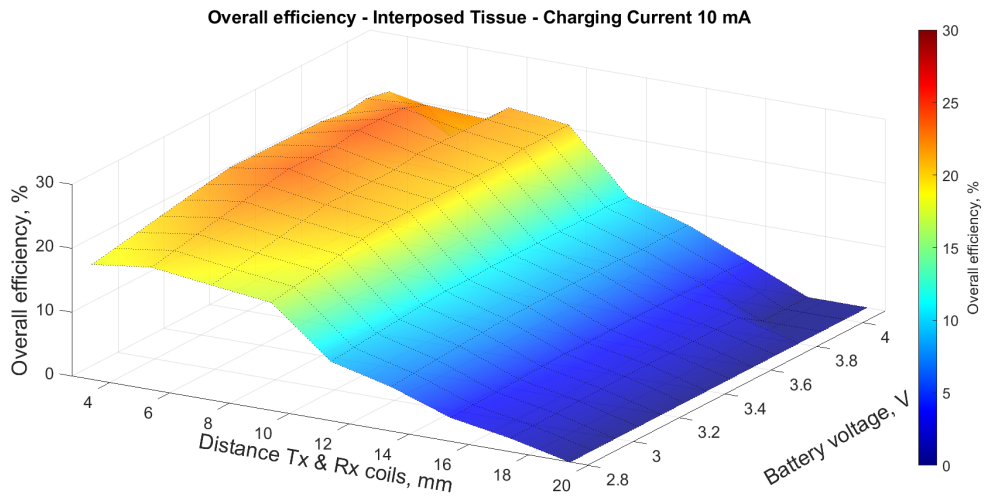
The magnetic field frequency used in the NRIC system developed is 200 kHz. Therefore, the overall efficiency was evaluated to assess the attenuation of the magnetic field with an interposed tissue.

The test was conducted with chicken breast tissue, and the thickness of the animal tissue was changed from 3 to 19 mm with a 2 mm pitch.

Figures 7.11 and 7.12 show the comparison between the overall efficiency of the NRIC with air and animal tissue interposed, for 10 and 25 mA of charging current, respectively. With the animal tissue interposed for 10 mA charging current, the maximum attenuation is 10% (fig. 7.11b), while for 25 mA charging current, the attenuation is 8% (fig 7.12b). The drop in overall efficiency is negligible with interposed tissue for all distances tested. The attenuation reported may also be due to the coils not being perfectly aligned. Therefore, the attenuation of the magnetic field by the skin is negligible at low frequencies.

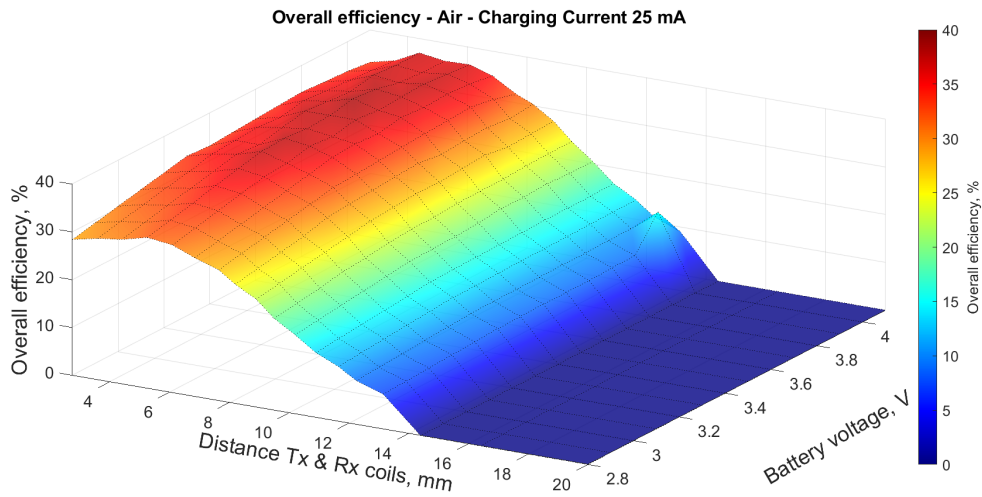


(a)

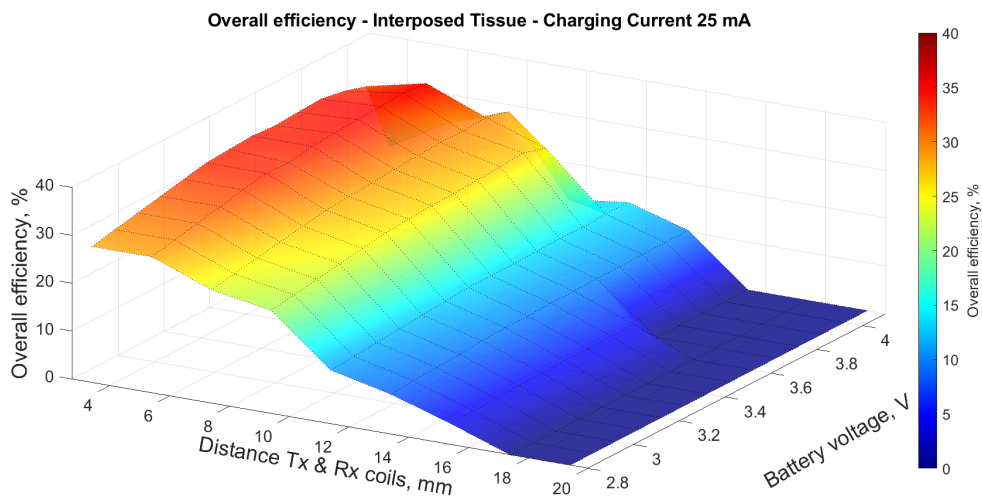


(b)

Figure 7.11: Comparison of overall efficiency, charging current 10 mA. a) Air interposed. b) Animal tissue interposed.



(a)



(b)

Figure 7.12: Comparison of overall efficiency, charging current 25 mA. a) Air interposed. b) Animal tissue interposed.

7.4.3 Lateral and Angular misalignments

The operation of the NRIC system has also been tested with misalignment of the coils. These tests are carried out to understand the strength of the link under low coupling conditions. The value of the coupling factor changes in relation to the geometry disposition of the coils. In particular, the mutual inductance values decrease with lateral and angular misalignments. Therefore, the lateral and angular misalignment was evaluated to investigate the limitations of the NRIC system implemented. In lateral misalignment (fig. 7.13a), the coils are parallel with the plane, but their centers are displaced by a distance (Δ). In the angular misalignments (fig. 7.13b), the planes of the coils are tilted to form an angle (α), and the axis of one coil passes through the center of the coil.

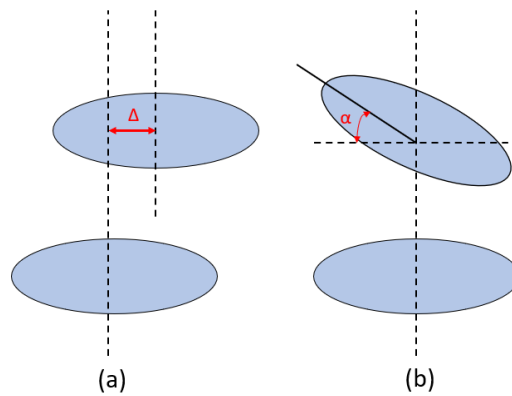
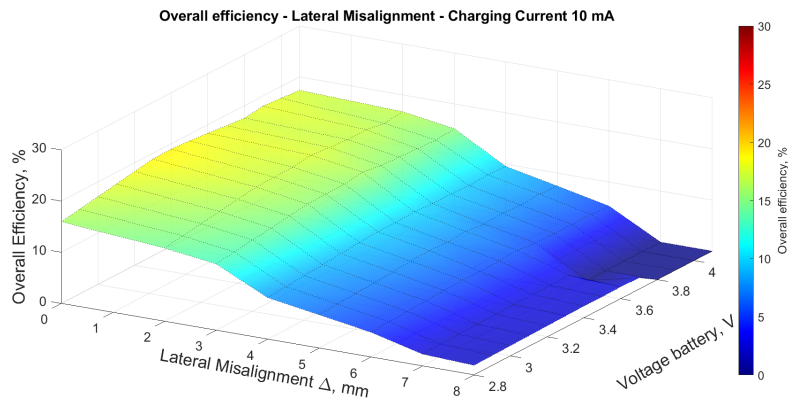


Figure 7.13: a) Lateral misalignments configuration. b) Angular misalignments configuration.

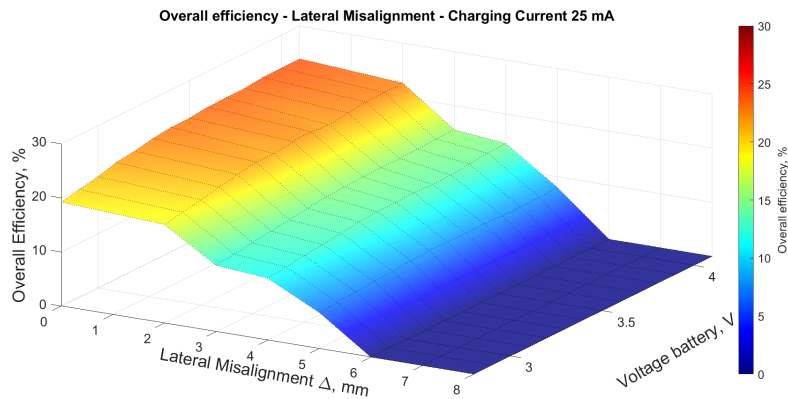
Lateral misalignments

The test was conducted with a lateral misalignment (Δ) from 0 to 8 mm with a step of 1 mm. The distance between the coils is set to 10 mm. 10 and 25 mA charging currents were tested.

Figures 7.14a and 7.14b, 10 and 25 mA charging current respectively, show the overall efficiency of the NRIC system as a function of lateral misalignments and battery voltage. The overall efficiency remains quite constant for both charging current (10 and 25 mA) for a lateral misalignment up to 4 mm. While the lateral misalignments increase, the overall efficiency drops quickly to zero. The transmitter must generate more power when lateral misalignments increase to allow the correct amount of power to the receiver.



(a)

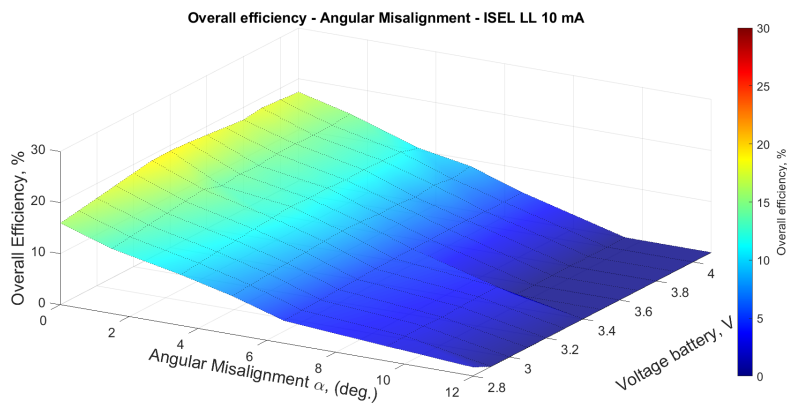


(b)

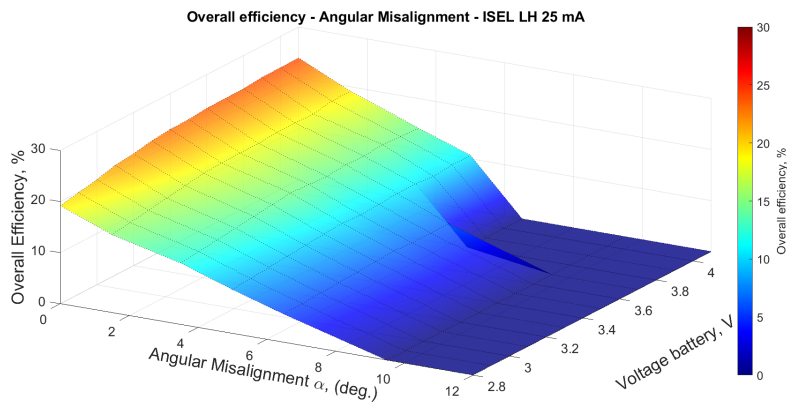
Figure 7.14: Overall efficiency compared to lateral misalignments and battery voltage a) Charging current 10 mA. b) Charging current 25 mA.

Angular misalignments

The angular misalignments test was conducted for angles (α) from 0° to 12° with a step of 2° . The minimum distance between the coil was set to 10 mm. Figures 7.15a and 7.15b, 10 and 25 mA charging current respectively, show the overall efficiency of the NRIC system as a function of angle misalignments and battery voltage. The overall efficiency decreases linearly with the angular misalignments increase. The overall efficiency must not fall below 10% to maintain good power transmission for 10 mA charging, so angles of up to 5° can be achieved. For 25 mA charging, the overall efficiency should not fall below 15%, allowing angles of up to 3° to be achieved.



(a)



(b)

Figure 7.15: Overall efficiency with angular misalignments and battery voltage a) Charging current of 10 mA. b) Charging current of 25 mA.

7.5 Battery charging tests

Charging tests were repeated to validate the closed-loop system using the same batteries described in chapter six. Figure 7.16 shows the test bench for recharging consisting of: transmitter, receiver, power control, the ina240 for current sensing, the battery case and the microcontroller for closed-loop management and data storage. The charging modes are listed below:

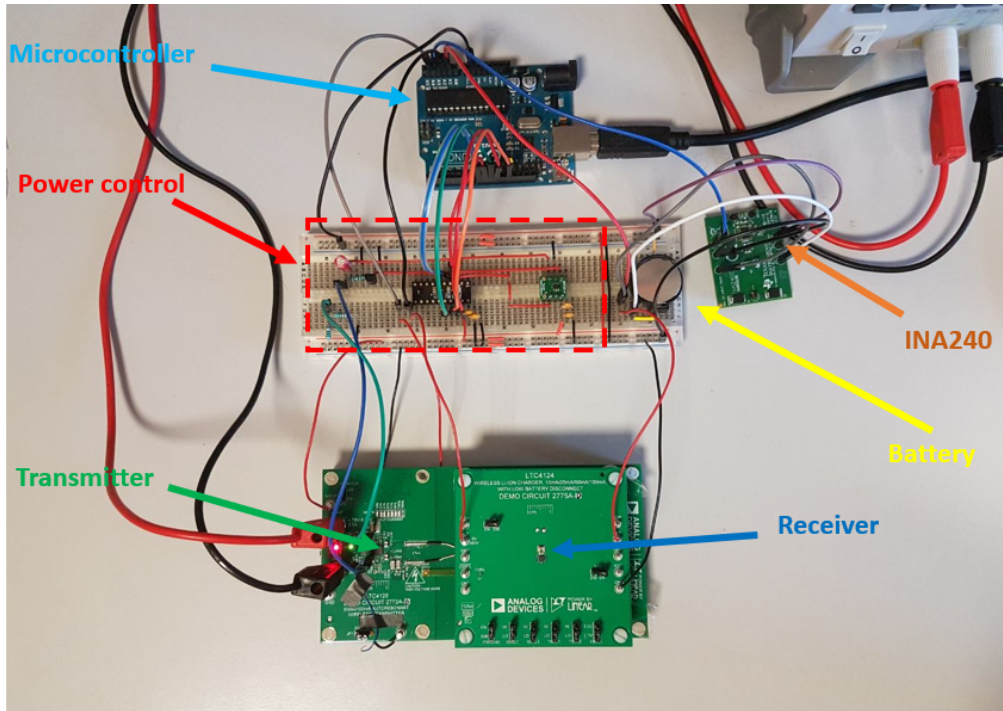


Figure 7.16: Test bench of recharges.

- The LIR2016 battery recharges at 10 mA (0.6 C);
- The LIR2025 battery recharges at 10 and 25 mA (0.4 C and 1 C);
- The LIR2032 battery recharges at 25 mA (0.6 C).

According to the specifications of the LIR2025 battery, it was possible to test two different charging currents (10 and 25 mA).

These tests aim to understand if the closed-loop system allows the batteries to be recharged without any problems during the whole charging phase and to acknowledge the time required to complete recharge. Recharges were carried out with a distance between the coils of 10 mm and perfectly aligned. With the open-loop system, it was impossible to recharge at this distance without overheating or transmitter malfunctions.

The four recharges are shown in figure 7.17. As it can be seen, all the recharges have the two characteristics of lithium battery recharging (constant current and constant voltage). The recharges were carried out without any fault condition, demonstrating the effectiveness of the closed-loop system compared to the open-loop system. Table 7.1 summarises the main characteristics of the recharges: maximum power required by the transmitter during the recharge and time required to complete the recharge.

The LIR2025 battery is suitable for two different charges: normal charging (fig. 7.17b), with a charging time of 5 hours, and fast charging (fig. 7.17c), which allows charging in 3 hours. The LIR2016 battery charging (fig. 7.17a) shows a very short constant current phase, probably due to the charging current used (10 mA). According to the specifications of the LIR2016 battery, the nominal charging current should be 3 mA, whereas a higher current was used for the test.

All batteries have been recharged from the ultra-discharged condition to test the pre-recharge mode characterized by a recharge current of 10% of the programmed recharge. At the start of all recharges, it is evident that the pre-charge mode is correctly activated. Only when the battery voltage exceeds 2.8 V, the current increases until the programmed value.

Battery	Capacity, mAh	Charging current, mA	P in, mW	Recharge time, min
LIR2016	16	10	250	180
LIR2025	25	10 - 25	250 - 450	300 - 170
LIR2032	40	25	455	225

Table 7.1: Summary of recharge performance. Coils distance of 10 mm.

Another key aspect taken into account during the charging process is whether the implemented closed-loop system responds correctly to load variations. Indeed, during charging, the load changes continuously, particularly in the last phase of charging when the required current gradually decreases. The value of the imposed threshold was saved each time it changed to monitor the operation of the closed-loop system (the threshold value corresponds to the value of the PTH voltage). Figure 7.18 shows as the voltage on the PTH pin (red) changes with the current required during all recharging tested. The PTH voltage changes according to the required load, reaching its maximum value when the maximum charging voltage and current are required. Figure 7.18 also shows the zoom in the pre-charge phase. It shows how the PTH voltage also adapts during the pre-charge phase to ensure the best power transmission.

Therefore, the closed-loop system enables the correct and best power transmission to the receiver by modulating the magnetic field strength according to requirements.

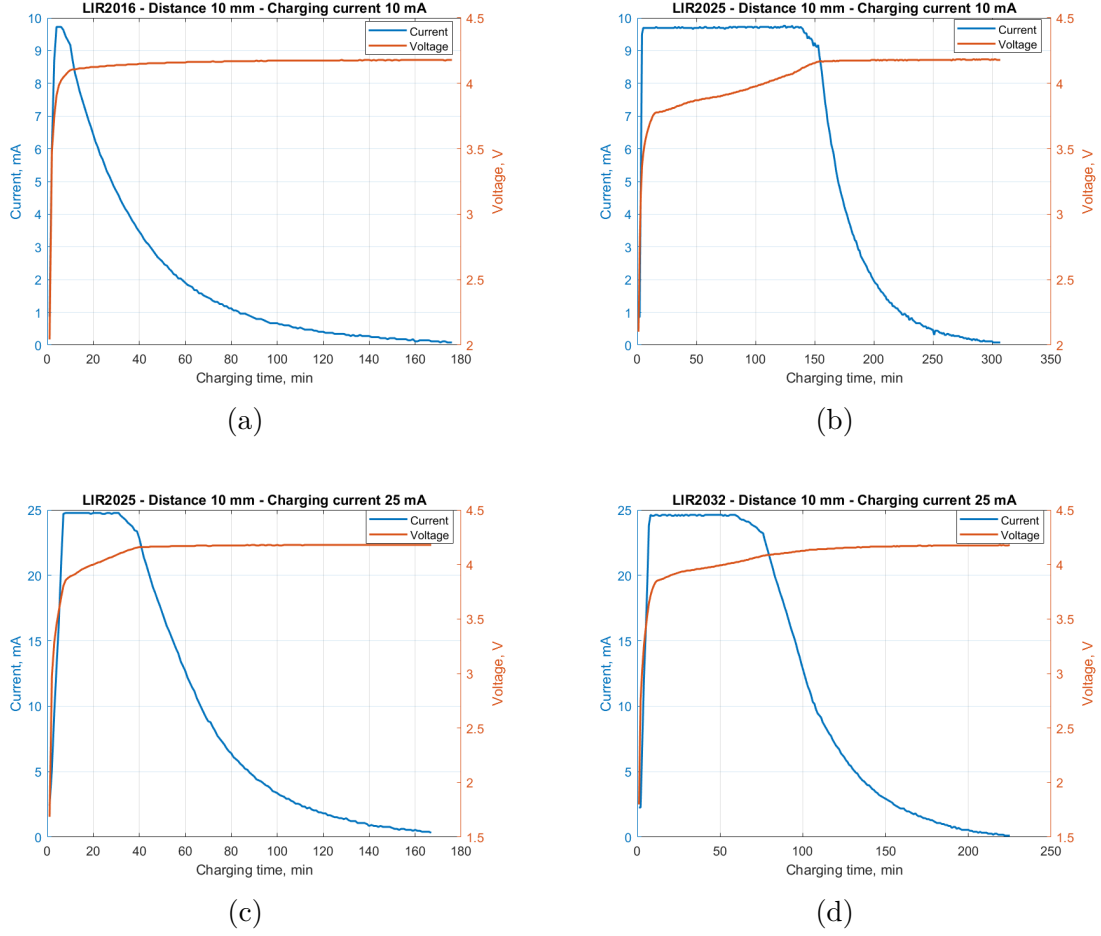


Figure 7.17: Battery recharge with closed-loop system. Charging current in blue and battery voltage in red. Coils distance 10 mm. a) LIR2016, charging current of 10 mA. b) LIR2025, charging current of 10 mA. c) LIR2025, charging current of 25 mA. d) LIR2032, charging current of 25 mA.

7.6 Safety and regulations discussion

Regulations require that the temperature of an implanted device does not exceed the limit of 2 °C above body temperature. Coils are not perfect inductors but are characterized by a resistance that depends on the type of material and manufacture. During power transmission, coils dissipate power, causing them to heat up. On the other hand the heating of ICs is linked to the package thermal impedance ($R_{\Theta JA}$). Therefore, during charging, the Tx coil, Rx coil, and Rx IC temperature were monitored. The NTC thermistor (MURATA, FTN55XH103FD4B) was used to monitor the temperature of the Tx coil. The thermistor has been placed under the Tx coil. Instead, the temperature of the receiver integrated circuit and Rx coil

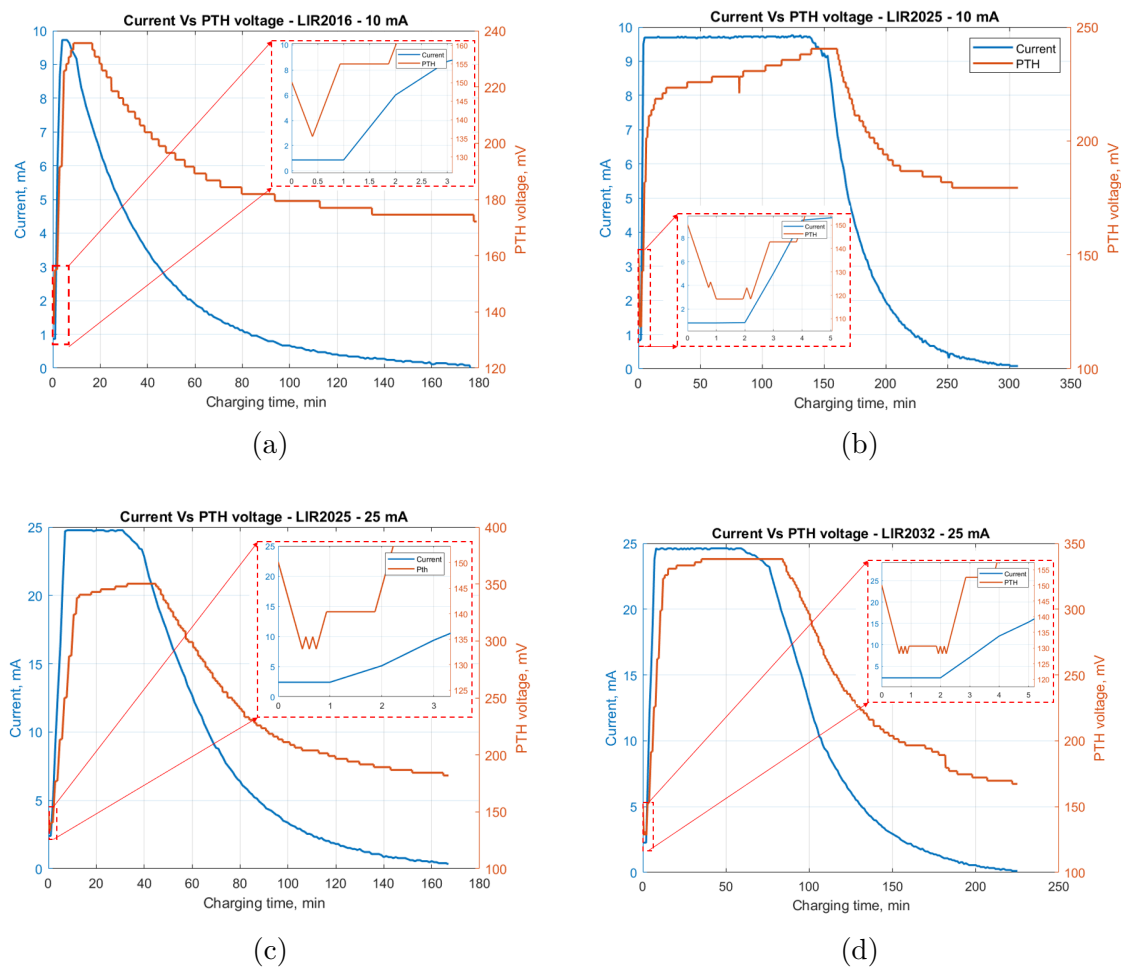


Figure 7.18: PTH variation during recharge. The PTH pin voltage (red) and current (blue). a) LIR2016, charging current of 10 mA. b) LIR2025, charging current of 10 mA. c) LIR2025, charging current of 25 mA. d) LIR2032, charging current of 25 mA.

were monitored with the thermal imaging camera (Ti10, Fluke). The heating of the NRIC closed-loop system with interposed air was evaluated, starting from the room temperature condition (24 °C).

Figure 7.19 shows the heating of the transmission system when charging the LIR2025 battery at 25 mA. Charging at 25 mA has been reported because it is the one that causes the most heating. The receiver has to supply more current, dissipating more power, while the coils have to generate a more intense magnetic field, causing more heating.

The transmitter coil suffers most from heating, reaching almost 33 °C (fig. 7.19a). The Tx coil is external to the body and can reach higher temperatures without giving a sense of burning. The temperature of the Rx coil and the Rx IC (fig. 7.19b)

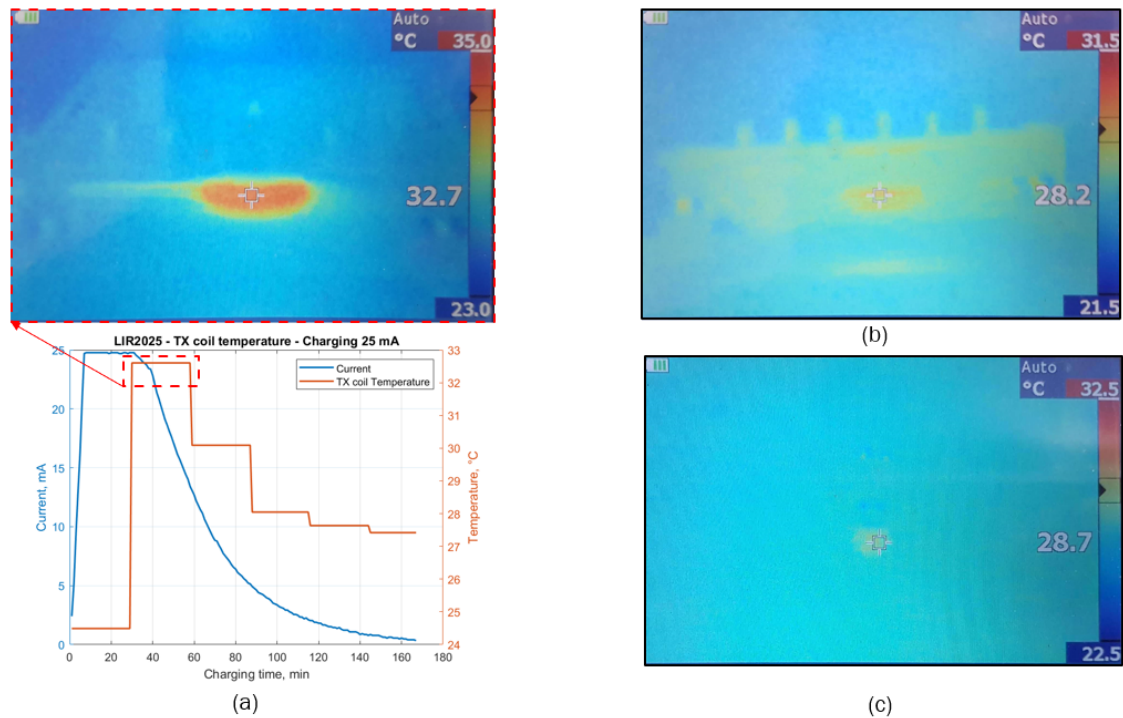


Figure 7.19: Temperature monitoring during LIR2025 battery recharge at 25 mA. Coils distance of 10 mm. a) Tx coil temperature trend during recharge. b) Rx coil temperature. c) Rx IC temperature.

and fig. 7.19c) reaches almost 29 °C. The LIR2025 battery was recharged with 4 different modalities keeping constant at 10 mm the coils distance to better study the temperature variations in the presence or absence of an interposed tissue:

- Interposed air, charging current at 10 mA;
- Interposed air, charging current at 25 mA;
- Interposed animal tissue, 10 mA charging current;
- Interposed animal tissue, 25 mA charging current.

Table 7.2 shows the maximum temperature values reached by the Tx and Rx coils and the receiver IC, while, figure 7.20 shows the Tx temperature trend in the 4 different modalities tested. The thermal conductivity of animal tissue is higher than that of air. Therefore, part of the heat generated by the coil flows into the animal tissue and heats it. The heat transfer, however, causes the temperature of the coil to take longer to warm up. Therefore, when charging, the temperature of the coil with animal tissue in between is lower than that of the coil with air in between.

The table 7.2 also shows that the temperature of the implantable part (Rx coil and Rx IC) does not exceed 26 °C when using the 10 mA charging current with both air and animal tissue interposed.

Batteries	Charging current, mA	Type	Temperature		
			Tx coil , °C	Rx coil, °C	Rx IC, °C
LIR2025	10	Air	27.2	25.3	25.6
LIR2025	25	Air	32.7	28.2	28.7
LIR2025	10	Animal tissue	26.6	24	24.6
LIR2025	25	Animal tissue	24.7	25	27.1

Table 7.2: Analysis of heating during 4 recharging modalities tested with coils distance of 10 mm. The highest recorded temperature was reported. The room temperature is shown in figure 7.20 in the first acquisition.

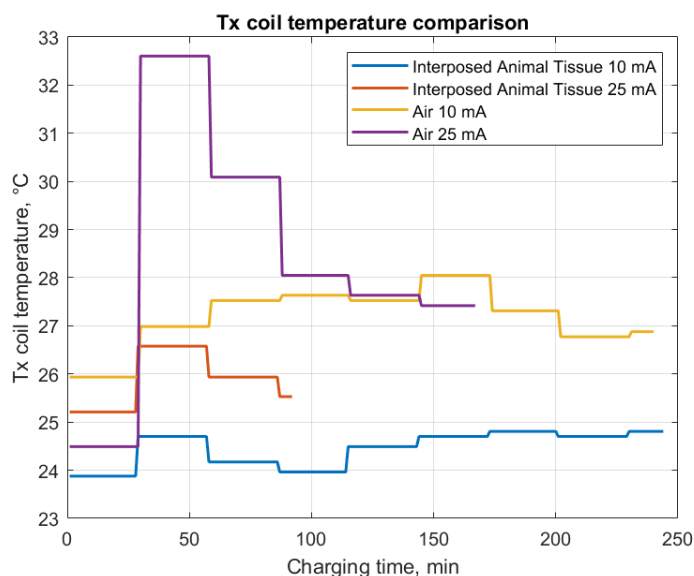


Figure 7.20: The temperature trend of Tx coil for 4 recharging modalities tested (air and animal tissue interposed, 10 and 25 mA charging current).

Chapter 8

Conclusion and future perspectives

Wireless power transfer (WPT) for powering subcutaneous devices has been discussed. According to the implantable devices' requirements, a near-field resonant inductive coupling (NRIC) system was chosen for power transmission. The smaller IC receiver chosen (LTC4124) is capable of recharging an implantable lithium battery. We compared the open-loop NRIC system with the closed-loop NRIC system. The overall efficiency of the system was studied by changing the distance between the coils. The results showed that better efficiency is achieved by using a power transfer control system. The closed-loop system was then tested to define the operability constraints. Tests were conducted with different charging currents and by changing the geometric arrangement of the coils and the interposed material. The system shows promising results for charging currents of 10 and 25 mA, up to a distance of 10 mm both with air and animal tissue interposed. The most critical aspect remains the misalignment between the coils. It has been defined that the maximum tolerable lateral misalignment is 4 mm, while for the angular misalignment, the maximum tolerable is 3° and 5° for 25 mA and 10 mA charging current, respectively. We have recharged three different lithium batteries to validate the closed-loop system's operation and the heating of the system. The recharges were completed without any malfunctions. The IC receiver shows a temperature rise of 2 and 5 °C above room temperature at 10 and 25 mA charging current. The closed-loop NRIC system appears to be a promising system for charging batteries implanted under the skin. However, several studies still have to be conducted:

- Hardware:
 - Integrating the power control system and the transmitter into a single PCB to avoid problems due to noise;
 - Adding battery management to the transmitter to replace the bench power

supply;

- Replacing the microcontroller used (Atmega328p) with two microcontrollers, one for the transmitter and one for the receiver. Given the simplicity of the control algorithm, even microcontrollers that are not computationally powerful but energy-efficient can be fine. The two microcontrollers can exploit wireless link communication. Also in this case, no particular performance is required, as data can be exchanged every few seconds.
- Integrating the receiver with an implantable medical device to check the correct functioning of the charging system.
- Firmware:
 - Implementing a communication system between the receiver and the transmitter, exploiting either Bluetooth Low Energy communication between the receiver and the transmitter already used in the Houston device or exploiting coils by adding a modulator and demodulator to the receiver and transmitter. Bluetooth would be a good choice in terms of space-saving but increases power consumption. Modulator and demodulator, on the other hand, limits power consumption but increases the space occupied by receiver.
- Test:
 - Testing new coils with the aim of reducing the size of the Rx coil, improving flexibility, coupling between Tx and Rx coils and thermal properties.
 - Testing the developed system *in vivo* to study if power transmission is maintained stable in an implanted device.
 - Simulating and test power transfer regulations. (SAR, maximum electric field, and maximum magnetic field).

Bibliography

- [1] E. Meng and R. Sheybani, «Insight: implantable medical devices», *Lab Chip*, vol. 14, pp. 3233–3240, 17 2014. DOI: 10.1039/C4LC00127C. [Online]. Available: <http://dx.doi.org/10.1039/C4LC00127C> (cit. on pp. 1, 3, 4).
- [2] K. Agarwal, R. Jegadeesan, Y. Guo, and N. V. Thakor, «Wireless Power Transfer Strategies for Implantable Bioelectronics», *IEEE Reviews in Biomedical Engineering*, vol. 10, pp. 136–161, 2017 (cit. on pp. 3, 6, 8–16).
- [3] «Active Implantable Medical Devices Market», in, Available on line. [Online]. Available: <https://www.transparencymarketresearch.com/active-implantable-medical-devices-market.html> (cit. on p. 4).
- [4] J. S. Ho, A. J. Yeh, E. Neofytou, S. Kim, Y. Tanabe, B. Patlolla, R. E. Beygui, and A. S. Y. Poon, «Wireless power transfer to deep-tissue microimplants», *Proceedings of the National Academy of Sciences*, vol. 111, no. 22, pp. 7974–7979, 2014, ISSN: 0027-8424. DOI: 10.1073/pnas.1403002111. [Online]. Available: <https://www.pnas.org/content/111/22/7974> (cit. on pp. 3, 5, 14).
- [5] C. H. Amar AB Kouki AB, «Power Approaches for Implantable Medical Devices», *Sensors*, vol. 15, no. 11, pp. 28 889–28 914, 2015. DOI: 10.3390/s151128889. [Online]. Available: <https://doi.org/10.3390/s151128889> (cit. on pp. 4, 11).
- [6] C. Dagdeviren, B. D. Yang, Y. Su, P. L. Tran, P. Joe, E. Anderson, J. Xia, V. Doraiswamy, B. Dehdashti, X. Feng, B. Lu, R. Poston, Z. Khalpey, R. Ghafari, Y. Huang, M. J. Slepian, and J. A. Rogers, «Conformal piezoelectric energy harvesting and storage from motions of the heart, lung, and diaphragm», *Proceedings of the National Academy of Sciences*, vol. 111, no. 5, pp. 1927–1932, 2014, ISSN: 0027-8424. DOI: 10.1073/pnas.1317233111. eprint: <https://www.pnas.org/content/111/5/1927.full.pdf>. [Online]. Available: <https://www.pnas.org/content/111/5/1927> (cit. on p. 5).
- [7] B. I. Rapoport, J. T. Kedzierski, and R. Sarpeshkar, «A Glucose Fuel Cell for Implantable Brain–Machine Interfaces», *PLOS ONE*, vol. 7, no. 6, pp. 1–14, Jun. 2012. DOI: 10.1371/journal.pone.0038436. [Online]. Available: <https://doi.org/10.1371/journal.pone.0038436> (cit. on p. 5).

- [8] K. T. Settaluri, K. T. Settaluri, H. Lo, H. Lo, R. J. Ram, and R. J. Ram, «Thin Thermoelectric Generator System for Body Energy Harvesting», eng, *Journal of electronic materials*, vol. 41, no. 6, pp. 984–988, 2012, ISSN: 0361-5235 (cit. on p. 5).
- [9] P. P. Mercier, A. C. Lysaght, S. Bandyopadhyay, A. P. Chandrakasan, and K. M. Stankovic, «Energy extraction from the biologic battery in the inner ear», eng, *Nature biotechnology*, vol. 30, no. 12, pp. 1240–1243, 2012, ISSN: 1087-0156 (cit. on p. 5).
- [10] R. Das, F. Moradi, and H. Heidari, «Biointegrated and Wirelessly Powered Implantable Brain Devices: A Review», *IEEE Transactions on Biomedical Circuits and Systems*, vol. 14, no. 2, pp. 343–358, 2020 (cit. on p. 6).
- [11] R. P. Bert Lenaerts, *Omnidirectional Inductive Powering for Biomedical Implants*. Springer Netherlands, 2009, pp. 39–56 (cit. on pp. 6–8).
- [12] C. A. Balanis, *Antenna Theory Analysis and desig*. ProQuest Ebook Central, 2016. [Online]. Available: <https://ebookcentral.proquest.com> (cit. on pp. 6, 7).
- [13] R. Shadid and S. Noghanian, «A Literature Survey on Wireless Power Transfer for Biomedical Devices», eng, *International journal of antennas and propagation*, vol. 2018, pp. 1–11, 2018, ISSN: 1687-5869 (cit. on p. 8).
- [14] K. Agarwal, R. Jegadeesan, Y.-X. Guo, and N. V. Thakor, «Wireless Power Transfer Strategies for Implantable Bioelectronics», eng, vol. 10, pp. 136–161, 2017, ISSN: 1941-1189 (cit. on pp. 7, 8).
- [15] H. Jiang, J. Zhang, D. Lan, K. K. Chao, S. Liou, H. Shahnasser, R. Fechter, S. Hirose, M. Harrison, and S. Roy, «A Low-Frequency Versatile Wireless Power Transfer Technology for Biomedical Implants», eng, *IEEE transactions on biomedical circuits and systems*, vol. 7, no. 4, pp. 526–535, 2013, ISSN: 1932-4545 (cit. on p. 7).
- [16] R. Jegadeesan and Y. Guo, «Topology Selection and Efficiency Improvement of Inductive Power Links», *IEEE Transactions on Antennas and Propagation*, vol. 60, no. 10, pp. 4846–4854, 2012 (cit. on pp. 8, 9).
- [17] M. Kiani, U.-M. Jow, and M. Ghovanloo, «Design and Optimization of a 3 Coil Inductive Link for Efficient Wireless Power Transmission», eng, vol. 5, no. 6, pp. 579–591, 2011, ISSN: 1932-4545 (cit. on p. 9).
- [18] I. Hochmair, P. Nopp, C. Jolly, M. Schmidt, H. Schöber, C. Garnham, and I. Anderson, «MED-EL Cochlear Implants: State of the Art and a Glimpse Into the Future», eng, *Trends in amplification*, vol. 10, no. 4, pp. 201–219, 2006, ISSN: 1084-7138 (cit. on p. 9).

-
- [19] F.-G. Zeng, S. Rebscher, W. Harrison, X. Sun, and H. Feng, «Cochlear Implants: System Design, Integration, and Evaluation», eng, *IEEE reviews in biomedical engineering*, vol. 1, pp. 115–142, 2008, ISSN: 1937-3333 (cit. on p. 9).
- [20] M. Kiani and M. Ghovanloo, «An RFID-Based Closed-Loop Wireless Power Transmission System for Biomedical Applications», eng, vol. 57, no. 4, pp. 260–264, 2010, ISSN: 1549-7747 (cit. on p. 9).
- [21] R.-H. Kim, H. Tao, T.-i. Kim, Y. Zhang, S. Kim, B. Panilaitis, M. Yang, D.-H. Kim, Y. H. Jung, B. H. Kim, Y. Li, Y. Huang, F. G. Omenetto, and J. A. Rogers, «Materials and Designs for Wirelessly Powered Implantable Light-Emitting Systems», eng, vol. 8, no. 18, pp. 2812–2818, 2012, ISSN: 1613-6810 (cit. on p. 10).
- [22] U.-M. Jow and M. Ghovanloo, «Modeling and Optimization of Printed Spiral Coils in Air, Saline, and Muscle Tissue Environments», eng, *Conference proceedings (IEEE Engineering in Medicine and Biology Society. Conf.)*, vol. 2009, pp. 6387–6390, 2009, ISSN: 1557-170X (cit. on p. 10).
- [23] P. Feng and T. G. Constandinou, «Autonomous Wireless System for Robust and Efficient Inductive Power Transmission to Multi-Node Implants», *bioRxiv*, 2021. DOI: 10.1101/2021.02.01.429239. eprint: <https://www.biorxiv.org/content/early/2021/02/02/2021.02.01.429239.full.pdf>. [Online]. Available: <https://www.biorxiv.org/content/early/2021/02/02/2021.02.01.429239> (cit. on p. 10).
- [24] R. Jegadeesan, K. Agarwal, Y.-X. Guo, S.-C. Yen, and N. V. Thakor, «Wireless Power Delivery to Flexible Subcutaneous Implants Using Capacitive Coupling», eng, *IEEE transactions on microwave theory and techniques*, vol. 65, no. 1, pp. 280–292, 2017, ISSN: 1557-9670 (cit. on p. 10).
- [25] R. Jegadeesan, Y. Guo, and M. Je, «Electric near-field coupling for wireless power transfer in biomedical applications», Dec. 2013, pp. 1–3, ISBN: 978-1-4673-6096-8. DOI: 10.1109/IMWS-BIO.2013.6756140 (cit. on p. 11).
- [26] G. L. Barbruni, P. Motto Ros, D. Demarchi, S. Carrara, and D. Ghezzi, «Miniaturised Wireless Power Transfer Systems for Neurostimulation: A Review», eng, vol. PP, pp. 1–1, 2020, ISSN: 1932-4545 (cit. on pp. 11, 12).
- [27] B. C. Johnson, K. Shen, D. Piech, M. M. Ghanbari, K. Y. Li, R. Neely, J. M. Carmena, M. M. Maharbiz, and R. Muller, «StimDust: A 6.5mm³, wireless ultrasonic peripheral nerve stimulator with 82 peak chip efficiency», eng, in *2018 IEEE Custom Integrated Circuits Conference CICC*, IEEE, 2018, pp. 1–4, ISBN: 9781538624838 (cit. on p. 12).

- [28] S. Barnett, H.-D. Rott, G. Ter Haar, M. Ziskin, and K. Maeda, «The sensitivity of biological tissue to ultrasound», *Ultrasound in medicine and biology*, vol. 23, pp. 805–12, Feb. 1997. DOI: 10.1016/S0301-5629(97)00027-6 (cit. on p. 13).
- [29] J. Zhao, R. Ghannam, Q. H. Abbasi, M. Imran, and H. Heidari, «Simulation of Photovoltaic Cells for Implantable Sensory Applications», in *2018 IEEE SENSORS*, 2018, pp. 1–4 (cit. on pp. 13, 14).
- [30] L. Bereuter, S. Williner, F. Pianezzi, B. Bissig, S. Buecheler, J. Burger, R. Vogel, A. Zurbuchen, and A. Haeberlin, «Energy Harvesting by Subcutaneous Solar Cells: A Long-Term Study on Achievable Energy Output», eng, *Annals of biomedical engineering*, vol. 45, no. 5, pp. 1172–1180, 2017, ISSN: 0090-6964 (cit. on p. 13).
- [31] A. N. Bashkatov, E. A. Genina, V. I. Kochubey, and V. V. Tuchin, «Optical properties of human skin, subcutaneous and mucous tissues in the wavelength range from 400 to 2000 nm», eng, *Journal of physics. D, Applied physics*, vol. 38, no. 15, pp. 2543–2555, 2005, ISSN: 1361-6463 (cit. on p. 13).
- [32] J. S. Ho, S. Kim, and A. S. Y. Poon, «Midfield Wireless Powering for Implantable Systems», eng, *Proceedings of the IEEE*, vol. 101, no. 6, pp. 1369–1378, 2013, ISSN: 0018-9219 (cit. on p. 14).
- [33] A. S. Y. Poon, S. O’Driscoll, and T. H. Meng, «Optimal Frequency for Wireless Power Transmission Into Dispersive Tissue», eng, *IEEE transactions on antennas and propagation*, vol. 58, no. 5, pp. 1739–1750, 2010, ISSN: 0018-926X (cit. on p. 15).
- [34] K. K S, K. Ilango, and G. Manjula, «Study of Midfield Wireless Power Transfer for Implantable Medical Devices», Jul. 2018, pp. 44–47. DOI: 10.1109/IBIOMED.2018.8534820 (cit. on p. 15).
- [35] R. Warty, M.-R. Tofghi, U. Kawoos, and A. Rosen, «Characterization of Implantable Antennas for Intracranial Pressure Monitoring: Reflection by and Transmission Through a Scalp Phantom», eng, *IEEE transactions on microwave theory and techniques*, vol. 56, no. 10, pp. 2366–2376, 2008, ISSN: 0018-9480 (cit. on p. 15).
- [36] E. Y. Chow, A. L. Chlebowski, S. Chakraborty, W. J. Chappell, and P. P. Irazoqui, «Fully Wireless Implantable Cardiovascular Pressure Monitor Integrated with a Medical Stent», eng, *IEEE transactions on biomedical engineering*, vol. 57, no. 6, pp. 1487–1496, 2010, ISSN: 0018-9294 (cit. on p. 16).
- [37] N. Di Trani, A. Silvestri, G. Bruno, T. Geninatti, C. Y. X. Chua, A. Gilbert, G. Rizzo, C. S. Filgueira, D. Demarchi, and A. Grattoni, «Remotely controlled nanofluidic implantable platform for tunable drug delivery», eng, *Lab on a chip*, vol. 19, no. 13, pp. 2192–2204, 2019, ISSN: 1473-0189 (cit. on pp. 18, 19).

- [38] I. Williams, A. Rapeaux, J. Pearson, K. Nazarpour, E. Brunton, S. Luan, Y. Liu, and T. Constandinou, «SenseBack – Implant considerations for an implantable neural stimulation and recording device», Oct. 2019, pp. 1–4. DOI: 10.1109/BIOCAS.2019.8919046 (cit. on pp. 19, 20).
- [39] I. Williams, A. Rapeaux, Y. Liu, S. Luan, and T. Constandinou, «A 32-ch. bidirectional neural/EMG interface with on-chip spike detection for sensorimotor feedback», Oct. 2016, pp. 528–531. DOI: 10.1109/BioCAS.2016.7833848 (cit. on p. 20).
- [40] *BS EN 45502-1:1998: Active implantable medical devices. General requirements for safety, marking and information to be provided by the manufacturer*, eng, 1998 (cit. on p. 22).
- [41] *100mA Wireless Li-Ion Charger with Low Battery Disconnect*, LTC4124, Rev. A, Analog Devices, 2021. [Online]. Available: <https://www.analog.com/media/en/technical-documentation/data-sheets/LTC4124.pdf> (cit. on pp. 25, 26, 29).
- [42] *LTC4124/LTC4125, 100mA Wireless Li-Ion Charger Demonstration Kit*, Analog Devices, 2021. [Online]. Available: <https://www.analog.com/media/en/dsp-documentation/evaluation-kit-manuals/DC2770A-B-KIT.pdf> (cit. on pp. 25, 32).
- [43] *5W AutoResonant Wireless Power Transmitter*, LTC4125, Analog Devices, 2021. [Online]. Available: <https://www.analog.com/media/en/technical-documentation/data-sheets/4125f.pdf> (cit. on pp. 31, 33, 35, 36, 39).
- [44] W. Li, *Close the Loop Between Wireless Charger Receiver and Transmitter Without Digital Controllers*, Analog Devices. [Online]. Available: <https://www.analog.com/en/technical-articles/close-the-loop-between-wireless-charger-receiver-and-transmitter.html> (cit. on p. 52).